Summer 7-9-2020

Development and demonstration of a pico-Watt calorimeter for optical absorption spectroscopy

Behshad Roshanzadeh
University of New Mexico

Behshad Roshanzadeh

Candidate

Physics and Astronomy

Department

This dissertation is approved, and it is acceptable in quality and form for publication:

Approved by the Dissertation Committee:

Wolfgang Rudolph , Chairperson

Stephen T. Boyd

Mansoor Sheik-Bahae

Tito Busani

Development and demonstration of a pico-Watt calorimeter for optical absorption spectroscopy

by

Behshad Roshanzadeh

M.S., Optical Science & Engineering, University of New Mexico, 2014
M.S., Photonics, Shahid Beheshti University, 2011
B.S., Physics, Shahed University, 2008

DISSERTATION

Submitted in Partial Fulfillment of the
Requirements for the Degree of

Doctor of Philosophy

Optical Science & Engineering

The University of New Mexico

Albuquerque, New Mexico

July, 2020

Dedication

To my wife

To my son

To my mom and dad

To my brothers

Acknowledgments

I would first like to express my gratitude to my advisor, Professor Wolfgang Rudolph, for his patience and dedication in guiding me through my doctorate journey. He was always there whenever I needed his guidance. I would like to thank my co-advisor, Professor Stephen Boyd, for his support and guidance throughout my research.

I wish to thank the other members of my dissertation committee: Professor Mansoor Sheik-Bahae and Professor Tito Busani for generously offering their time and guidance throughout the preparation and review of this dissertation.

I would like to acknowledge the help that I have received from Dr. Ruslan Hummatov, Dr. Linh Le, Dr. Vasudevan Nampoothiri, Dr. Luke Emmert, and Dr. Felix Jaeckel and thank them for their support, guidance and good will throughout this journey.

My gratitude to my dear friends who supported and encouraged me to strive towards my goal.

My deepest gratitude goes to my family: Mina, Mom, Dad, Hadi, and Behnam. I would not be writing this page if it wasn't for your unconditional love, support, and encouragement in all aspects of life.

Warm greetings to my son, Ryan, who gave me strength and encouragement during the preparation of this dissertation.

Development and demonstration of a pico-Watt calorimeter for optical absorption spectroscopy

by

Behshad Roshanzadeh

M.S., Optical Science & Engineering, 2014

M.S., Photonics, 2011

B.S., Physics, 2008

Ph.D., Optical Science & Engineering, 2020

Abstract

An optical calorimeter for sensitive absorption measurements of non-radiative samples at 4 K was designed, built and demonstrated. It consists of a cryostat cooled by a commercial pulse tube (PTC) refrigerator, a measurement chamber housing the sample and thermometers, and various fiber-coupled light sources. By employing measures to damp mechanical noise from the environment and active temperature stabilization of critical components of the instrument temperature noise as low as 6 nK/√Hz at 50 mHz was achieved under 15 mW of optical excitation. An optical absorption induced temperature increase of the sample as small as 2.5 nK could be resolved using paramagnetic temperature sensors with SQUID (Superconducting Quantum Interference Device) readout. This resulted in an absorption sensitivity of 0.3 ppm and 0.6 ppb for tunable 30-

μW optical excitation from 330 nm to 1700 nm and for 15-mW laser excitation, respectively. The instrument was applied to the characterization of stacks of dielectric films for material science studies and laser mirror development.

Contents

Contents

Contents

Contents

List of Figures

List of Figures

List of Figures

List of Figures

List of Tables

Chapter 1

Introduction and Background

The focus of this dissertation is the development and demonstration of a novel technique for the measurement of nonradiative optical absorption with very high sensitivity. The new approach employs quantum metrology (Superconducting Quantum Interference Devices or SQUIDs) at cryogenics temperatures and enable us to measure pico-Watt absorbed power.

The aim of this chapter is to provide background information and give a general introduction to the work presented in this thesis. This includes a summary of the research motivation and goals, and an outline of the chapters of this thesis.

1.1 Motivation: Sensitive Optical Absorption Spectroscopy

Sensitive measurements of optical absorption with spectral resolution are important for areas ranging from fundamental science to materials engineering. In optics and photonics, characterization of absorption of ultra-pure optical samples is crucial for technology development, while the characterization of nano-particles, crystal defects and single atoms and molecules helps to understand the photo-physics of single-absorbing centers.

In the past few decades, the need for materials with utmost purity and quality has been growing continuously in many areas in science and technology. In optics and photonics, high-purity dielectric materials are particularly important for substrates, nonlinear optical elements, and optical coatings. Prominent examples can be found in high power laser systems, where the laser power scaling breaks new records at a fast rate and meeting the advanced requirements puts high demands on optical components [1]. In state-of-the-art photolithographic systems absorption and subsequent photo-degradation of the imaging optics may eventually lead to distortion of features and costly component replacement [2], [3]. In laser fusion experiments optical coatings with extremely high damage threshold are essential for large optical components [4], [5].

Many optical materials suffer from the presence of impurities and defects at low concentration, which give rise to absorption [6] in addition to the absorption that is present in the "perfect" host material in its transparent spectral region. Such defects often

determine key operational limitations in optical components [7], [8]. For example, absorption of high power laser beams leads to undesired heating of optical elements [9], can produce thermal lenses in optical windows [10], and can ultimately result in physical damage, e.g., ablation and defect growth [11], [12]. Even excitations below the optical damage threshold that produce material modifications such as photobleaching can render the component useless [13]. E' centers are just one example that has been studied extensively in one of the most important optical materials, fused silica [14].

These examples show that sensitive measurement of optical absorption is a crucial first step to produce materials of highest quality. Absorption measurement often provide first information about the presence of impurities in optical bulk materials as well as optical thin films and coatings. Absorption spectra may provide guidance for improving the transparency of optical samples, in particular if defects can be identified according to their spectral fingerprint. Sensitive absorption measurements can also help us to understand possible performance changes and limitations of optical materials during their use in *e.g.* in high-power laser systems [15].

The detection of single, non-fluorescing impurity atoms or molecules is now regarded as a critical component in many areas of nano-physics and -chemistry [16]–[18]. To estimate the order of magnitude of absorbed power by a single absorbing center (a non-fluorescing atom, molecule, lattice defect, or nanoparticle), let us assume the simplified geometry shown in Fig. 1.1. The single absorbing center is on or in a typical fused silica substrate and is excited optically by a CW laser. It absorbs one photon (wavelength λ = 1 μm) and relaxes with relaxation time of ten nanoseconds non-radiatively dissipating heat

to the substrate. Assuming that the next absorption event follows the relaxation immediately, the dissipated power is 20 pW. To measure such an absorbing center one needs to be able to measure 20 pW of dissipated power. The goal of this dissertation is to develop and test an instrument to measure absorption with pico-Watt sensitivity.

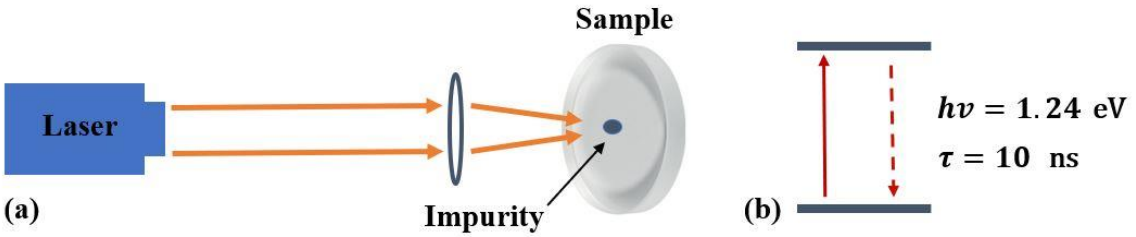

Figure 1.1: (a) A simplified scheme showing the optical excitation of a single impurity particle on a substrate. (b) The single absorbing center absorbs one photon (λ = 1 μm) every ten nanoseconds non-radiatively.

1.2 Overview of Absorption Measurement Techniques and their Limitations

To stay ahead of the demand for nondestructive characterization of the absorption in optical samples, a number of different experimental techniques with high sensitivity have been developed.

If the absorbing centers fluoresce efficiently, it is relatively straightforward to perform sensitive detection and characterization of absorbing centers, down to the limit of single molecules [19]–[21]. However, there are many materials of interest that absorb light but do not fluoresce efficiently [22]–[24]. Materials of these types have instead been

measured with extinction or photothermal techniques.

In a typical optical extinction experiment transmitted and incident optical power are compared. These transmission measurements measure the combined effect of reflection, scattering and absorption losses. The sensitivity of this type of extinction detection technique is limited by the intensity fluctuations of the probing laser [25]. Single-molecule sensitivity has been achieved by extinction measurements where the difference in transmitted light with and without the molecule in the focus amounts to several parts-per-million [25], [26]. Such a sensitivity was obtained in a highly optimized environment where the background scattering from the sample, caused by inhomogeneities in refractive index arising for instance from surface roughness, was minimized so that the molecule can be distinguished from the background.

Absorption measurements using photothermal techniques have been increasingly used in the past few years to detect the presence of non-fluorescing impurities and defects in samples for optics related applications [16], [27]. The photothermal techniques are based on measuring a change in a thermodynamic parameter of the sample arising from the sample heating. When the sample absorbs the optical radiation from a strong pump laser, a local temperature change happens in the sample where it results in a change in a sample property. A weak probe laser measures this change and then the proper calibration yields the sample absorbance. For this purpose, many different techniques and sensors have been developed and demonstrated. Examples are listed in table 1.1. These techniques are distinguished by the temperature dependent physical property probed and how its change is sensed. As an example, photoacoustic spectroscopy uses a sensitive microphone to

monitor the pressure wave induced in a sample by a modulated light beam or pulsed excitation.

Table 1.1: Common photothermal techniques for absorption measurement. Table taken from [27].

Thermodynamic Parameter	**Measured Physical Property**	**Detection Technique**
Temperature	Temperature	Calorimetry
Pressure, P(T)	Acoustic wave	Photoacoustic Spectroscopy
Density, ρ(T)	Refractive Index	Photothermal Lens Photothermal Interferometry Photothermal Deflection Photothermal Refraction Photothermal Diffraction
Density, ρ(T)	Surface Deformation	Surface Deflection

Of the photothermal techniques, the most common ones are those that detect wave-front distortion of a probe beam due to the refractive index change induced by a pump beam, and calorimetry where the temperature change is measured directly using thermometers.

1.2.1 Photothermal Wave-Front Distortion

The wave-front distortion technique also known as photothermal lensing or photothermal interferometry (or other listed in Table 1.1) relies on the temperature dependence of the refractive index dn/dT of the sample to be characterized.

Figure 1.2 shows a basic schematic of photothermal lens spectroscopy. The nonuniform absorption-induced heating of the sample by a pump beam induces a temperature gradient. The resulting refractive index gradient leads to the formation of a thermal lens which then results in focusing or defocusing of the incident light. The transmitted light through a pinhole positioned past the sample depends on the sign and the focal length of the induced lens.

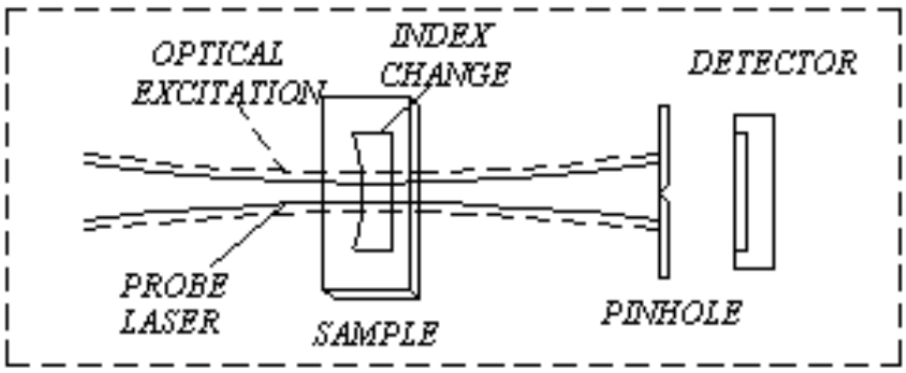

Figure 1.2: Schematic of photothermal lens spectroscopy and the temperature dependent refractive index profile (thermal lens) that is created. Image taken from [27].

Typical absorption sensitivities of photothermal wave-front distortion techniques, are on the order of ppm (parts per million) [28]–[30]. The most sensitive photothermal wave-front methods such as common-path interferometry can achieve sensitivities A_{min} as high as 0.01 parts per million, but only if high-intensity pump beams of a few Watts are available as pump. Such beams are typically available only at selected (laser) wavelengths [31], so that continuous absorption spectra cannot be measured.

Rather than sensitivity in terms of minimum measurable absorptance A_{min}, it is often more useful to consider the minimum absorbed power P_{min} that a given technique can

sense:

$$A_{min} = {P_{min}}/{P_0} \tag{1.1}$$

where P_0 is the incident power illuminating the sample. The $P_{\min}$ that can typically be detected by photothermal wave-front distortion techniques is on the order of a few ten nW [31].

Let's consider a case where a single excitation pulse illuminates a test sample. Assuming negligible heat dissipation during the pulse excitation the heated volume V_h is limited to the spot-size of the excitation source. The latter is true when the single pulse time duration Δt is much smaller than the time for heat to diffuse out of the excited volume. For such a measurement, the $P_{\min}$ can be related to the minimum detectable temperature change ΔT_{min} according to the relationship:

$$P_{min} = \frac{C_h}{\Delta t}\Delta T_{min} \tag{1.2}$$

where C_h is the heat capacity of the heated volume whose temperature change is measured. The heat capacity is the product of heated volume V_h, material density ρ and specific heat capacity C_p:

$$C_h = V_h \rho C_p \tag{1.3}$$

For wave-front distortion techniques, the minimum index change Δn_{min} in the beam center that can be detected, relates to ΔT_{min} as [27]:

$$\Delta n_{min} = \frac{\partial n}{\partial T}\Delta T_{min} \tag{1.4}$$

Combining equations (1.2) to (1.4), the minimum detectable absorbed power for wave-front distortion techniques can be written as:

$$P_{min} = \frac{V_h \rho C_p \Delta n_{min}}{\Delta t \left(\frac{\partial n}{\partial T}\right)} \tag{1.5}$$

Thus, the performance of photothermal wave-front distortion techniques depend on the sample geometry and thermophysical properties, *dn/dt* and C_p. For optimal cases with small V_h and suitable thermophysical properties, P_{min} can be made small.

Absorption measurements of single nonfluorescent azo dye molecule have been reported using photothermal wave-front distortion technique in glycerol (with large *dn/dt* and poor heat conduction) [32]. Glycerol has a *dn/dt* of 2.7×10^{-4} K^{-1} [33], which is more than one order of magnitude larger than the thermo-optic coefficient of a Corning 7980 fused silica substrate with $dn/dt = 9.25\times10^{-6}$ K^{-1} at 500-nm probe wavelength [34]. Detection of P_{min} as small as 64 pW was possible by using Xenon gas as the medium instead of glycerol [33]. This experiment was conducted at temperatures and pressures near the critical point of Xenon (T=16.583 °C, P=5.842 MPa) where *dn/dt* is extremely large ($dn/dt \sim 4\times10^{-2}$ K^{-1}). By choosing Xenon, which has a relatively low thermal conductivity and C_P, the volume of the heat affected zone was kept small (< 1 μm^3) resulting in very small C_h. However, many practical absorption measurement problems associated with material characterization cannot meet all of these restrictions.

The sensitivity of photothermal wave-front distortion techniques relies on the photothermal material properties. However, there are materials, such as many laser or nonlinear optical materials, which have very small *dn/dt* and so there is a lack of sensitivity to detect very low absorption losses. Mounting these samples on another material with large *dn/dt* is possible but results in an increased effective heat capacity.

The absolute calibration of the absorption measurement is a challenging problem for all the photothermal wave-front distortion techniques [35]. To determine the absolute absorbance of a test sample with photothermal wave-front distortion techniques, a reference sample of the same material and geometry with known absorption coefficient and thermal properties is typically used. This makes absolute sample absorption measurements difficult. Problems arise if the thermo-optical properties of the material are not known.

In another sensitive photothermal approach, the heating of the sample is probed with a microfabricated optomechanical or optical resonator whose resonance shifts with temperature [36], [37]. For example, when a probe laser hits the absorbing center, the absorption-induced local heating causes a heat flux into a drum resonator, and the resulting thermal expansion reduces the stress of the drum. As a result, the mechanical resonance frequency of the drum changes and the absorption cross-section of the attached single nanoparticle can be deduced after proper calibration. Recently a nanomechanical drum resonator was used as a temperature sensitive element for single nano-particle and single molecule imaging and an absorbed power of 16 fW/√Hz was measured at an optimal integration time of 40 ms [36]. This approach has also been demonstrated with optical whispering-gallery-mode (WGM) microresonators with ultrahigh-quality-factors, where the photothermal shifts in the resonance frequency acts as the micron-scale thermometric element [37]. Figure 1.3 shows the schematic of such a spectrometer and the frequency shift in the resonance frequency of the WGM microresonator.

These approaches work well when a single absorbing particle can be placed in thermal contact with the micron-scale thermometric element. The technique works well

with nano-scale samples with very small heat capacity ($C \sim$ nJ/K). Single particle sensitivity cannot be realized for macroscopic samples with orders of magnitude larger heat capacity. For example, the heat capacity of fused silica is about $C \approx 1$ mJ/K for 1 mm^3 at room temperature.

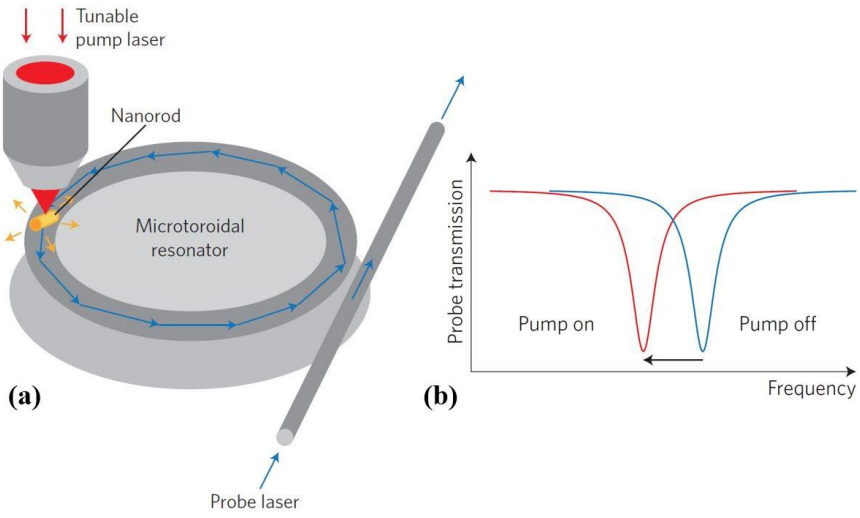

Figure 1.3: Combination of the whispering-gallery-mode sensing with photothermal absorption spectroscopy. (a) A pump–probe beam arrangement is used to illuminate a plasmonic nanorod resonantly, causing the nearby microcavity to heat up. (b) The generated photothermal absorption signal shifts the resonance frequency of the microresonator. Graphics taken from [38].

1.2.2 Optical Calorimetry at Room Temperature

Calorimetry is the oldest technique among the photothermal techniques, dating back to the 18th century when the concepts of latent heat and heat capacity were introduced [39]. Figure 1.4 shows a basic schematic of a calorimeter. A calorimeter in general consists of an absorber, a temperature sensor, and a thermal link with thermal resistance R_L to a

thermal bath T_B. Assuming a strong thermal contact between the absorber and thermometer, the two components can be lumped into one heat capacity C_S and temperature T_S.

In such a calorimeter, the absorber or absorbing sample is subjected to a laser beam (or any excitation source) with known incident power. During the illumination time, energy of the laser beam is converted into heat by absorption, and the absorption-induced temperature rise of the sample under investigation is directly measured with the temperature sensor.

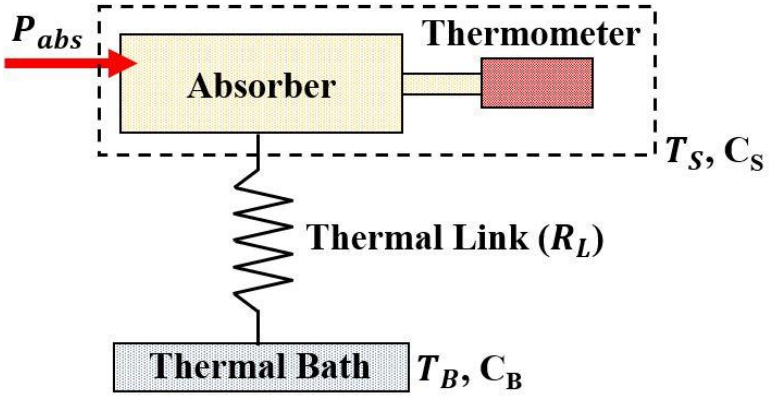

Figure 1.4: Schematic view of a simple calorimeter. The "thermal bath" here is an element with large heat capacity whose temperature is constant.

Assuming the time constant $C_S R_L$ to be much larger than the time constant between the absorber and the thermometer, temperature gradient is negligible within the thermal mass with heat capacity C_S and the temperature rise of the absorber can be estimated according to a lumped-capacitance model. The heat balance equation for such a calorimeter can be written as:

$$\frac{dT_S}{dt} = \frac{P_{abs}}{C_S} - \frac{T_S - T_B}{C_S R_L} \tag{1.6}$$

$$\frac{dT_B}{dt} = -\frac{T_B - T_S}{C_B R_L} \tag{1.7}$$

where T_S is the time-dependent temperature of the absorber, P_{abs} is the absorbed power by the absorber and C_B is the heat capacity of the thermal bath. The thermal capacities C_S and C_B and thermal resistance R_L have similar meaning as capacitance and resistance in electrical circuits. Subtracting Eq. (1.7) from Eq. (1.6) yields:

$$\frac{d(T_S - T_B)}{dt} = \frac{P_{abs}}{C_S} - \left(\frac{1}{C_S} + \frac{1}{C_B}\right)\frac{T_S - T_B}{R_L} \tag{1.8}$$

The thermal time constant $\tau = R_L C_{eff}$ can be introduced, where $C_{eff} = (\frac{1}{C_S} + \frac{1}{C_B})^{-1}$ is the effective heat capacity of the two-mass thermal system. In most cases, $C_B >> C_S$ and so the $C_{eff} \approx C_S$. For simplicity, it can be assumed that absorber and thermal bath have the same temperature before the illumination starts and so the temperature rise in the absorber $\Delta T = T_S - T_B$. In terms of ΔT, Eq. (1.8) can be written as:

$$\frac{d(\Delta T)}{dt} + \frac{\Delta T}{\tau} = \frac{P_{abs}}{C_S} \tag{1.9}$$

With the initial condition of $\Delta T(t=0) = 0$ and assuming that a constant optical power is turned on at $t = 0$ the solution is:

$$\Delta T(t) = \frac{P_{abs}}{C_S}\tau\left(1 - e^{-\frac{t}{\tau}}\right) \tag{1.10}$$

Two simplifying limits determined by the ratio of the thermal time constant τ to the duration of the optical excitation Δt, can be considered: pulsed and continuous illuminations. For short-pulse illumination $\Delta t << \tau$ Eq. (1.10) simplifies to:

$$\Delta T(\Delta t) = \frac{P_{abs}(\Delta t)}{C_S}\Delta t \tag{1.11}$$

Here P_{abs} and ΔT are the absorbed power and temperature change at the end of the pulse duration Δt. In this case, the heat capacity of the absorber and thermometer C_S are the key factors in determining the sensitivity of the experiment.

For continuous illumination, $t >> \tau$, and Eq. (1.10) simplifies to:

$$\Delta T(t) = P_{abs} R_L \tag{1.12}$$

The magnitude of this time independent temperature change, which determines the sensitivity of the calorimeter, is controlled by the absorbed power and the thermal resistance R_L. It is clear that thermometers with small ΔT_{min} are required for measurements with high sensitivity.

In contrast to the photothermal wave-front distortion techniques, which need a rather complicated approach for calibration, calorimetry allows for relatively simple and straightforward calibration methods. An absolute calibration (dissipated power vs. measured temperature change), can be achieved using electrical heaters without any prior knowledge of sample parameters. Also, compared to photothermal wave-front distortion techniques, calorimetry does not require critical alignment of a probe and wavelength tunable pump beam. These are the reason why calorimetry has become an ISO standard method for measuring the absolute absorbance of optical laser components [40].

According to Eq. (1.11) and Eq. (1.12), to detect the lowest measurable absorbed power (P_{min}), which defines the resolution of a calorimeter, – (i) ΔT_{min} should be small, (ii) C_S should be small, and (iii) R_L should be large in particular for continuous illumination.

Figure 1.5 shows a schematic diagram of a simple calorimeter and a typical result of a laser calorimetric measurement conducted at room temperature.

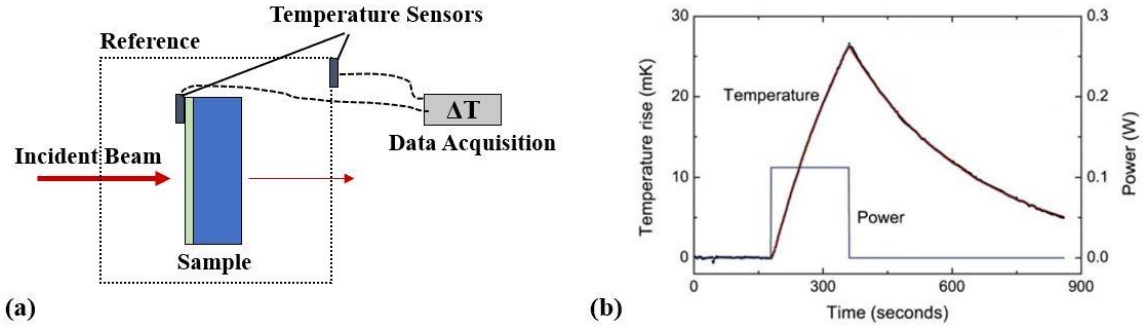

Figure 1.5: A typical example for a laser calorimetric measurement. The sample is a highly reflective mirror irradiated at 193-nm with an average irradiation power of 114 mW and illumination time of 180 s. Figure (b) is reproduced from [41].

The calorimetry technique has been used at both room temperature and low (cryogenic) temperature. The sensitivity of optical calorimetry is ultimately determined by the temperature change of a weakly absorbing sample (incl. instrumentation) that one can measure for a given optical excitation power. It is therefore dependent upon the sensitivity of the thermometer and the heat capacity of the absorber or the thermal resistance between absorber and thermal bath (depending on illumination mode). In room temperature calorimeters, high sensitivity thermistors are often the thermometers of choice. These temperature sensors have demonstrated a temperature resolution of a few ten μK [42]. For pulsed illumination with an irradiation time of 100 s and a sample (incl. instrumentation) heat capacity of about 2 J/K, a 50-μK temperature resolution enables minimum detectable absorbed power P_{min} of 1 μW, which translates to an absorptance of about 1 ppm using average excitation powers of the order of one Watt [41]–[43]. The inherent Johnson noise of the thermistors is one of the limiting factors to achieving better temperature resolution. This can be improved by increasing the applied power to the sensor, but then self-heating

places a limit on the sensitivity of the thermistor [44], [45].

1.2.3 Optical Calorimetry at Cryogenic Temperature

Cryogenic temperature calorimetry was pioneered by Eucken [46] and Nernst [47] in the early 20th century. They used a calorimeter to determine specific heats at cryogenic temperatures. It was in the early 1980s that low temperature calorimetry began to be applied for optical absorption spectroscopy [48]. As we will explain next the advantages of calorimetry and cryogenic temperatures are: (1) the energy resolution improves by going to cryogenic temperatures, (2) the heat capacity of materials decreases at cryogenics temperatures, and (3) temperature sensors with high resolution can be employed at cryogenic temperatures.

Fundamental limit, energy resolution – For a calorimeter such as the one depicted in Fig. 1.4, the energy of the system including the absorber and the thermometer, with heat capacity C_S and at a non-zero temperature, fluctuates due to random energy exchange with the thermal bath. These fluctuations have a standard deviation of the form [49]

$$\sigma_E = \sqrt{k_B T^2 C_s} \tag{1.13}$$

where k_B is the Boltzmann constant, and T is the temperature at which the experiment is conducted. The energy resolution can be defined as Full Width Half Maximum (FWHM) of the Gaussian fit to the peak in energy spectrum and it can be written as:

$$\Delta E_{FWHM} = 2.36\sqrt{k_B T^2 C_s} \tag{1.14}$$

The derivation of this expression can be found in appendix A. This equation shows that the

energy resolution of such a calorimeter depends linearly on the operational temperature.

Technical limit, heat capacity - Optical calorimetry at cryogenic temperatures can also take advantage of the fact that the heat capacity of materials decreases at cryogenics temperatures [50]. As an example, Fig. 1.6 shows the specific heat (heat capacity per unit mass at constant pressure) of some commonly used materials from room temperature to ~4 K. The figure shows that below ~100 K the specific heat decreases rapidly, falling approximately as T^3 in most of these materials as expected from the Debye model.

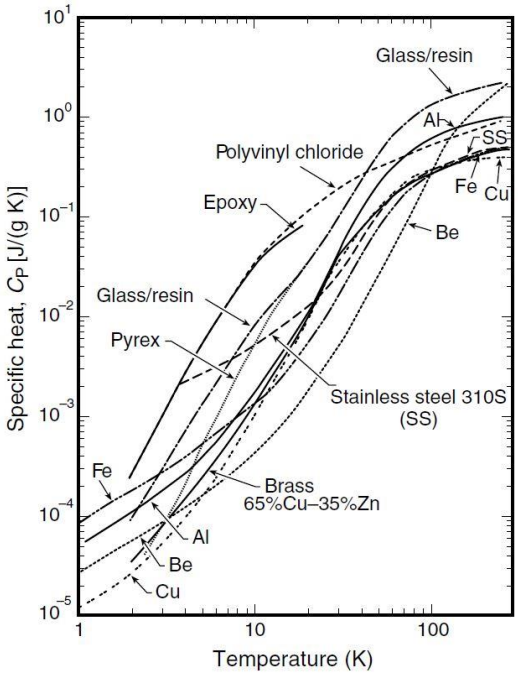

Figure 1.6: Specific heat capacity (heat capacity per unit mass at constant pressure, C_P) for some materials at cryogenic temperatures. From [50].

Smaller heat capacity means less energy is needed to get the same temperature increase. According to Eq. (1.11), this will decrease the minimum detectable absorbed power and thus increase the absorption sensitivity. For instance, the heat capacity of fused silica at 4 K is about 10^3 times smaller than at room temperature (for 1-mm^3 of fused silica

for example, $C \approx 1$ μJ/K at 4 K), which means the temperature rise at 4 K for the same dissipated power would be 10^3 times larger than at room temperature.

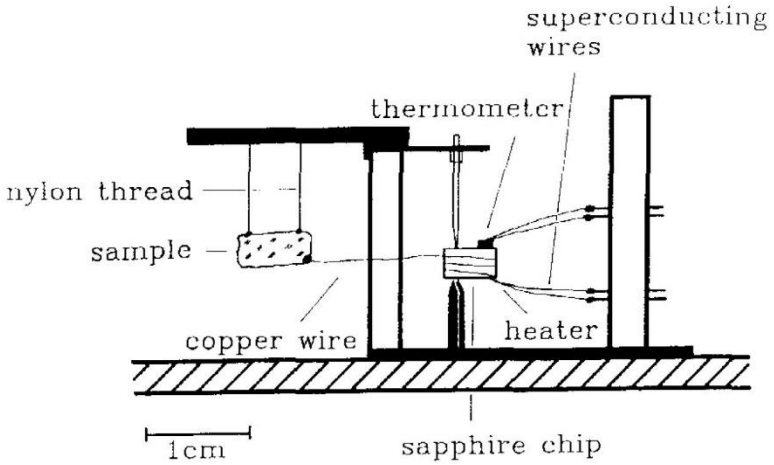

Figure 1.7: Sample/calorimeter arrangement for calorimetric absorption spectroscopy at 45 mK. To enhance the thermal isolation of the sample, nylon threads with extremely low thermal conductivity (large R_L in Fig. 1.4) were used. A sapphire chip with very small heat capacity at low temperature was employed to support sample and heater. The heater was used for calibration purposes to measure the heat power dissipated in the sample quantitatively. A copper wire provides the thermal coupling between the sample and sapphire chip. Superconducting wires are used for electric connections to minimize the heat flow through the wires. From [56]. In this instrument the heat capacity C_S is the sum of the sample and the sapphire chip holding the thermometer.

Early low temperature optical calorimeters have taken advantage of this fact. By going to the lowest achievable temperature in the cryostat researchers have tried to improve the minimum detectable absorbed power P_{min} [48], [51]–[58]. A P_{min}=0.1 pW has been reported in a ^{3}He/^{4}He dilution cryostat held at 45 mK for several weeks [56]. Figure 1.7 shows the sample/calorimeter arrangement for such an experiment. To further decrease C_S the instrument relied on samples and holders with extremely small heat capacity and excellent thermal isolation from the rest of setup. Hence, a minimum temperature change of ΔT_{min}=15 μK, whose detection is possible with thermistors, was sufficient to achieve

such a small P_{min}. Their highest possible irradiation power was limited by the cooling power of their cryostat at 45 mK and could not be more than 1 µW. This translated into limits for absorptance measurements on the order of $A_{min} \approx 0.1$ ppm.

Technical limit, high resolution thermometry - Another reason for going to cryogenic temperatures is that thermometers with high sensitivity can be utilized. Although previous low temperature calorimeters used different types of resistance temperature detectors (RTDs) like ruthenium oxide and carbon resistance thermometers, which improved sensitivity [54], [56], the ΔT_{min} improved only by a few µK to about 15 µK.

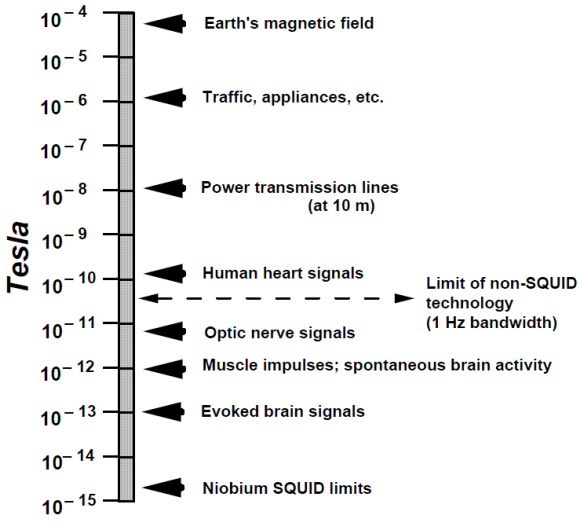

Figure 1.8: The SQUID limits compared to magnetic fields of different sources. Image taken from [62].

Paramagnetic sensors with Superconducting Quantum Interference Device (SQUID) read-outs have shown impressive temperature dependencies, which can be exploited for High Resolution Thermometers (HRTs) [59]–[61]. The SQUIDs are the most sensitive detectors of magnetic field and can detect the tiny magnetic signals generated by

the human brain for example. Figure 1.8 shows the magnetic field levels of different sources compared to the detection limit of the best niobium SQUIDs.

By taking advantage of SQUID sensitivities, HRT devices have demonstrated noise limited resolution of better than 100 pK/√Hz near 1 Hz at 2.2 K [63], [64]. These paramagnetic sensors are made from materials whose magnetic susceptibilities are strongly temperature dependent. They are placed in a constant magnetic field to take advantage of SQID readout technology to detect small temperature induced susceptibility changes. In calorimeter applications, when the temperature of the absorbing sample and paramagnetic sensor increases in proportion to the absorbed power, the magnetization of the sensor decreases. This magnetization change can be read out by the SQUIDs, and with proper calibration one can find the temperature change of the absorbing sample. This will be described in Chapter 3 in more detail.

The disadvantage of employing SQUID based HRTs to measure the optical absorption of non-fluorescing samples, arises from (i) the requirement of cryogenic temperatures, (ii) the need for complex instrumentation to go to cryogenics temperatures, and (iii) the fact that the material properties are measured at cryogenic temperatures from which room temperature behavior is extrapolated. However, in principle, sensitivities can be reached that would allow for the detection of single absorbing centers in macroscopic samples with only milli-Watts of excitation power. This is particularly attractive if the absorption measurement is to be performed over a broad spectral range. Low-power tunable sources are readily available.

1.3 Thesis Goals

The main research goals of this thesis are:

1. To develop, design and build an optical calorimeter with a top-access experimental stage capable of reaching a cryogenic temperature of ~4 K in less than 15 hours using a pulse-tube refrigerator.
2. To provide a well-controlled thermal environment for the specimen to permit measurements of very small temperature changes (≤ 10 nK).
3. To employ paramagnetic sensors with SQUID readouts as temperature sensors to detect the absorption-induced temperature change of the sample with nK temperature resolution.
4. To conduct a direct measurement of nonradiative optical absorption, which is calibrated with an electric resistor, and to obtain an absorbed power sensitivity of a few pW which then enables us to detect absorption sensitivities below 1 ppm level for just a few ten μW of excitation powers.
5. To evaluate the developed optical calorimeter as a tool to measure the absorption spectrum of transparent optical substrates and optical thin films.

1.4 Thesis Outline

Chapter 2 describes the design of a custom-built U-shaped cryogen-free cryostat cooled by a commercial pulse-tube refrigerator to 4 K. A comprehensive thermal modelling

with COMSOL Multiphysics will be presented, which was employed to optimize the cryostat design for fast cooldown to 4 K of the base plate that houses the optical setup. At the end of this chapter, the simulation results for cooldown will be compared to experimental results.

Chapter 3 describes the experimental setup for an ultra-sensitive absorption measurement and the thermal network of the absorption measurement. The necessary optical mechanical components are introduced and the basic concept of the paramagnetic sensor with SQUID read-out are discussed.

Chapter 4 describes the data acquisition system, including the hardware and software configurations, developed for this work. A routine analysis for estimating the absolute absorption of a sample will be discussed at the end of this chapter.

Chapter 5 describes the achieved sensitivity and characterizes fundamental and technical noise of the instrument.

The work presented in Chapter 6 focuses on the application of the developed pico-Watt calorimeter to the study of high-purity optical samples.

Chapter 7 provides a summary of the dissertation and the outlook for future work.

Chapter 2

Design and Test of a Custom-Built Cryostat

To perform optical absorption spectroscopy with the desired sensitivity, it is necessary to cool the experimental setup down to very low temperatures. The goal of this chapter is to describe the design, construction, and test of a cryostat, in which a specimen (sample) will reside at a low cryogenic temperature of ~4 K.

2.1 Design Objectives

The design and construction process of a research cryostat for a particular

measurement is unlike the one used for commercial manufacturing. To have a cryostat suitable for sensitive calorimetric absorption spectroscopy, several requirements have to be satisfied:

1. The first definitive factor in design is the temperature range of interest. This work exploits the extraordinary temperature resolution that can be obtained with High Resolution Thermometers (HRTs) at low temperatures. For best performance, the experimental stage should reach a temperature low enough for low-Tc SQUIDs to operate, which is approximately 5 K [65]. The performance can be further improved by cooling the experimental stage to temperatures lower than 5 K, to further decrease heat capacities and thermal noise sources.
2. For cooling down the experimental stage to temperatures below 5 K, mechanical refrigerators such as a pulse tube cooler (PTC) are desired as a source of refrigeration [66], [67]. Non-usage of expensive liquid cryogens, such as liquid helium, and the advantage of possible long continuous measurements make cryogen-free cryostats an increasingly popular choice for research.
3. For optical illumination of the specimen, the (tunable) light source should be fiber coupled, and suitable fiber ports need to be incorporated into the cryostat design.
4. Propagation of mechanical vibrations to a cryostat, with a mechanical refrigerator as the source of refrigeration, is a very well-known problem. This problem needs to be addressed in order to provide a quiet (low noise) environment for sensitive measurements at low-temperature.

To have a user friendly apparatus, some other factors need to be considered in the cryostat design:

I. In terms of mechanical and geometric design, the cryostat should possess an experimental stage (base plate) at 4-5 K that can be accessed from the top.
II. The cryostat needs to be compact so that it can be mounted on a standard optical table for integration with a various light sources.
III. The cool-down time of the cryostat should not exceed 15 hours to allow for overnight cooling. To accomplish this, heat-transfer calculations can aid in material selection and construction.
IV. The design needs to be flexible to permit the installation of optical entrance and exit windows in the future if high excitation power (e.g. a few Watts) is desirable.

2.2 Cryostat Design and Construction Approach

The mechanical refrigerator used for this work is a two stage pulse tube cooler (PTC), PTD406-RV by TransMIT Center for Adaptive Cryotechnology and Sensors, with a base temperature of 2.2 K [68]. The cryocooler provides simultaneous cooling powers of 20 W for the PTC's 1st stage at ~60 K and 0.6 W for the PTC's 2nd stage at ~4 K. The basic operation of a pulse tube cooler is explained in appendix B.

2.2.1 Main Components

Figure 2.1 shows the principal layout of our optical cryostat. It consists of a cryostat with a PTC and a baseplate kept at about 4 K, on which the components of the measurement chamber are mounted. Light is coupled to the sample to be characterized through an optical multi-mode fiber and can be turned on and off using an electromechanical shutter (MS). The U-shape allows the PTC to stay in its required gravity-dependent orientation with the base plate in standard horizontal orientation.

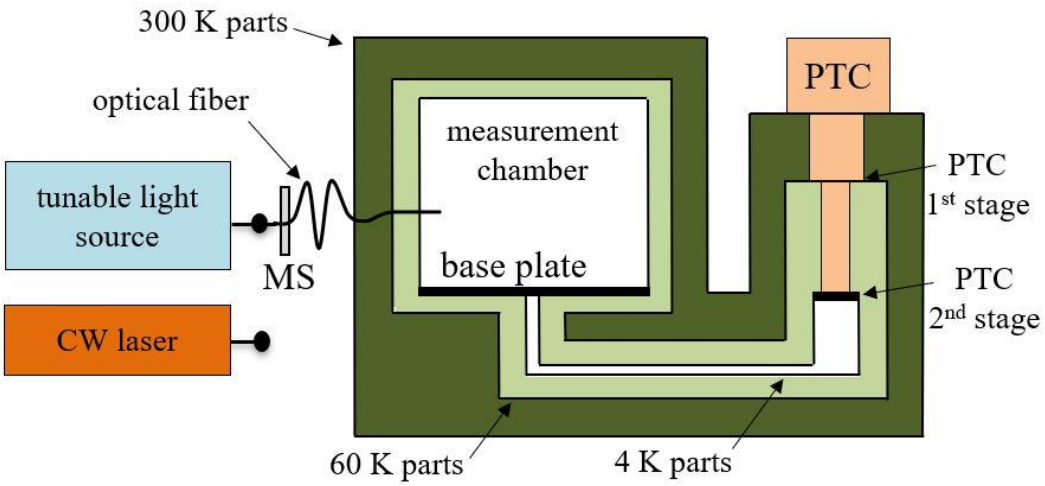

Figure 2.1: Schematic diagram of the main units of the cryostat with outer shell (300 K), middle shell (60 K), and inner units (4 K). PTC: pulse tube cooler, MS: electromechanical shutter. A tunable light source or a laser at selected wavelength can be used as the source of excitation. The PTC 1st stage has a nominal operating temperature of 60 K, while its 2nd stage has a nominal operating temperature of 4 K. Parts with nominal temperature of 60 K and 4 K are thermally connected to the 1st and 2nd stages of the PTC. The measurement chamber houses the sample and the low temperature experimental setup.

The cryostat consists of three major building blocks held at temperatures of about 300 K, 60 K and 4 K, respectively. The first segment is the outer shell, which provides

mechanical support for the whole structure and acts as a vacuum chamber for the inner parts with nominal temperatures of 60 K and 4 K. The reason behind a multi-shell design will be explained in the next section. To maximize the performance of a cryostat, good thermal isolation between stages with different temperatures is required. Thus, it is necessary to operate the cryostat under vacuum to avoid thermal conduction due to gases.

The details of the calorimeter design will be given in the rest of this section.

2.2.2 Details of the Design

The cryostat was designed with the help of Creo Elements/Pro software. Figure 2.2 shows the finalized design of the cryostat. The vacuum-insulated shell (outer shell) is comprised of an aluminum box-shaped base unit, an aluminum cylinder (300 K shell) and a stainless steel PTC support shell. The support unit is 79 cm by 20 cm by 10 cm. The aluminum cylinder with the outer diameter and height of 32.4 cm and 38.5 cm, respectively, is large enough to accommodate the measurement chamber. The choice of materials will be explained later. The PTC support shell is connected to the top flange of the PTC and provides mechanical support for it.

The aluminum base supports the whole cryostat and can be bolted to an optical table. The openings in the bottom and two sides are needed for the cryostat assembly and can be sealed hermetically with aluminum plates and O-rings. The inner unit includes a 4-K radiation shield, the 4-K base plate, the 4-K bar and the 2^{nd} stage flexible thermal link, see Fig.2.2. The 4-K radiation shield and the 4-K base plate form the measurement chamber, where the sample and detectors reside.

All surfaces emit heat. In a cryostat where we have great temperature differences between various parts of the cryostat, the thermal radiation can be a large source of the heat leak into the cryostat. An obvious question therefore is how to minimize this heat flow.

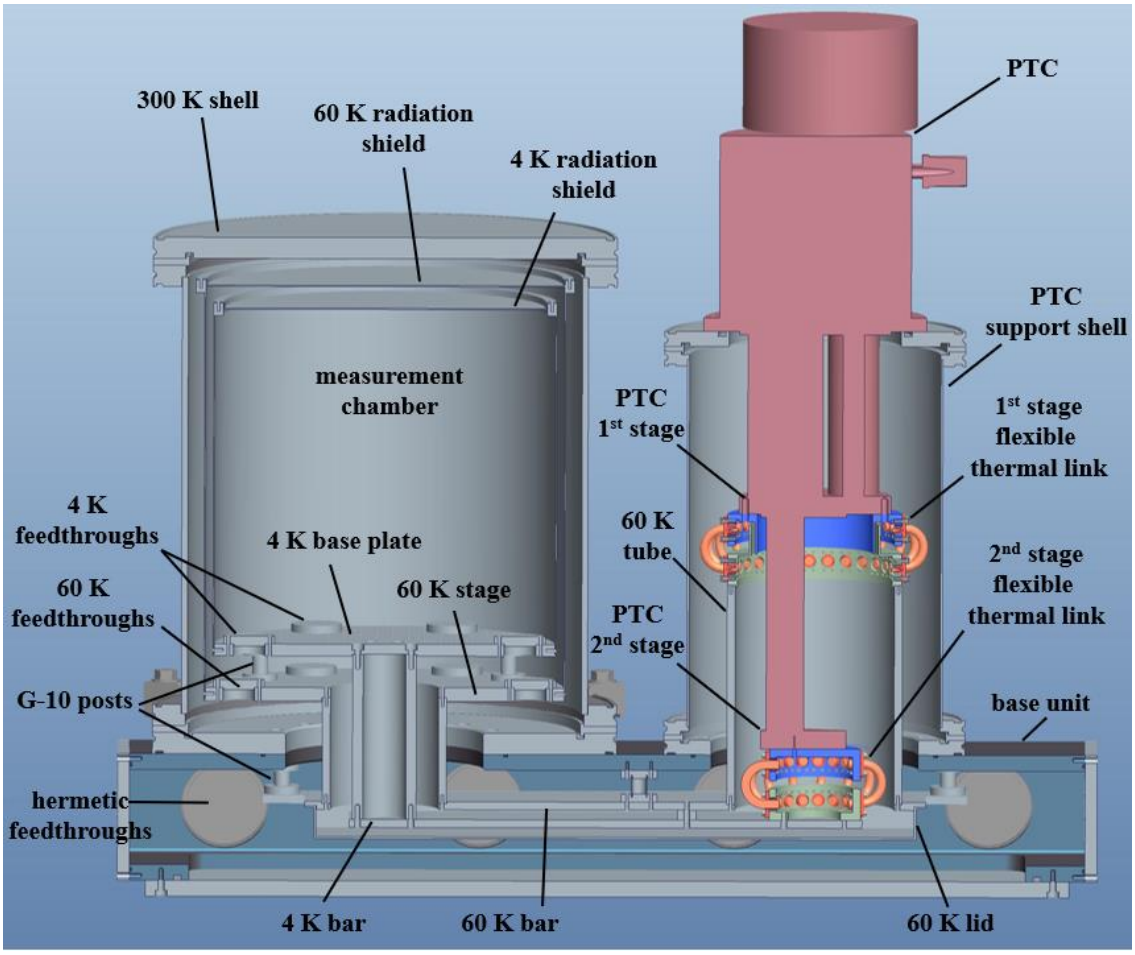

Figure 2.2: Cross section of the actual cryostat design. 60-K components surround the 4-K parts to reduce the radiative heat load. Hermetic feedthroughs are O-ring sealed flanges for the entrance of the fiber optic cable and the electric wiring. The cold stages and thermal links are supported by hollow rods of fiberglass-reinforced epoxy G-10 which have very low thermal conductivity. Flexible thermal links are designed to provide high thermal conduction and flexibility at the same time.

There are several approaches that one can utilize to reduce the radiation heat leak

into the sensitive parts of the cryostat. The radiative heat flow P_r from a surface is given by the Stefan–Boltzmann equation,

$$P_r = \varepsilon\sigma \mathrm{A} T^4, \tag{2.1}$$

where ε is the emissivity of the surface at temperature T, A is the surface area, and σ is the Stefan–Boltzmann constant [5.67×10^{-8} W/(m^{2}K^4)]. To minimize radiative heat transfer from the 300-K shell to the experiment two design features were implemented – A and B.

A. An intermediate-temperature refrigerated stage and radiation shield was incorporated to intercept the radiative heat flow from the vacuum shell (with nominal temperature of 300 K) impinging on the cold stage of a cryostat (e.g. base plate at 4 K in our design). A two-stage PTC is suitable for our purpose, where the 1st and 2nd stages operate at roughly 60 K and 4 K, respectively. In this design, the 60-K shell surrounds the 4-K inner chamber. Hence, the 4-K components are only exposed to the thermal radiation from the 60-K surfaces and are shielded from radiation from the 300-K outer shell (vacuum shell). The 4 -K radiation shield reduces the radiative heat load on the experimental setup.

B. The radiative heat transfer depends on the emissivity of the cold surfaces ε_{cold}, which for an opaque material is related to the cold-surface reflectance R_{cold} by $\varepsilon_{cold} = 1\text{-}R_{cold}$. Thus we reduced the emissivity of the parts at lower-temperature so that the radiation from higher-temperature parts are mostly reflected. This is achieved by gold and nickel plating the lower-temperature parts and wrapping those parts with high-reflectivity materials. This will be discussed in more details later in this chapter.

In what follows we will describe further design components sketched in Fig.2.2.

Hermetic feedthroughs: Five hermetic feedthroughs on each side of the base unit are for (i) the fiber optic cable, (ii) electric wires, (iii) vacuum pump, (iv) pressure monitoring, and (v) the SQUID cryo-cable. All feedthrough cables are connected to the 60-K stage to prevent direct thermal contact between the outer, 300-K shell and the 4-K base plate.

O-ring sealed ISO-63 KF flanges are used as standard installation mountings for hermetic feedthroughs. The ISO-63 flanges can be modified or replaced by commercially available feedthroughs to accommodate the desired feedthrough with a specific need.

Flexible thermal links: Flexible thermal links are designed and constructed for several reasons:

1. At low temperatures almost all materials change size (most shrink). Hence, differential thermal-contraction forces can build up between the PTC stages and thermal loads (attached to them). Soft heat links are needed for operating the PTC apparatus in a stress-free manner.

2. Strong thermal conduction between the PTC stages and the cold stages is needed to not lessen the cooling capacity of the refrigeration system.

3. Soft mechanical links are needed to attenuate the transmission of the PTC induced mechanical vibrations to the 60-K stage and 4-K base plate. The mechanical vibrations attributed to the PTC will be discussed in detail later. Such thermal links have been previously used by other groups to minimize the mechanical coupling [69], [70]. Figure 2.3(a) shows a picture of the 1st stage flexible thermal link bolted to the PTC 1st

stage and 60-K tube. Figure 2.3(b) shows the bottom view of the 2nd stage flexible thermal link which is bolted to the PTC 2nd stage. The 1st stage and 2nd stage flexible thermal links are made of 24 and 14 copper braids respectively, with their ends welded to copper blocks which are then bolted to the PTC stages and the thermal links. Each copper braid has a cross section of ~0.06 in^2 and a length of 2 in. To increase the thermal conductivity and the flexibility of the thermal links, the copper braids (after welding to copper blocks) are annealed at 1000℃ under high vacuum for about 12 hours.

According to the Wiedemann-Franz law the ratio of thermal conductance K to electrical conductance G is proportional to the temperature T and can be expressed as [50]

$$\frac{K}{G} = LT, \tag{2.2}$$

where $L = 2.44\times10^{-8}$ $W.\Omega.K^{-2}$ is the Lorenz number.

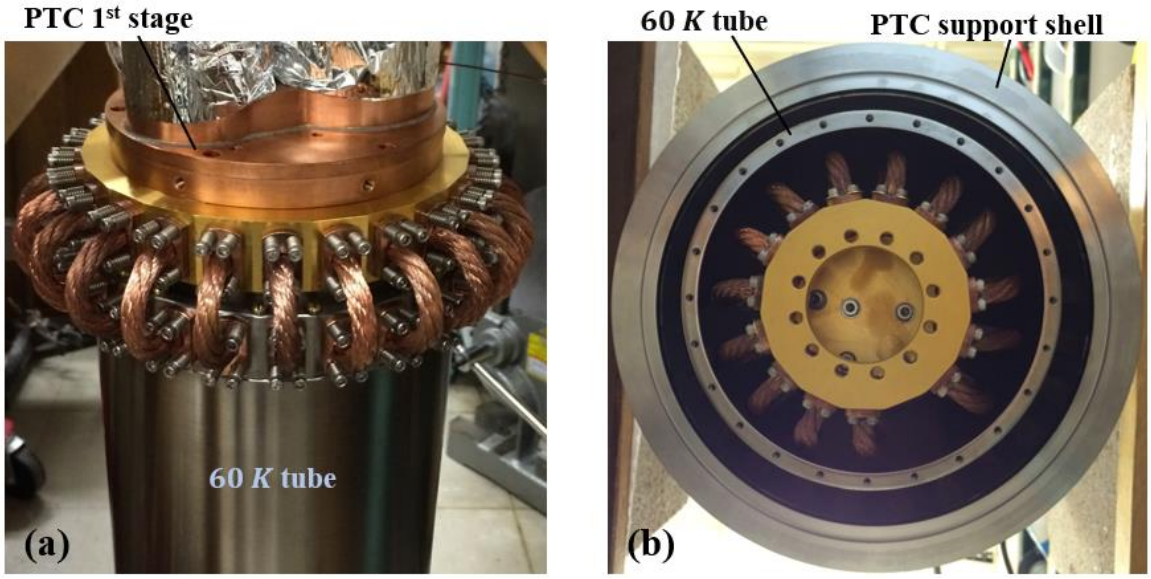

Figure 2.3: (a) Side view of the 1st stage flexible thermal link bolted to the PTC 1st stage and 60-K tube, (b) Bottom view of the 2nd stage flexible thermal link.

We have measured an electrical conductance of ~1.4×10^{4} Ω^{-1} at 4.2 K temperature for the copper braid with the 4-lead sensing method (two for current and two for voltage sensing). According to Eq. (2.2) this yields a thermal conductance of ~1.4×10^{-3} $W.K^{-1}$ for each copper braid. To increase the thermal conductance across the joint interfaces, a thin (0.005-inch thick) indium foil is placed between the two parts before bolting them together. The indium foil cold-welds the parts together and fills gaps between the two surfaces [50]. The inner diameter of the 60-K tube connected to the 1st stage flexible thermal link, is big enough to accommodate the 2nd stage flexible thermal link. As one can see in Fig. 2.3(b), the 2nd stage flexible thermal link is very well centered inside the 60-K tube and has enough wall clearance.

The thermal conductance across an interface of two materials increases approximately linearly with pressure while the contact area of the two pressed surfaces does not play a crucial role [50]. Thus, applying a high force when pressing the two surfaces together, provides a good thermal connection between two solid surfaces. For bolting our two parts together, screws in combination with soft springs or Belleville disc springs are employed to produce a large enough pressure.

Fiberglass-reinforced epoxy G-10 posts: The 60-K tube, the 60-K radiation shield and other 60-K components in between, are made of aluminum and are structurally supported by several G-10 posts attached to the base. The 4-K components are connected similarly to the 60-K shell. Figure 2.4 shows a G-10 post used in the cryostat for mechanically supporting the cold stages and thermal links at lower temperatures. A G-10 post is made of a fiberglass-reinforced epoxy G-10 tube glued (using Stycast 1266™

epoxy) to two aluminum disks.

Fiberglass-reinforced epoxy G-10 material has excellent tensile and impact strength and has extremely low thermal conductivity and thermal contraction at temperatures near 4 K [71], which makes it an ideal material for the mechanical structure at low temperatures. Stycast 1266™ is an unfilled epoxy with high impact strength and low viscosity that works very well at low temperatures [50].

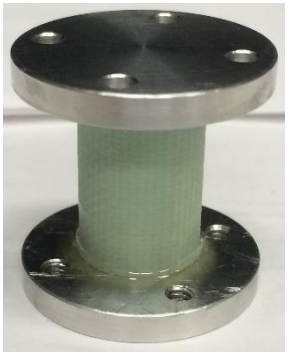

Figure 2.4: A G-10 post is used in the cryostat for mechanically supporting the cold stages and the thermal links at lower temperatures.

4-K base plate: Figure 2.5 shows the 4-K base plate, which serves as an optical table at low temperature (4 K). This base plate needs to be big enough to accommodate the optical and mechanical components, such as a sample holder for holding macroscopic test samples, a coupling/collimating assembly for the optical fiber, a beam dump, and instrumentation for one or more High Resolution Thermometers (HRTs). The 4-K base plate has a diameter of ~28 cm and it is mechanically supported by the 60-K stage via three G-10 posts. Similarly, the 60-K stage is mechanically supported by the base unit. The circular openings (1-inch diameter) on the 4-K base plate and the 60-K stage are the

entrance for the optical fiber, wires, and cables. There is a bolt pattern around the 4-K base plate (60-K stage) for attaching the 4-K radiation shield (60-K radiation shield) to it.

4-K and 60-K feedthroughs: Custom flanges are fabricated to provide light-tight feedthroughs for these components. These feedthroughs can be bolted to the 4-K base plate and the 60-K stage.

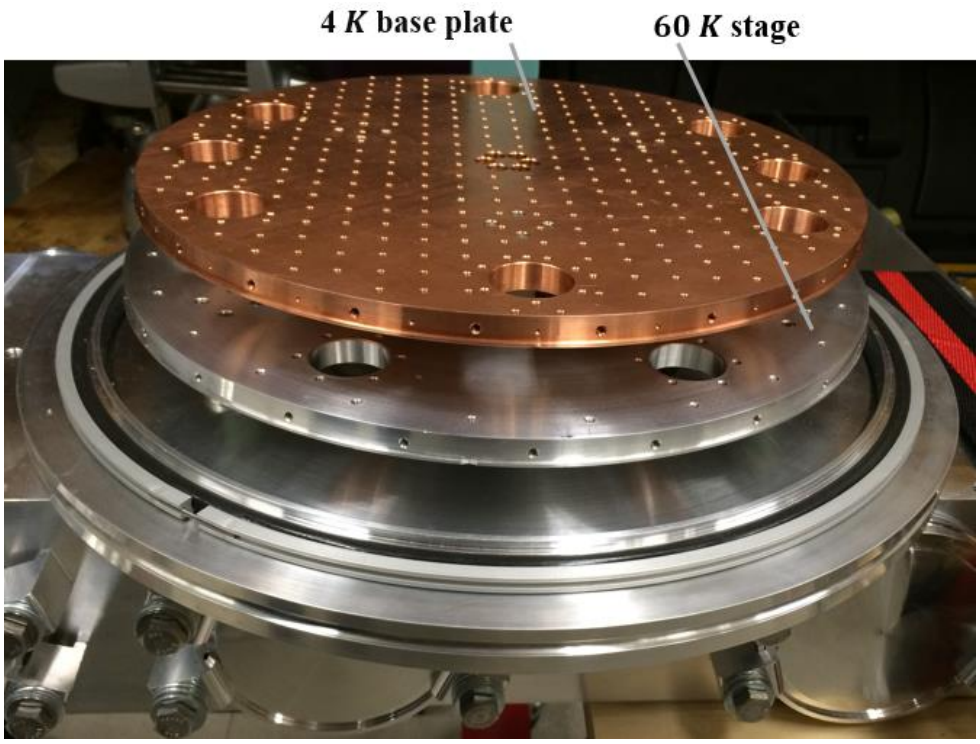

Figure 2.5: The 4-K base plate mechanically supported by the 60-K stage.

4-K bar & 60-K bar: The 4-K bar (60-K bar) is the intermediate thermal link between the 4-K base plate (60-K stage) and the 2nd stage (1st stage) of the PTC. One can realize that by attaching the 60-K lid to the 60-K bar, the 4-K bar is completely enclosed by parts with a nominal temperature of 60 K and not 300 K. So, the radiative heat load is

reduced as discussed in the beginning of this chapter.

Figure 2.6 shows a bottom view of the custom cryostat where the O-ring-sealed aluminum plate is removed from the base unit to provide access to the cryostat for assembly purposes. Also, the 60-K lid is removed so that the 4-K bar becomes accessible. The groove cut around the circumference of the opening is to accommodate a standard size Viton® Fluoroelastomer O-Ring. When the aluminum plate is bolted to the base unit, the O-ring is compressed enough to provide a vacuum seal.

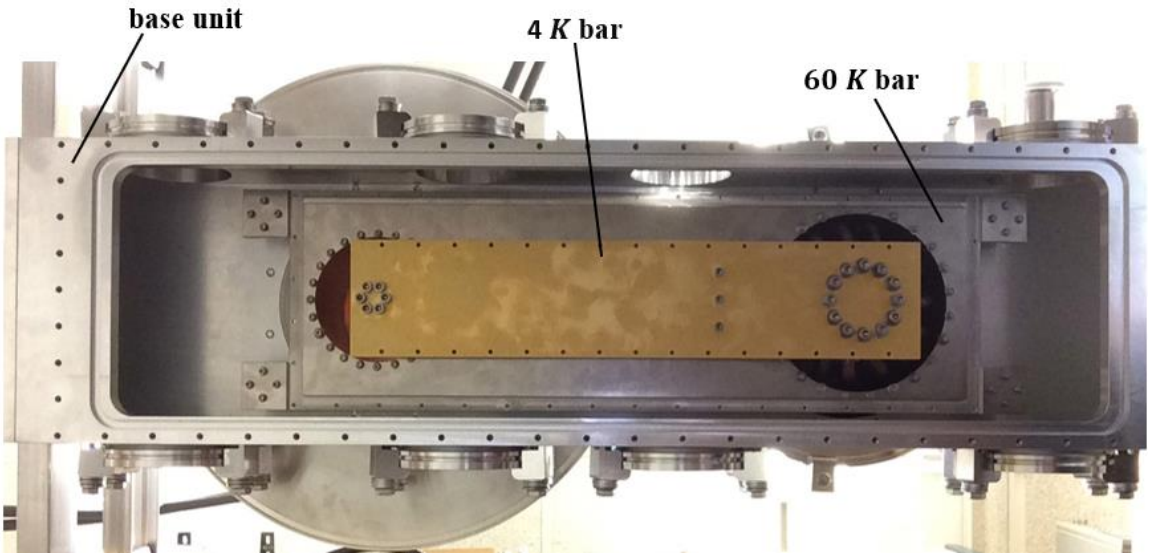

Figure 2.6: A bottom view of the custom cryostat.

Material and coating selection for 60-K and 4-K parts: Since the 4-K base plate is our experimental stage at low temperature and the temperature needs to be as homogenous as possible across the whole stage, the base plate is made from high-conductivity copper (copper alloy 101). The heat transfer across the contact between two different metals is a common problem in low-temperature applications where the thermal

boundary resistance at the interface between two materials becomes increasingly important [72]. To lessen this problem, parts in direct thermal contact are made from the same material whenever possible. The only exception in our design was the 4-K radiation shield where the simulation showed a huge difference in the cooldown performance if copper is replaced by aluminum.

All the parts with nominal temperature of 4 K (except for the 4-K radiation shield and the copper braids used for flexible thermal links) are gold plated with nickel as under-plate. Gold prevents surface oxidation and gives high thermal conductance, so it is a preferred material for low temperature applications where low emissivity is needed to reduce the thermal radiation load on sensitive parts [72]. The nickel under-plate acts as a barrier layer to prevent copper migration to the gold layer.

Parts with a nominal temperature of 60 K (except the flexible thermal link) are made from aluminum and are nickel plated. Although emissivity of nickel is not as low as gold and the thermal conductivity is not as high as that of gold, nickel is a good alternative for less sensitive parts for its low-cost and high wear-resistance. Aluminum is the chosen material for the 60-K parts because the thermal modeling showed that aluminum is a better choice than copper for 60-K parts in terms of cooldown performance (see section 2.3).

Aluminized Mylar: To further reduce the radiative heat load on sensitive parts, all the 4-K parts and 60-K parts are wrapped with several layers of aluminized Mylar. A thin high-reflective material, such as aluminized Mylar, is a practical choice for low temperature applications when one needs to provide radiative insulation for sensitive parts. Figure 2.7 shows some of these parts, which are wrapped with thin layers of aluminized

Mylar.

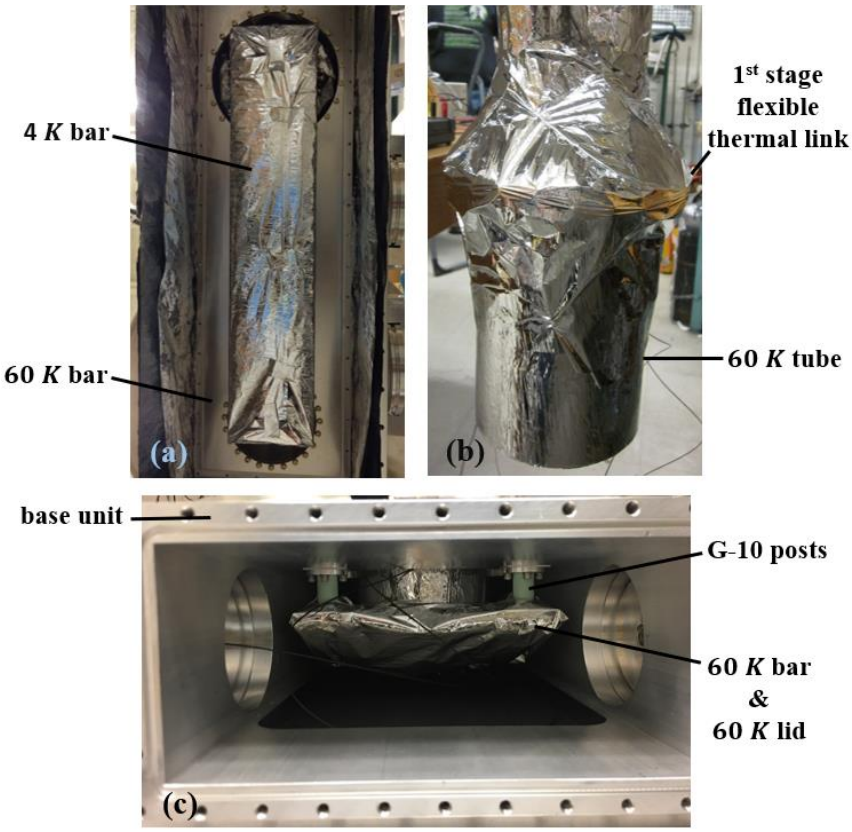

Figure 2.7: Parts with lower temperatures are wrapped with several layers of aluminized Mylar to provide radiative insulation against parts with higher temperatures: (a) 4-K bar, (b) 1st stage flexible thermal link and 60-K tube and (c) 60-K bar and 60-K lid. To support the 60-K bar, five G-10 posts are bolted to the base unit and the 60-K bar.

Assembled Cryostat: Figure 2.8 shows the fabricated and assembled cryostat bolted to an optical table. The cryostat is compact and can be moved easily. The cryostat has a total mass of about 300 lb. One can see that the base unit provides support for the whole cryostat structure and is the housing for all the hermetic feedthroughs.

A pressure relief vent and an analog pressure gauge (with standard 0.5-inch pipe thread) are hermetically installed on one of the modified ISO flanges (with a 0.5-inch pipe

threaded hole in the center) to monitor pressure and to make sure that the system is not over-pressurized. Two commercially available DB-25 hermetic feedthroughs are used for the wiring. Each of them is made of hermetically sealed 25-pin connector installed on an ISO-63 KF flange.

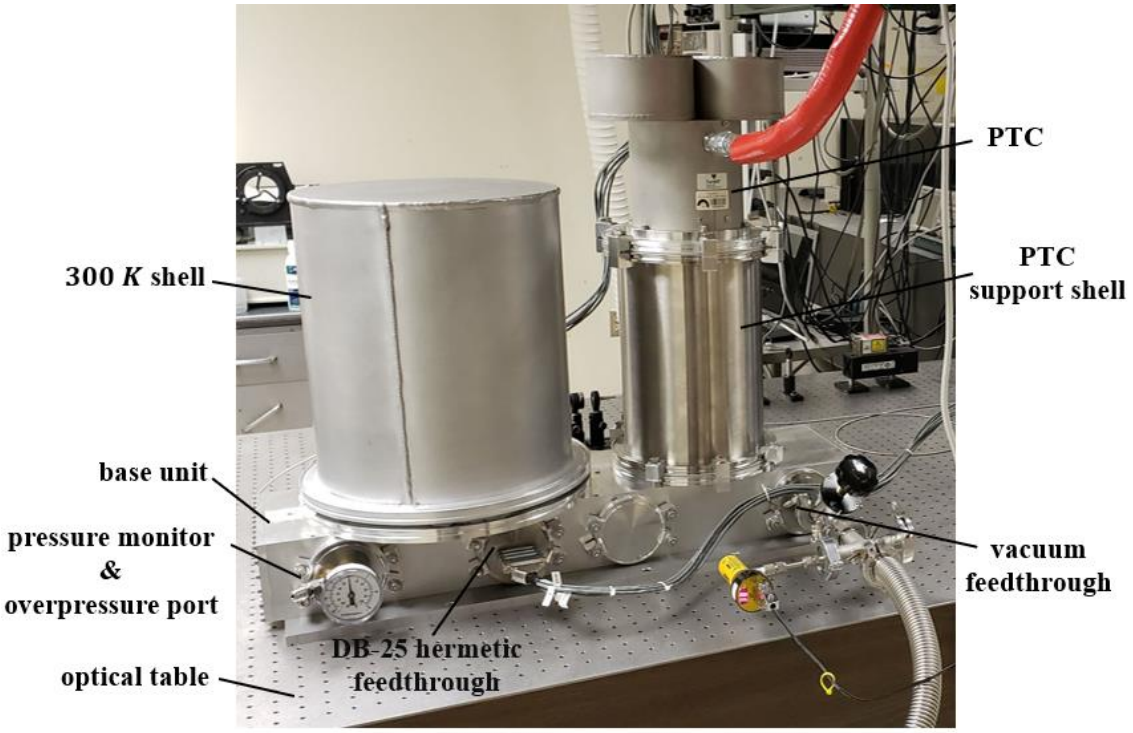

Figure 2.8: Fabricated and assembled cryostat mounted on an optical table. O-ring sealed ISO-63 KF flanges are used as standard installation mountings for hermetic feedthroughs.

2.3 Thermal Modeling with COMSOL

For the design optimization, thermal modeling of the instrument was performed before the construction begun. The goal was to reach the lowest possible temperature on the 4-K base plate and to cool down as fast as possible. The simulation was carried out

using COMSOL Multiphysics® software, which uses the finite element method. The overall geometry of the designed cryostat, its thermal boundary conditions, a selection of possible materials for each part, the heat capacity and the thermal conductivity as a function of temperature for each material serve as input for the program. COMSOL then solves the time-dependent heat diffusion equation. Since the inner parts of the cryostat are under vacuum during the cooldown, the convective heat transfer can be ignored.

We will discuss the elements of the thermal model that we used to design and optimize major components of our cryostat with the help of the software package COMSOL.

2.3.1 Modeling Geometry

The same geometry model as the 3D cryostat model (from the Creo Elements/Pro software) was generated in COMSOL with only two exceptions: 1. The 1st stage and 2nd stage of PTC are represented only by their two stages. Since the temperature-dependent cooling powers of the two stages of the PTC are given by the manufacturer, considering only the two stages of the PTC is not going to change the simulation results. 2. The outer shell is not drawn in the geometry model but its impact on the modeling is considered by defining the boundary conditions for other parts. Since the outer shell has a nominal temperature of about 300 K and its temperature does not change significantly, this would be a good estimation. For instance, the surface ends of the G-10 posts, which are bolted to the base unit in 3D design, have a constant temperature of 300 K in the thermal model.

2.3.2 Equation for Heat

Let us consider a body of mass density ρ and specific heat capacity C_P (at constant pressure) in thermal contact with a stage, subjected to a source of heat Q ([W/m^3]). The heat equation governing conductive and radiative heat transfer can then be expressed in terms of temperature T [73]:

$$\rho C_P(T)\frac{\partial T}{\partial t} + (\nabla . q(T)) = Q(T) \tag{2.3}$$

where $q(T)$ is the total heat flux ([W/m^2]). The total heat flux can be written in terms of conductive heat flux $q_c(T)$ and radiative heat flux $q_r(T)$:

$$q(T) = q_c(T) + q_r(T) \tag{2.4}$$

According to the Fourier's law of heat conduction, which states that the conductive heat flux is proportional to the temperature gradient, $q_c(T)$ can be expressed as:

$$q_c(T) = -k\nabla T \tag{2.5}$$

where k is the thermal conductivity ([W/m.K]).

The inward radiative heat flux for a surface can be written in terms of the surface-to-ambient and surface-to-surface radiative heat fluxes [74]:

$$q_r(T) = \varepsilon\sigma(T_{amb}^4 - T^4) + \varepsilon(G - \sigma T^4) \tag{2.6}$$

where T_{amb} is the ambient temperature and G is the irradiation which is the total arriving radiative flux (excluding the one coming from the surrounding environment). The first and second terms on the right of Eq. (2.6) represent the surface-to-ambient and surface-to-surface radiative heat fluxes, respectively. A derivation of Eq. (2.6) is given in appendix C.

For a surface such as the outer surface of the 60-K radiation shield that sees the

cylindrical shell at nominal temperature of 300 K, the surface-to-ambient term is considered where the T_{amb} is 300 K. For a surface such as the outer surface of the 4-K radiation shield, that sees the inner surface of the 60-K radiation shield, the surface-to-surface term is applied.

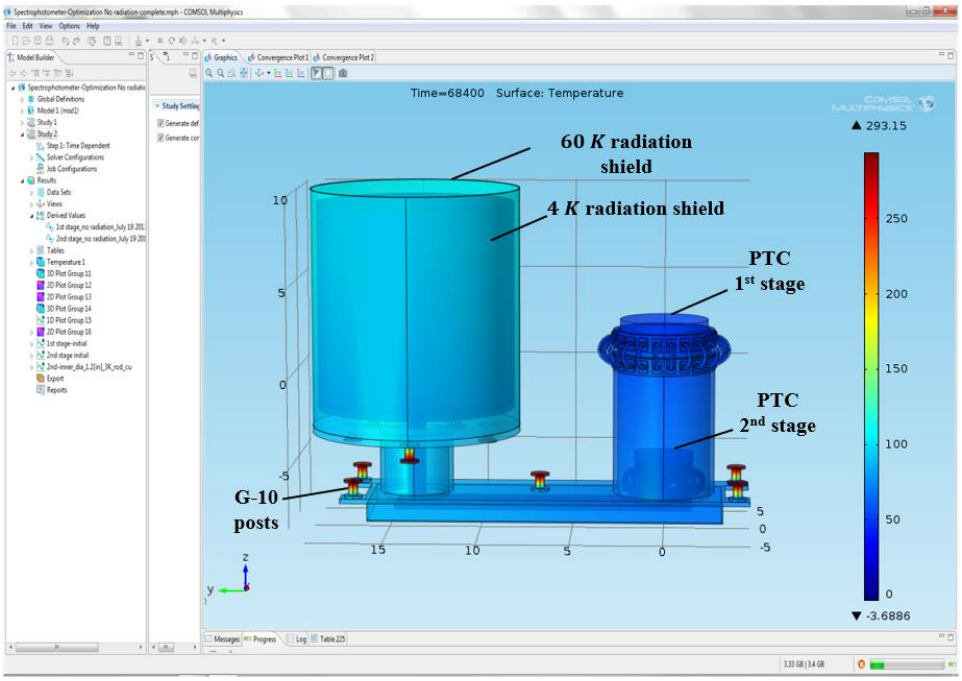

Figure 2.9: The thermal modeling of the cryostat via COMSOL Multiphysics® software. The heat diffusion equation with boundary conditions for various geometries is solved to optimize design details and materials for each part with the goal to reach the lowest possible temperature at the base plate and to cool down as fast as possible. A temperature of 300 K is considered as initial condition for all components. Temperature-dependent cooling powers for the 1st and 2nd stages of PTC are applied according to the technical data sheet and the temperature of the 4-K base plate and 60-K stage are monitored over time.

The temperature-dependent cooling powers of the two stages of the refrigerator were introduced into the heat transfer equation as Q in Eq. (2.3). Since we are cooling the system, Q is negative. Figure 2.9 shows an example of the thermal modeling of the

instrument. There is heat flow from the 4-K and 60-K radiation shields (higher temperature, left side) toward the 1st stage and 2nd stage of our refrigerator (lower temperature, right side) in the cryostat. The relatively large temperature difference between the top and bottom of the G-10 posts reveals the extremely good thermal insulation the G-10 material can provide.

2.3.3 Design Optimization

To optimize the design, one needs to find the best material, length, and cross-sectional areas for each component of the cryostat. The best material for a component that needs to conduct heat quickly relative to its thermal bulk, is a material with large thermal diffusivity. Thermal diffusivity D is the thermal conductivity divided by density and specific heat capacity at constant pressure ($D=k/\rho C_P$). Figure 2.10 shows the thermal diffusivity of some technical materials which are commonly used in low-temperature applications.

Among common materials used for low-temperature applications, copper and aluminum are practical choices since they have high thermal diffusivity and are easy to machine and cost-efficient. Figure 2.11 shows the temperature-dependent thermal conductivity from room temperature to 4 K of copper of different purities and different alloys of aluminum. Copper with residual resistivity ratios (RRR) of 100 and aluminum 1100 are materials which are commercially available and have high thermal conductivity. Hence, they were initially considered in our simulation for components that required high thermal diffusivity. However, in several cases the optimization was constrained by the

aluminum alloy availability in the required size and therefore other alloys of aluminum (2024, 6063, etc.) were considered as well.

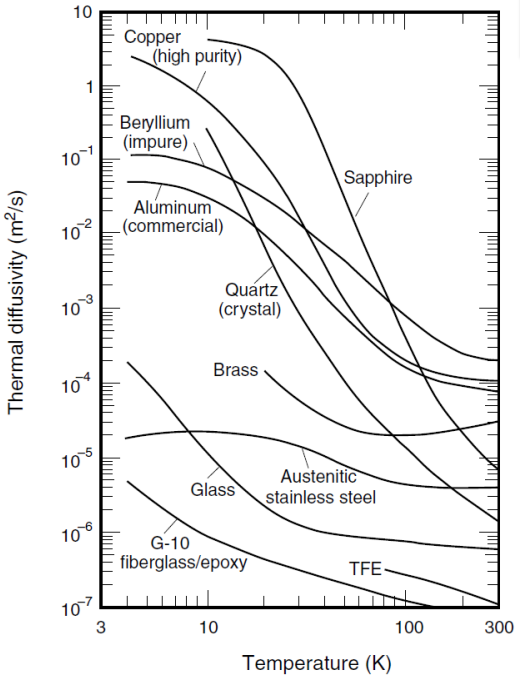

Figure 2.10: Thermal diffusivity for selected materials used commonly in low-temperature applications. Figure taken from [50].

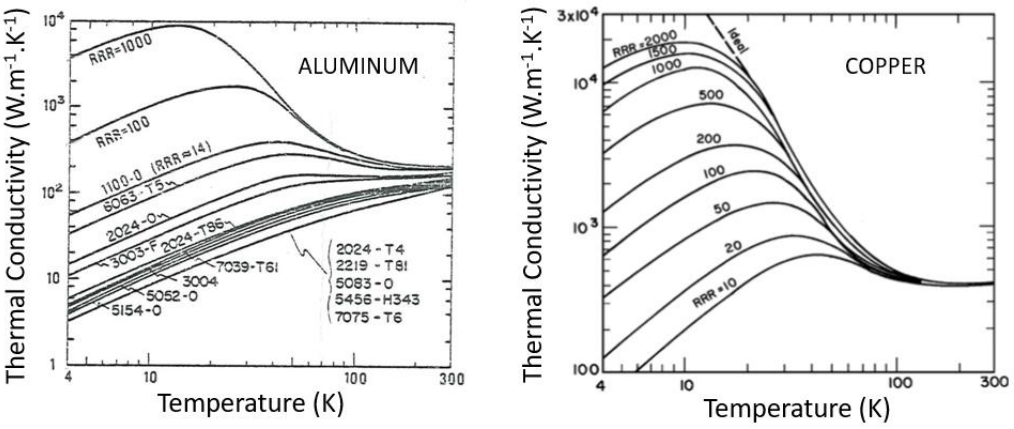

Figure 2.11: Temperature-dependent thermal conductivity of different alloys of aluminum (left) and different purities of copper (right). Figures taken from refs. [75], [76]. RRR – residual resistivity ratio – is the ratio of resistivities at ~300 K and ~4 K.

A few examples of the design optimization, performed in COMSOL, will be discussed in the rest of this section where temperatures of the 4-K base plate and 60-K stage are examined for different scenarios. Figure 2.12 shows the thickness optimization and material selection for the 4-K bar performed in COMSOL Multiphysics® software. In this case, a large thickness (cross-section) means higher thermal conductance, which is desired, but also an undesired higher heat capacity. The thickness optimized for fastest cooldown is thus expected to be a compromise. To find an acceptable solution the temperature of the 4-K base plate was calculated as a function of time during cooldown for different thicknesses of Al 1100 and Cu 100. The best results was obtained with Cu 100 and a thickness of 0.25 in.

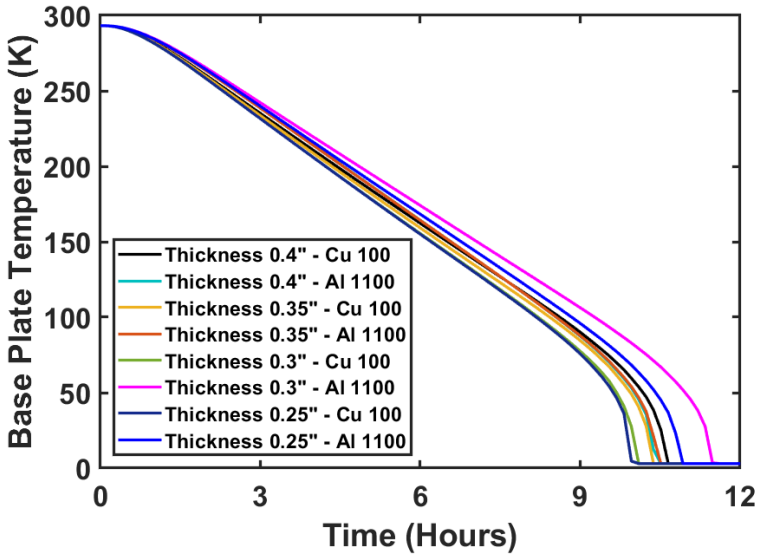

Figure 2.12: Thickness optimization and material selection for 4-K bar. The thermal modeling was performed in COMSOL and the temperature of the 4-K base plate was monitored.

Figure 2.13 shows the thermal modeling via COMSOL software for different

surface emissivity. We assumed that all parts of the cryostat have the same emissivity. The simulation results show that the surface emissivity should be kept below 0.1 in order for the base plate to reach 4 K and to have a reasonable cooldown time. As discussed before, this criterion was addressed by gold- and nickel-plating the sensitive parts of the cryostat. In addition, aluminized Mylar with very high reflectivity was wrapped around.

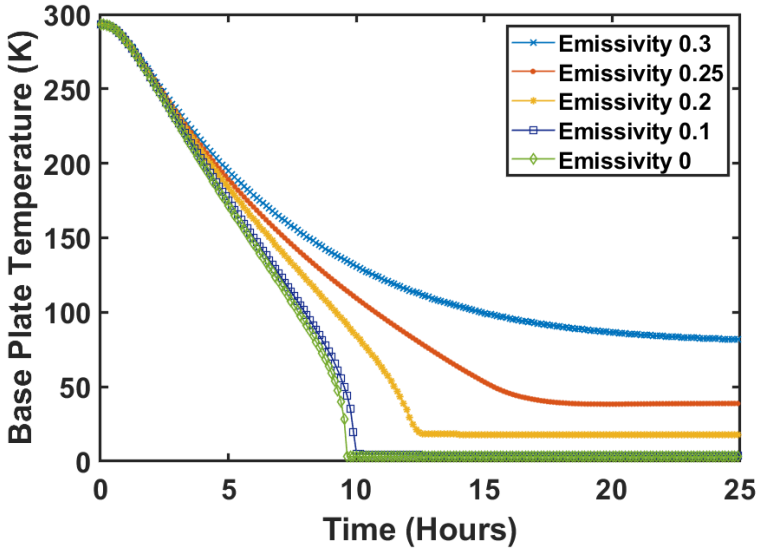

Figure 2.13: Effect of thermal radiation on cooldown for different surface emissivity of the cryostat parts is investigated by thermal modeling via COMSOL software.

2.4 Monitoring Temperature at Different Stages

For monitoring the temperature of the 60-K stage, the PTC 1st stage and the PTC 2nd stage, silicon diode temperature sensors (model DT-670 from Lake Shore Cryotronics) are used. These thermometers offer reasonable accuracy from 500 K to 1.4 K, which covers our temperature range of interest. Their working principle is based on the temperature

dependence of the forward voltage drop across a silicon diode junction at a constant current [77]. Figure 2.14 shows the forward voltage and the sensitivity for the DT-600 series diode thermometers at a constant excitation current of 10 μA.

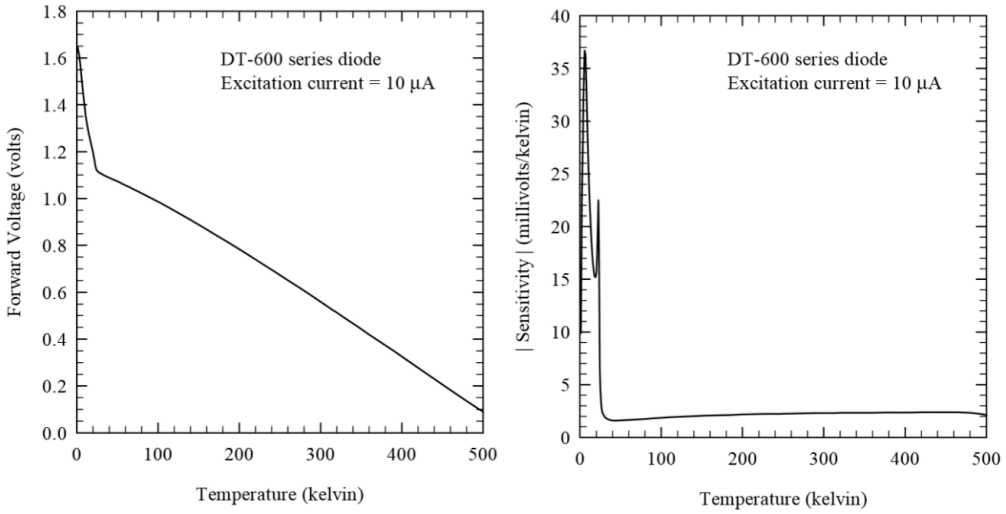

Figure 2.14: Forward voltage and sensitivity versus temperature for the model DT-600 series diode thermometer at constant excitation current of 10 μA. Figure taken from [78].

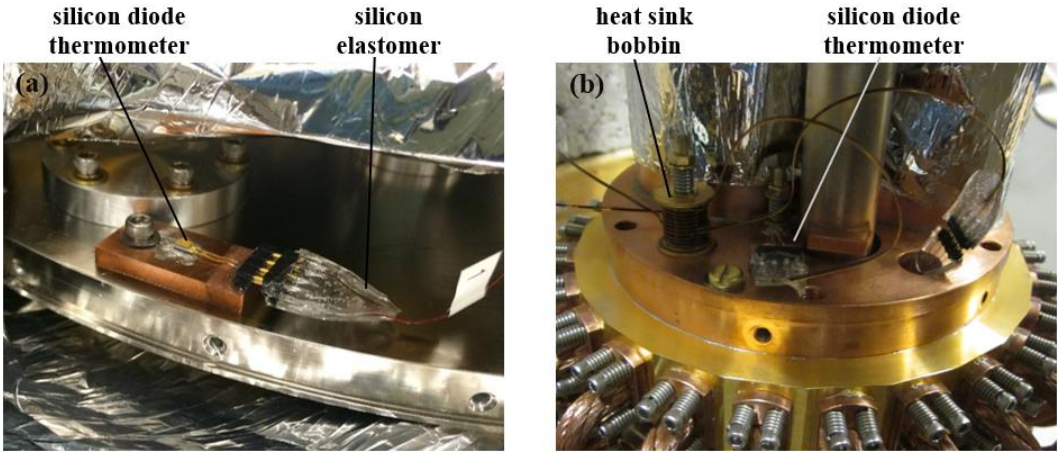

Figure 2.15: A silicon diode thermometer soldered to a small copper plate mounted on (a) the 60-K stage and (b) the PTC 1st stage. The small bobbin mounted on the PTC 1st stage provides the required thermal anchoring for the wiring.

Figure 2.15 shows a silicon diode thermometer soldered to a small copper plate mounted on the 60-K stage and the PTC 1st stage. To have a very high thermal conductivity between the thermometer and the small copper plate, pure indium solder is used. An ultra-low outgassing silicone elastomer (SCV 2590 from NuSil™) is used to protect the wires and to provide mechanical stress-relief.

To monitor and control the temperature at different stages inside the measurement chamber, e.g. at the 4-K base plate, Cernox® cryogenic temperature sensors (model CX-1050 from Lake Shore Cryotronics) are employed. These resistance temperature detectors (RTDs) with negative temperature coefficient have a higher sensitivity compared to the diode thermometers.

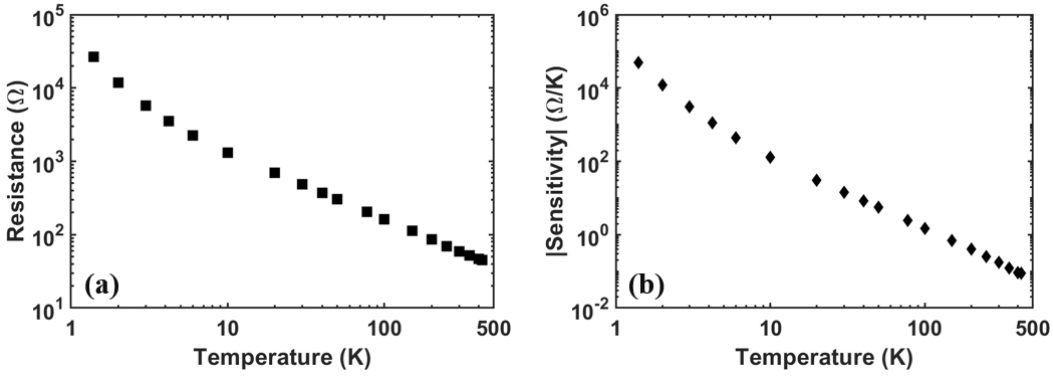

Figure 2.16: Typical (a) resistance and (b) sensitivity vs temperature of a CX-1050 Cernox® RTD. Data taken from [77].

Figure 2.16 shows the typical resistance and sensitivity of CX-1050 RTDs. These detectors are designed to withstand repeated thermal cycling and to have minimum sensor self-heating [77]. Each Cernox® temperature sensor was indium soldered to a small circuit

board and was surrounded by a nickel-plated copper housing to minimize the thermal noise caused by blackbody radiation. The Cernox® assembly could be screwed down to any stage.

A cryogenic temperature controller (model 350-3062 from Lake Shore Cryotronics) is used to read the outputs of the diode and the RTD temperature sensors with LABVIEW software. The temperature resolution of the measurement is determined by the sensitivity of these temperature sensors and the resolution of the temperature controller. Table 2.1 shows the typical sensor performance for each of the employed sensors with the LakeShore 350 readout.

Table 2.1: Typical CX-1050 and DT-670 temperature sensor performances. Data taken from [77].

LakeShore sensors			LakeShore 350 temperature controller		
Sensor model	Nominal resistance/voltage	Typical sensitivity	Input range	Resolution	Resolution: temperature equivalents
CX-1050 (10 mV)	3507.2 Ω	-1120.8 Ω/K	0 Ω to 10 kΩ	100 mΩ	89 μK
DT-670	1.58 V	-31.6 mV/K	0 V to 2.5 V	10 μV	320 μK

Phosphor-bronze wires are used for the electric connections between components at 300 K and at 4 K. The low thermal conductivity (and higher electrical resistivity) of these cryogenic wires minimizes unwanted heat conduction. For cryogenic thermometry, a four-lead type measurement is used to eliminate the (relatively large) resistance of the cryogenic wire. A four-lead configuration formed into a ribbon cable (Quad-Lead™ from Lake Shore Cryotronics) with Polyimide insulation is used, which makes heat sinking

much easier compared to individual wires.

To remove heat flow down the sensor leads, we used heat sink bobbins at 4 K and 60 K for the wires in the inner chamber and the intermediate stage, respectively. Figure 2.15(b) shows a small gold-plated copper bobbin bolted to the PTC 1st stage. The small bobbin is used for thermal anchoring of the ribbon cable before connecting to the thermometer leads. A quad-lead wire is wrapped several turns tightly around the bobbin and is secured in place and protected by Stycast 1266™ epoxy. The epoxy improves the thermal anchoring of the wires as well. Figure 2.17(a) shows a fabricated large feedthrough bobbin mounted on the 4-K base plate, which provides heat sinking for the wires entering the measurement chamber. Six phosphor-bronze quad-lead wires pass the center-hole of the feedthrough bobbin and are wrapped around. To have a light-tight feedthrough, the center-hole is filled with black epoxy. Four large feedthrough bobbins are employed in total (two on the 60-K stage and two on the 4-K base plate) for heat sinking the wires.

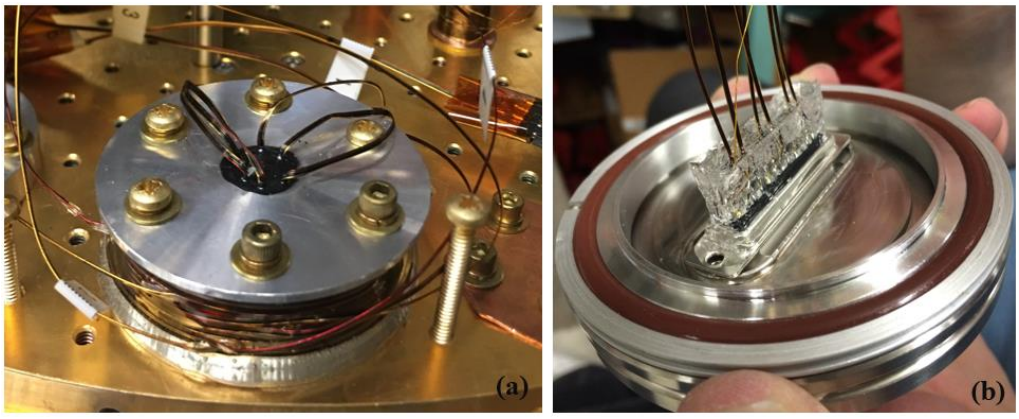

Figure 2.17: (a) Heat sink feedthrough bobbin mounted on the 4-K base plate. (b) Electrical wires soldered to a DB-25 hermetic feedthrough.

As discussed earlier in this chapter, commercially available DB-25 hermetic feedthroughs are used as vacuum feedthroughs for these wires. Figure 2.17(b) shows the six phosphor-bronze quad-lead wires soldered to a DB-25 connector. Silicone elastomer is used again to provide protection and stress-relief. The extra pin in the DB-25 connector is used for grounding.

Since rf noise can be transmitted through the wires causing undesired heating, capacitor-input filters (commercial DB-25 connectors) were implemented at the cryostat input. All instruments share a common ground.

2.5 Cooldown Preparation & Results

Figure 2.18 shows the setup for cooling the cryostat. The PTC is used in combination with a compressor (model CP-6200-H from Leybold), which requires only electricity and cooling water to operate [79]. A rotary valve operates at a frequency of 1.5 Hz generating pressure pulses in high-purity He (99.999% or higher). More details on the working principle of the PTC can be found in appendix B.

The rotary valve is controlled with a frequency converter. Since the frequency converter is connected to the remote connection of the compressor, it starts/stops automatically when the compressor starts/stops. A molecular sieve filter installed in the middle of the high pressure supply flexline ensures that oil is prevented from entering.

To minimize convective heat transfer inside the cryostat, one needs to reach a high vacuum. Cryostats operating below 77 K, have vacuums of ~10^{-5} millitorr or less since the

cold parts act as a cryopump for residual gases [80]. However, for the best performance, one needs to use mechanical pumps to reduce the pressure before cooling down the cryostat. Also, pumping the system and back-filling the vacuum space with dry nitrogen gas for several times is a good practice to eliminate the water vapor and to prevent

ice formation on the sample surface at low temperatures [50]. With a turbo pump backed by a rough pump, we reach a vacuum pressure of ~1 millitorr for our cryostat before starting the cooldown.

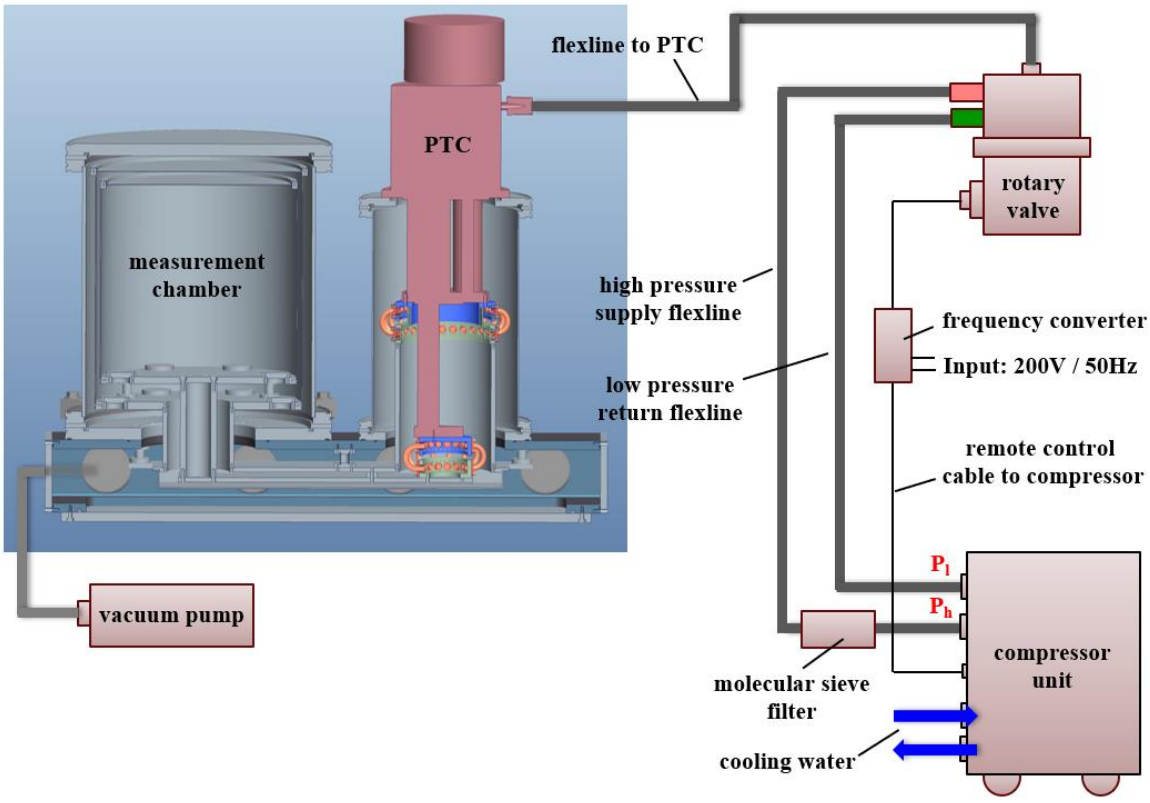

Figure 2.18: Layout of the cryostat setup for cooldown. The compressor unit in combination with the rotary valve creates the pressure pulsation in He required for cooling. The vacuum pump reduces the pressure inside the cryostat to ~1 millitorr before the cooldown starts.

2.5.1 Control of Vibration-Induced Noise

In a cryostat where a mechanical refrigerator such as a pulse tube cooler (PTC) provides the required cooling, mechanical vibrations can be transmitted into the cryostat where they dissipate into undesired heat adding to the temperature noise.

To reduce the vibration transmission to the sensitive parts of the cryostat, several approaches have been taken. First, flexible copper braids are used to mechanically decouple the PTC 1^{st} stage (PTC 2^{nd} stage) from the rest of the parts with a nominal temperature of 60 K (4 K) while providing a strong enough thermal path, see Fig. 2.3. Second, the high/low pressure flexlines and the molecular sieve filter are suspended from the ceiling structure by the elastic bands. Hence, most of the vibrations will be absorbed before propagating to the cryostat. Third, Additional mechanical isolation of the cryostat from the environment was achieved by floating the optical table. Fourth, the compressor is placed in the next room to reduce the acoustic effect and the high/low pressure flexlines are passed through two holes in the wall to reach the rotary valve.

More details on the noise characteristics of the custom-cryostat and various vibration-induced noises that could limit the performance of the apparatus will be discussed in chapter 5.

2.5.2 Cooldown

Figure 2.19 compares experimental cooldown data to the simulation performed in COMSOL Multiphysics® software. According to the experimental data, the temperature

of the base plate reaches 4 K after about 12 hours. The base plate reaches the lowest temperature of 3.9 K after about 14 hours. Also, a lowest temperature of ~55 K is measured for the 60-K stage. We see that there is a good agreement between the experimental data and the simulation results. In the simulation, a surface emissivity of 0.1 is considered for all the parts at 4 K and 60 K. As discussed before, the emissivity of sensitive parts is decreased significantly by gold (and nickel) plating and using aluminized Mylar as super-insulation against thermal radiation. Hence, considering an emissivity of 0.1 in our thermal modeling of the cryostat is realistic.

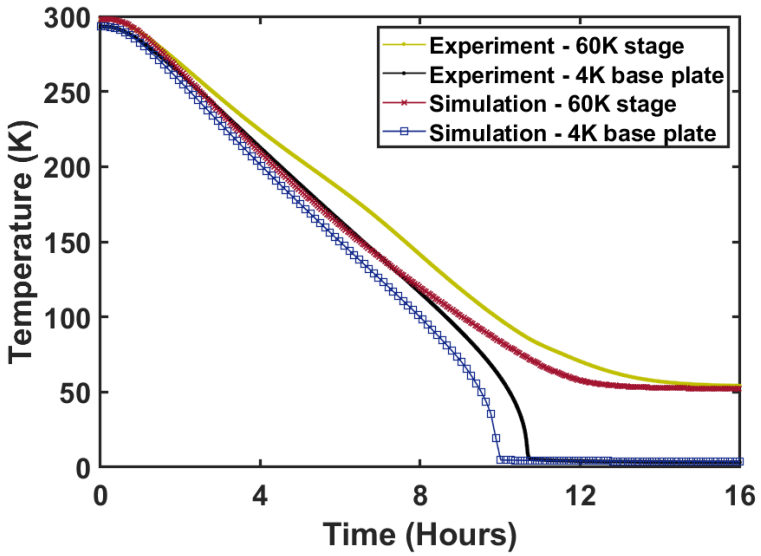

Figure 2.19: Comparison of experimental cooldown and simulation data. According to experimental data, the temperature of the base plate reaches 4 K after about 12 hours.

2.6 Summary

In summary, a cryogen-free cryostat has been designed, built and tested. The

experimental stage (base plate) can be accessed from the top. The operating temperature of 4 K at the base plate is reached in 12 hours (overnight). This cryostat possesses entry ports for electric and optical cables and fibers needed to perform optical absorption spectroscopy. To reduce the effect of mechanical vibration of the environment to the sensitive parts of the cryostat, the optical table is floated and elastic bands are deployed to suspend the flexlines and molecular sieve filter from the ceiling structure.

Chapter 3

Setup for Optical Calorimetric Absorption Measurements at 4 K

In this chapter we will describe the optical setup to produce tunable excitation from 330 nm to 1700 nm that can be fiber coupled into the cryostat. We will also discuss the layout of the absorption measurement instrumentation on the 4-K base plate and the high-resolution thermometry.

3.1 Optical Instrumentation & Setup

For a sensitive calorimetric absorption measurement, one needs to couple the light beam efficiently from excitation sources at room temperature to the measurement chamber

at 4 K (where the specimen resides). The goal is to couple as much excitation power to the sample because this ultimately controls the sensitivity of the absorption measurement using the (lower-power) tunable light source.

In this section the different excitation sources that can be used in our measurement, the special optical fiber used to deliver light from room temperature to 4 K, and the free space optical setup for coupling light from the excitation sources to the special optical fiber will be discussed in detail.

3.1.1 Excitation Sources

Various lasers emitting at selected wavelengths or a tunable light source can be used to probe the sample absorption.

Tunable light source - To perform an absorption measurement with spectral resolution one needs to have a tunable excitation source with high brightness across a broad wavelength range. To cover a broad spectral range from ultraviolet through visible into the near-infrared, a laser-driven white-light source (EQ-99 from Energetiq Technology Inc) in combination with a monochromator (Triax 180 from HORIBA Scientific) is used. Typically, multiple lamps such as Halogen/Tungsten, Xenon-arc, and Deuterium are used to cover this broad spectral range. However, combining multiple lamps is costly and high brightness is not obtained for all the desired wavelengths. EQ-99 has a (quoted) lifetime of more than 5000 hours and long term stability of a 1% decrease in output power per thousand hours. In this laser-driven light source, a high temperature xenon plasma is formed and sustained by a high power diode laser-focused in the center of a fused-silica

bulb (filled with high-pressure xenon gas) [81]. The laser power absorbed by the plasma is reradiated across the broadband spectrum and the collection optics couple the light into the monochromator. The monochromator has three gratings for selecting the desired wavelength. The 1st grating has a groove density and blaze wavelength of 600 gr/mm and 400 nm, respectively. The 2nd grating has a groove density and blaze wavelength of 600 gr/mm and 750 nm, respectively. The 3rd grating has a groove density and blaze wavelength of 300 gr/mm and 1000 nm, respectively. The gratings with 600 gr/mm groove density have an optimized bandpass of 5-10 nm while the 300 gr/mm grating has an optimized bandpass of 13-17 nm. Gratings with higher grove density ensure a good spectral resolution in the visible range. The bandpass can be controlled by adjusting the width of the exit slit of the monochromator. An electromechanical shutter is installed after the exit slit to modulate the sample excitation. The wavelength, the bandwidth, and the modulation frequency can all be controlled by a computer. The output of the monochromator is coupled into a 300-µm diameter multimode optical fiber with a numerical aperture (NA) of 0.22. Figure 3.1 shows the tunable light source including the EQ-99 laser-driven light source in combination with the Triax 180 monochromator. More details on EQ-99 light source system can be found in appendix D.

This light source is tunable from about 200 nm to 1700 nm. However, for wavelengths below 320 nm, one needs to fill the lamp house with a purge gas since ozone will otherwise form from atmospheric oxygen reducing the light output. An average illumination power of 6 µW/nm after the monochromator output fiber was measured for wavelengths between 330 nm and 1700 nm.

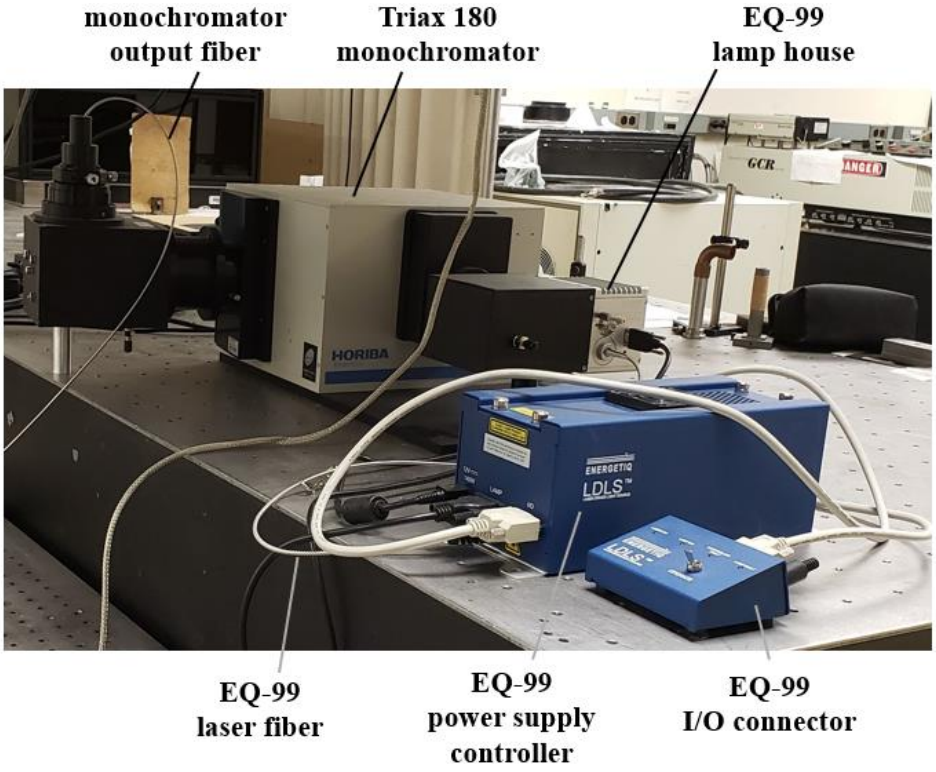

Figure 3.1: Tunable light source, including the EQ-99 laser driven light source and the Triax-180 monochromator. A fiber delivers the output from the IR laser to the EQ-99 lamp house (where the xenon plasma is formed). The I/O connector is the operator interface to the EQ-99.

Lasers at selected wavelengths – According to Eq. (1.1) the sensitivity of an absorption measurement can be improved by increasing the incident power P_0 assuming the smallest measurable absorbed power P_{min} does not change. Hence, to perform an absorption measurement with ultimate sensitivity, lasers with high incident powers at selected wavelengths can be utilized. The highest possible incident power that can be delivered to a sample residing in the measurement chamber at 4 K is determined by the amount of irradiation power that can be dissipated in the measurement chamber without raising the temperature above 5 K temperature.

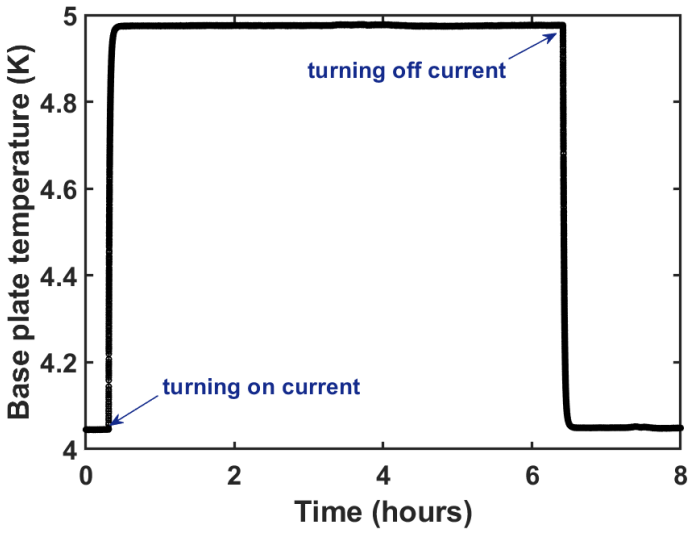

Figure 3.2: Temperature change of the 4-K base plate when 100 mW of heating power is delivered by an electrical resistor mounted on the base plate. (A current of 10 mA is applied to a 1-kΩ resistor).

As discussed in the previous chapter, temperatures below 5 K are required to operate low-Tc SQUIDs. We showed that our cryostat is able to dissipate powers up to 100 mW before the base plate reaches 5 K. Figure 3.2 shows the temperature of the base plate when 100 mW of power is dissipated from an electrical heater (resistor) mounted on the base plate. Therefore, any (laser) illumination source with a power of less than 100 mW can be utilized.

3.1.2 Coupling Light into the Cryostat (from a 300 K to a 4 K Environment)

Fiber Optics – Optical fibers are used routinely to deliver light into cryostats in

low temperature applications [82]–[85]. A 300-micron diameter step-index multimode fiber with a numerical aperture of NA=0.22 is used for this purpose in our setup. The fiber core is made from pure silica and cladding from F-doped silica. This special fiber (from OZ Optics) with vacuum feedthrough is 1-m long outside the cryostat and has a 3-mm outer diameter stainless steel jacket. Inside the cryostat the fiber is 1.5-m long with a 0.9-mm outer diameter hytrel jacket. Both ends of the fiber are terminated with standard connectors. The vacuum feedthrough part of the fiber (with standard 0.5-inch pipe thread) can be mounted hermetically on a modified O-ring sealed ISO-63 KF flange (with a 0.5-inch pipe threaded hole in the center). As discussed in chapter 2, these ISO flanges have hermetically sealed feedthroughs. The fiber passes through a fiber feedthrough connected to the 60-K stage. The fiber is then wrapped a few turns around the 4-K cylinder (in the space between the 4-K base plate and 60-K stage) for thermal anchoring before entering the measurement chamber through another fiber feedthrough. The latter is bolted to the 4 K-base plate.

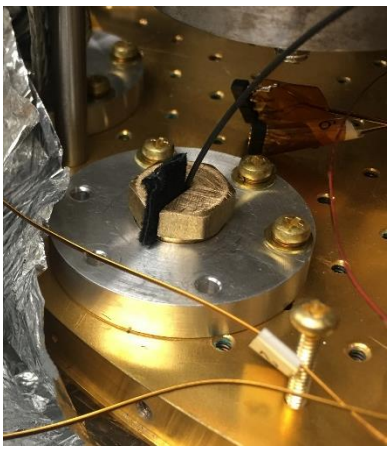

Figure 3.3: The light-tight fiber feedthrough mounted on the 4-K base plate.

Figure 3.3 shows the fiber feedthrough mounted on the 4-K base plate. This fiber feedthrough is a narrow slit in a pipe-threaded plug, which is mounted on a custom-built flange. The flange is screwed to the 4 K-base plate (or the 60-K stage). To protect the fiber from damage, it is covered with soft velvet cloth when passing through the narrow slit. To have a light-tight feedthrough, the velvet cloth is used to fill the gap in the feedthrough.

Free space optical setup at room temperature – A schematic diagram of the optical setup at room temperature is shown in Fig. 3.4. This setup is used to couple light from the excitation sources (the tunable light source or laser at selected wavelength) to the fiber which delivers the excitation to the 4-K measurement chamber in the cryostat.

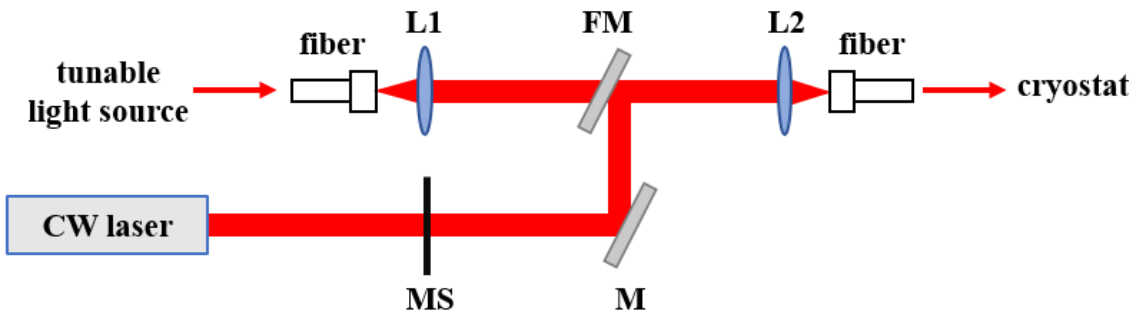

Figure 3.4: Schematic diagram of the optical setup at room temperature for coupling the light from one of the excitation sources to the fiber. L1: collimating lens f=25 mm, L2: focusing lens f=25 mm, M: mirror, FM: flip mirror, MS: electromechanical shutter.

The output of a fiber connected to the exit of the monochromator is collimated with lens L1 (f = 25 mm) and is focused on the fiber (going to cryostat) through lens L2 (f = 25 mm. As mentioned before, the beam from the tunable light source can be switched with a shutter integrated into the monochromator. The laser light can be turned on and off using

another electromechanical shutter (MS). A flip mirror (FM) is used to switch from the tunable light source to the laser. This setup allows us to easily monitor the incident beam power and adjust the optical fiber by inserting calibrated filters. Also, additional lenses can be used to increase or decrease the laser beam size if needed.

Collimator – A collimator is used to collimate the output of the fiber inside the measurement chamber. The collimator tube is made of aluminum and shown in Fig. 3.5. Light enters from the right side via a fiber optic connection (a) and passes through an f =11 mm aspheric lens (b) to form a collimated beam. The collimated beam maintains a diameter of about 3 mm inside the 4-K measurement chamber. If one needs to focus the light onto the sample, a second lens can be added at position (c). Such an objective assembly was previously tested [86].

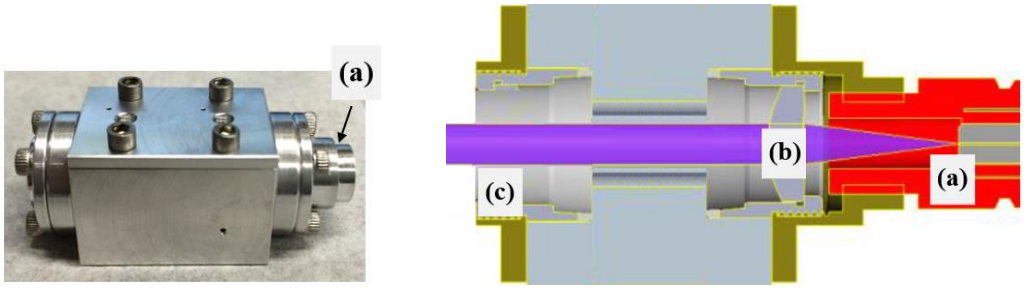

Figure 3.5: Collimator assembly. Left: fabricated collimator. Right: Optical path inside the collimator. Light enters from the right via fiber optics connection (a) and collimated beam by an aspheric lens (b). Another aspheric lens (not shown here) can be placed in location (c) to focus the beam if desired. Figure adopted from ref. [86].

The light coupling efficiency can be defined as the ratio of the beam power measured before the sample in the 4-K measurement chamber (after the collimator) to the beam power before lens L2. For a wavelength range of 330 nm to 1700 nm, a coupling

efficiency of 88% (+/- 4%) was measured. Most of the losses are due to coupling light from one fiber into another fiber.

3.2 Thermal Network inside the Measurement Chamber

For sensitive optical calorimetric absorption spectroscopy, one needs to provide a well-controlled thermal environment for the sample to permit measurements of very small temperature changes. For this reason, different optical and mechanical components were designed, fabricated and employed for the low temperature setup inside the measurement chamber. High resolution thermometers (HRTs) are employed for ultimate sensitivity. Figure 3.6(a) shows the top view of the 4-K base plate with the custom-built optical and mechanical components mounted on it when the vacuum shell and the radiation shields are removed. Figure 3.6(b) shows the 3D design of the sample holder created with Creo Elements/Pro software. The schematic diagram of the thermal network inside the measurement chamber is shown in Fig 3.6(c).

The collimated light passes through the sample (S) mounted in the sample holder, and the transmitted light through the sample is collected by a beam dump (BD). The sample holder consists of three rings: measurement ring (MR), damping ring (DR) and reference ring (RR). The sample is thermally connected to the measurement ring and an HRT mounted on the measurement ring is used to measure the temperature change of the sample. An ohmic resistor (r) is used for calibration of the absorption measurement. The outer ring (reference ring RR) of the sample holder serves as reference mass. The reference ring is in

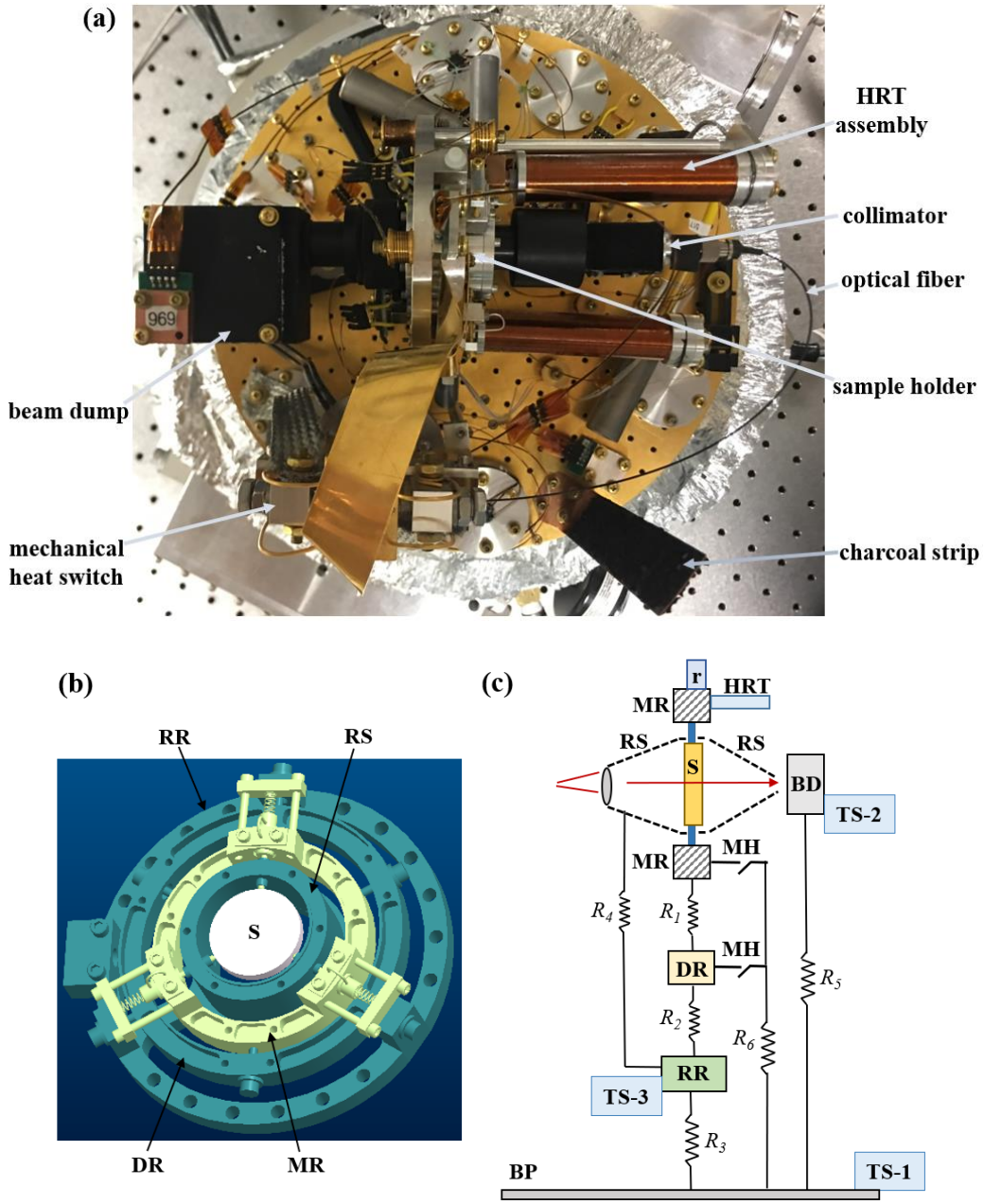

Figure 3.6: (a) Top view of the 4-K base plate with the custom-built optical and mechanical components mounted on it when the vacuum shell and the radiation shields are removed. (b) Sample (S) is thermally connected to the measurement ring (MR) with good mechanical but poor thermal connection to a reference ring (RR). A Damping ring (DR) in between provides additional thermal isolation for the sample. (c) Schematic diagram of the equivalent thermal network: BP: base plate, BD: optical beam dump, HRT: high-resolution thermometer, TS-1,2,3: temperature control units (thermometer and ohmic heater), RS: radiation shield, R_i: thermal resistances of the mechanical mounts and connectors, MH: electromechanical heat switch, r: ohmic resistor for calibration.

mechanical and thermal contact with the base plate (BP). The damping ring is integrated into the design to provide additional thermal resistance and capacitance between the measurement ring and the reference ring.

Temperature stabilization units (TS) are mounted to the base plate (TS-1), the beam dump (TS-2) and the reference ring (TS-3). They consist of electric heaters and thermometers and are implemented to produce a quiet thermal environment under load. In particular, periodic temperature changes introduced by the modulated optical pump beam (by the PTC) are suppressed using TS-2 (TS-1). The Cernox® temperature sensors are employed as thermometers for TS-1 and TS-2. For measurements that require ultimate temperature stability at the reference ring, a high resolution thermometer (HRT_TS-3) is used as the thermometer of choice for TS-3. More details on the performance of the temperature stabilization units will be given in chapter 5. Phosphor bronze wires with four-lead configuration are used for the electrical wiring from the base plate to TS-1 and TS-2 units. As mentioned in chapter 2, phosphor-bronze wires are also used for the electrical connections from the 300-K to the 4-K components. A commercial superconducting wire, e.g. 71-μm-diameter Nb-Ti with 81-μm-diameter Cu-Ni cladding, is used for wiring connections from the base plate to TS-3, HRT, and r. Three twisted pairs of superconducting wires go to the HRT (mounted on the measurement ring) and two twisted pairs to r (for 4-wire measurement). These wires are thermally anchored at the reference ring, to minimize the heat flowing to the measurement unit. Thermal anchoring is provided by wrapping the twisted pairs around gold-plated copper bobbins connected to the reference ring. Stycast 1266™ epoxy is used to improve the heat sinking and to protect the

wires. To provide better heat sinking for the five twisted pairs of wires going to TS-3, they are also thermally anchored at the 4-K base plate.

A charcoal strip, made of activated charcoal pieces fixed to a copper strip with GE varnish, is attached to the 4-K base plate to adsorb the residual gas (water vapor) from the vacuum space. Activated charcoal is typically used getter at cryogenic temperatures because it can be easily reactivated by heating and subsequent evacuation [87]. The design and working principles of different components inside the measurement chamber will be discussed in the following sections.

3.2.1 Sample Holder

For optimum performance, the sample holder must satisfy several requirements. The measurement unit including the sample, the measurement ring, and the HRT should have a small total heat capacity C and all the components should be in excellent thermal contact with each other. The measurement unit needs to be thermally isolated from the rest of the measurement setup, when performing sensitive absorption measurement. Besides, the measurement unit needs to be in high thermal conductance contact with the 4-K base plate for fast cooling only when necessary. Also, the effect of scattered light from the sample needs to be minimized so that it does not interfere with the absorption measurement.

When measurements at cryogenic temperature are not carried out in a cryogenic liquid, one is faced with the challenge of maintaining temperature uniformity of the sample and its holder. Hence, the measurement ring should be made of a material with high thermal conductivity, so the entire volume will come to thermal equilibrium quickly and provide a

uniform temperature profile along the measurement ring. For this purpose, copper is used as the material of choice for the whole sample holder assembly. The sample holder is plated by silver followed by a fine layer of rhodium to prevent copper from getting tarnished and to reduce the thermal radiation load on the sample holder by reducing its surface emissivity. Silver is well known for its low emissivity, while the rhodium flash is used to increase the durability of the coated part.

The scattered light is an inherent problem in optical calorimeters [43] since it can lead to an undesired signal in the measurement unit. To address this problem, a few measures have been taken. The inside of the 4-K radiation shield is black anodized to absorb any stray light produced in the measurement chamber. Black tubes are employed between the collimator and the sample holder, and between the beam dump and the sample holder to shield the measurement unit from scattered light. The outside surfaces of the collimator and the beam dump are sprayed black. A radiation shield (RS) with black interior for maximum absorption is inserted and thermally connected to the reference ring. The sample is thermally connected to the measurement ring via three 1.5-mm copper fingers. To reduce the impact of volume scattering on the temperature measurement, the three copper fingers are passed through small holes in the radiation shield.

Since a high thermal conductance contact between the sample and the measurement ring is desired, the copper fingers are pressed firmly against the sample with springs. The thermal resistance between the sample and the measurement ring can be estimated by calculating the thermal resistance of the copper fingers. The thermal resistance R across an object can be defined as [88]:

$$R = \frac{L}{Ak} \tag{3.1}$$

where L is the length of material, k is its thermal conductivity, and A is the cross-sectional area perpendicular to the path of heat flow. Considering the copper fingers geometry and using the above relation, a low thermal resistance of about 50 K/W is estimated between the sample and measurement ring at temperature of 4 K. For this estimation, a thermal conductivity of 320 W/(m.K) for OHFC copper material (RRR=50) at 4 K is considered.

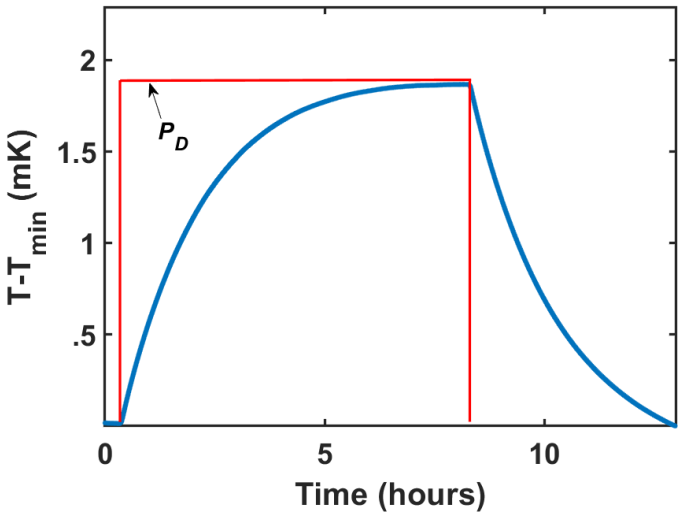

Figure 3.7: Measured temperature change (blue curve) of the measurement ring when a constant heating power of P_D = 9 nW (3 μA through a 1-kΩ resistor) is applied for several hours and then shut-off (red curve).

To isolate the measurement unit from the rest of the measurement setup, thermal coupling through R_1 and R_2 need to be kept as small as possible (R_1 and R_2 large). For this reason, the measurement ring is thermally and mechanically connected to the damping ring via three nylon screws. Similarly, the damping ring is connected to the reference ring via three nylon screws. Nylon is one of the most thermally insulating materials at low

temperature with thermal conductivity of about 0.012 W/(m.K) [50].

The thermal resistance between the measurement ring and reference ring (and beyond) can be experimentally measured by dissipating a known amount of heating power into the measurement ring and measuring its temperature change after reaching the steady state, see Eq. (1.12). From the results shown in Figure 3.7 a thermal resistance of about 1.95×10^5 K/W can be estimated from Eq. (1.12).

Since the main thermal communication from the measurement ring to the reference ring is through the nylon screws, one can also estimate the thermal resistance between the measurement ring and reference ring using Eq. (3.1). Each nylon screw has a diameter and length of 1.5 mm and 4 mm, respectively. Hence, a thermal resistance of about 1.6×10^5 K/W can be estimated from the known thermal properties of nylon [50], which is close to the measured value. A thermal resistance of 10^5 K/W is obtained from a similar measurement for the connection between the damping ring and reference ring. This means that $R_1 \approx R_2 \approx 10^5$ K/W. The large values for R_1 and R_2 ensure that during a measurement (heating) cycle, which typically lasts 10 seconds, only sample, measurement ring, and high resolution thermometer are heated, keeping the relevant heat capacity C_s to a minimum. This passive thermal RC network, cf. Fig. 3.6(c), serves as a low-pass filter effectively damping the thermal communication from the combined system of measurement ring, sample and HRT to the other components in the measurement chamber.

The thermal coupling through R_3 is a compromise of good heat conduction to the 4-K base plate and shielding from temperature fluctuations of the base plate produced by the pulse-tube cooler. An aluminum post holder, bolted down to the 4-K base plate,

securely holding an aluminum optical post attached to the reference ring provides the thermal communication between the reference ring and the base plate. Similar to the measurement of the thermal resistance connecting the measurement ring to the reference ring, a thermal resistance of about 1400 K/W was determined for R_3. Also, the heat capacity of the measurement unit is estimated to be 40 mJ/K from Eq. (1.11). For such a configuration, the low-pass filter between the reference ring and the base plate has a cut-off frequency, $f_c=1/2\pi RC$, of about 1 mHz. Since the PTC operates at 1.5 Hz, this low-pass filter effectively damps the PTC-induced temperature perturbation while providing sufficient cooling for the reference ring. The thermal link between the reference ring and base plate can be increased by attaching copper wires or copper straps to them if desired.

The thermal coupling through R_4 needs to be kept as small as possible so that the scattered or reflected light (if any) absorbed by the radiation shield, is dissipated efficiently to the reference ring and 4-K base plate. Since the radiation shield is firmly attached to the reference ring, a thermal resistance of a few K/W is estimated for R_4.

3.2.2 Beam Dump

As discussed before, the beam dump is responsible for trapping the light transmitted through the sample. The beam dump should satisfy three criteria in order to have the best performance. First, the thermal communication through R_5 needs to be strong (R_5 small) so that the heat is quickly dissipated to the 4-K base plate. This is especially crucial when more than a few mW of excitation need to be dissipated. The beam dump, made of aluminum, is secured firmly to 4-K base plate using an aluminum post and holder. A thick

copper strap is used to improve the thermal coupling between the beam dump and the base plate. A thermal resistance of $R_5 \approx 50$ K/W is measured experimentally.

The second criterion for the beam dump is to have a very small back scattering coefficient. This ensures that the incident light on the beam dump is trapped efficiently inside and the backscattered light does not disturb the measurement. Figure 3.8 shows the custom-built beam dump when the top lid is removed. The round shape inside the beam dump ensures that the incoming light hits the first surface at an angle and bounces many times inside before it escapes. The inner surfaces of the beam dump are black (Krylon 1602 Ultra-flat black spray paint) and have an emissivity close to one. A test was conducted at room temperature to compare the brightness of the backscattered light of the custom-built beam dump to the commercially available beam traps (BT600 model from Thorlabs and PL15 model from Newport). The amount of backscattered light was about 10 times lower for our design.

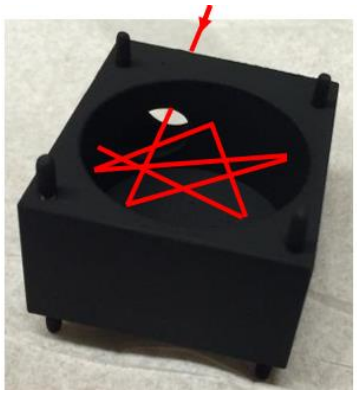

Figure 3.8: Custom-built beam dump used in the 4-K measurement chamber. A sketch of possible beam path inside the beam dump is shown with red lines.

The third criterion is the ability to work at a temperature of 4 K without

performance deterioration. To test the performance of the beam dump at low temperature, the custom-built beam dump and the two commercially available beam traps were placed into liquid nitrogen (77 K) for a few minutes before the backscattered light level was measured. While the two commercially available beam traps showed increase backscatter after having been exposed to 77 K our custom-built beam dump did not.

3.2.3 Mechanical Heat Switch

As discussed previously, the measurement ring and the damping ring are very well thermally isolated from the 4-K base plate. This means that a long cooldown time can be expected for these rings. To shorten the cooldown time for these components when needed a mechanical switch was implemented. Heat switches are widely used at low temperature applications for coupling and decoupling the sensitive parts from the rest of the measurement setup [89]–[92]. In our measurement setup, an electromechanical heat switch (MH) between measurement ring/damping ring and the 4-K base plate is used, see Fig. 3.9.

In this solenoid driven heat switch the magnetic field, generated by applying current to solenoid, moves the actuator away from or toward the solenoid tube depending on the direction of the current. Two gold-plated copper straps, bolted to the measurement ring and the damping ring, are aligned right in the middle of two gold-plated copper jaws (without making any contact to them). The copper jaws are thermally connected to the 4-K base plate via two copper braids. Each copper strap is about ~12 cm long and has a thickness and width of about 0.05 cm and 2 cm, respectively. The gold-coated copper is widely used when one needs to have high joint conductance. When the actuator moves away from the

solenoid tube, the copper jaws will be pressed against the copper strap. In this state the electromechanical heat switch is closed and a high conductance contact through R_6 is formed. Similarly, when the direction of the current changes and the actuator moves toward the solenoid tube, the heat switch will be opened and the measurement ring/damping ring will be isolated again. Since the thermal conductance across a pressed contact increases approximately linearly with pressure [50], the magnetic field needs to be sufficient for having a high thermal conductance.

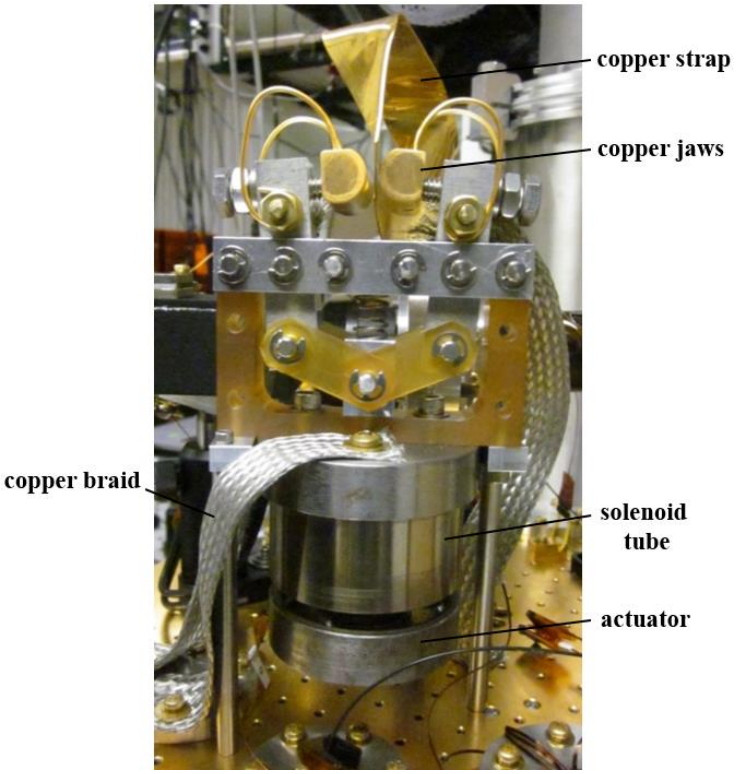

Figure 3.9: An electromechanical heat switch employed for fast cooling of the measurement ring/damping ring.

A thermal resistance of $R_6 \approx 90$ K/W between the measurement ring/damping ring

and the 4-K base plate (when the heat switch is closed) was determined by measuring the steady-state temperature increase when a known amount of heating power is applied.

3.3 High Resolution Thermometry

From the first development of high resolution thermometer (HRT) nearly 40 years ago [59], HRTs have been playing an important role in the advancement of low temperature science [60], [61], [99], [63], [64], [93]–[98]. The HRT takes advantage of a superconducting quantum interference device (SQUID) to measure the change in magnetization of a paramagnet in a constant magnetic field. SQUIDs are among the most sensitive detectors of magnetic fields. They are for example able to sense magnetic signals generated by the human brain.

Basic principles of a conventional HRT will be discussed fist in this section. We will then describe how a paramagnetic sensor for applications at 4 K was fabricated. At the end, the design principles and assembly of the HRT employed in our instrument will be discussed.

3.3.1 Basic Principles of a Conventional HRT

A schematic diagram of a conventional HRT is shown in Fig. 3.10. A paramagnetic material, fabricated as a cylindrical pill, is placed inside a superconducting flux tube and is thermally connected to the sample of interest. The flux tube is usually made of niobium, which has the highest superconducting transition temperature, T_c=9.25 K, among metals

and is a practical choice for many superconducting applications [100]. A solenoid is placed outside the flux tube and provides a uniform magnetic field *H*. While the solenoid is turned on, the flux tube is cooled down to temperatures below its superconducting transition temperature. Then the solenoid is turned off and the magnetic field *H* is trapped within the flux tube interior. So, the paramagnet is surrounded by a persistent magnetic field *H* while it is shielded by the flux tube from the ambient magnetic fields.

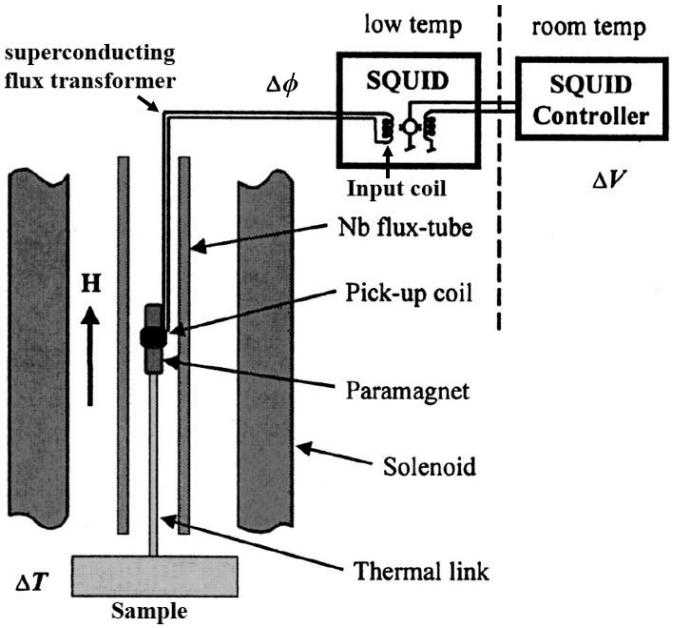

Figure 3.10: Components of a conventional HRT. Figure adapted from [94].

The paramagnet is used as a temperature sensor taking advantage of the fact that small changes in temperature induce relatively large changes in magnetic flux within the paramagnet material. This is because its magnetic susceptibility, χ, is strongly temperature dependent. A flux transformer couples the magnetic signal to the SQUID. A flux

transformer is a closed superconducting circuit which consists of two coils in series: the pick-up coil and the input coil. The pickup coil is tightly wrapped around the paramagnet and acts as a magnetic antenna. The input coil is magnetically coupled to a dc-SQUID and is typically part of the SQUID package.

Figure 3.11(a) shows how the change in magnetic flux is coupled to a dc-SQUID. A simple one-turn wire loop is considered for the pick-up coil and the input coil is just for illustrating the idea of flux coupling. As a temperature change ΔT occurs within the paramagnetic sensor, a flux change $\Delta\phi$ is induced in the pick-up coil. Based on the laws of superconductivity, the magnetic flux inside a superconducting loop cannot change as long as the loop remains superconducting. This comes from the fact that the superconducting loops can contain magnetic flux only in multiples of a universal constant known as the magnetic flux quantum ϕ_0 [2×10^{-15} Wb]. Hence a change in the magnetic field within the paramagnet causes a flux change $\Delta\phi$ in the input coil as well, but with different direction so that the net flux in the superconducting flux transformer is effectively canceled out. The SQUID and associated electronics then output a voltage, ΔV, at room temperature proportional to the $\Delta\phi$ which in turn is proportional to ΔT. After calibration, $\Delta V(\Delta T)$, the temperature change can be determined from the voltage. A detailed discussion of the design and operation of the SQUIDs can be found in [65], and it is beyond the scope of this dissertation and only the key concepts of a dc-SQUID will be reviewed here.

A schematic representation of a dc SQUID is shown in Fig 3.11(b). A dc-SQUID is a superconducting loop consisting of two Josephson junctions, labeled J_1 and J_2 in Fig 3.11(b), which are connected in parallel. The Josephson junctions are a physical system

composed of two superconducting regions with a weak coupling (such as a thin layer of an insulator or weakly conducting layers) in between. In a Josephson junction, the electrical current can flow between the two superconducting regions with zero resistance.

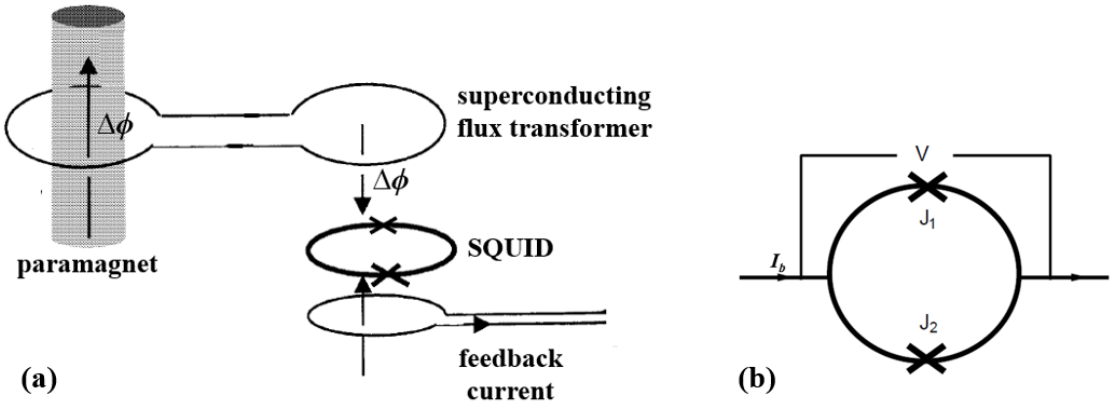

Figure 3.11: (a) Idea of superconducting flux transformer and the feedback current. Figure adapted from ref. [93]. (b) Schematic representation of a dc SQUID, figure from ref. [62].

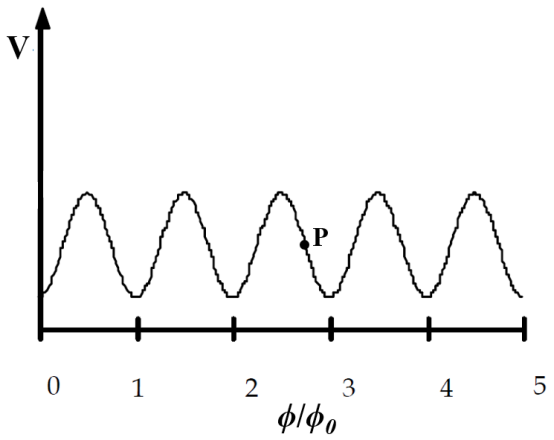

Figure 3.12: The SQUID voltage versus applied magnetic flux.

To make the SQUID function as a magnetic flux to voltage transducer a constant

bias current I_b, slightly greater than the critical current of the SQUID, is applied to it. The critical current I_c of the SQUID is the maximum current that can flow through the SQUID before a voltage develops across it. The current I_c is determined by the critical current of both Josephson junctions and the magnetic flux ϕ applied to the SQUID. Once the SQUID is biased with a constant current, the voltage across the SQUID would be periodic with the magnitude of the applied magnetic flux with a period of one flux quantum, as shown in Fig 3.12. This periodic relationship for V-ϕ curve originates from the flux quantization property of superconducting rings discussed earlier.

One can see that for every flux quantum applied to the SQUID, the voltage undergoes one complete cycle. So, one can do a sensitive measurement of magnetic flux change by counting the number of complete cycles. However, practical SQUID systems are operated in what is called a "flux-locked loop" where a feedback current is used to cancel out any changes in the external magnetic field. In a flux-locked loop scheme, the voltage across the SQUID is amplified and the resultant signal is used to drive a coil magnetically coupled to the SQUID, such as the one depicted in Fig. 3.11(a). When an unknown $\Delta\phi$ is applied to the SQUID, a feedback current flows through this coil in such a way that the generated magnetic flux has the same magnitude as the one applied to the SQUID but with opposite polarity. Under this condition, the magnetic flux change in the SQUID would be zero and the SQUID can be locked at one point on the V-ϕ curve. Point **P** in Fig. 3.12 would be suitable because $\partial V/\partial\phi$ is maximum and $V(\phi)$ is nearly linear. By measuring the feedback current going through the coil one can simply determine the unknown $\Delta\phi$. With such a control electronics for SQUID, it is possible to detect a $\Delta\phi$ with

a magnitude much smaller than one flux quantum. In addition, by linearizing the response of the SQUID to the applied flux the dynamic range of the measurement is hugely improved. The sensitivity of a SQUID device is limited by the intrinsic flux noise of the SQUID device [62].

The dc-SQUID used in our high resolution thermometry, is model SQ180 from STAR Cryoelectronics with a flux noise level of 3 $\mu\varphi_0/\sqrt{Hz}$ [101]. This means that magnetic signals larger than this noise level can be detected with this SQUID magnetometer. All the SQUID electronics and accessories were acquired from STAR Cryoelectronics. A pc-based SQUID control module (model PCI1000) with programmable feedback loops (model PFL-100) is used to operate the dc-SQUIDs in flux-lock operation. The closed-loop feedback and readout electronics (at room temperature) can be controlled by a computer via a standard RS-232. A cryocable (model CBL-C2) is used for the electrical connection between the SQUID electronics at room temperature and 4 K. The PFL-100 is connected to the warm-end connector of the cryocable that is hermetically mounted on the ISO-63 flange which is then mounted on the base unit. The cold-end of the cryocable is mated with a niobium shielded SQUID circuit board (model LL6118) at 4 K temperature. The SQUID circuit board is then connected to a SQUID package (model LS2076). The SQUID package includes the dc-SQUID with screw terminal inputs and a heater resistor to de-flux the SQUID if needed. The cryocable is thermally anchored at 60 K and 4 K when passing through custom-built feedthroughs screwed down to the 60-K stage and 4-K base plate, respectively.

3.3.2 Paramagnetic Temperature Sensor

Paramagnet Material Selection - The paramagnet material needs to have a high temperature dependence of magnetization near the temperature of interest. To ensure this, the ordering temperature (Curie temperature T_C) of the paramagnet should be slightly below the temperatures being measured [64]. In this temperature range, the magnetic susceptibility χ is large according to the Curie-Weiss Law, $\chi \propto 1/(T\text{-}T_C)$ [102]. The sensitivity, in units of flux quanta per μK, of a PdMn paramagnet (0.90 atomic percent Mn in Pd) near its Curie temperature T_C = 2.75 K, is shown in Fig. 3.13 for different trapped fields H [64]. One can see the large temperature dependence of magnetization of such a paramagnet slightly above and below its Curie temperature.

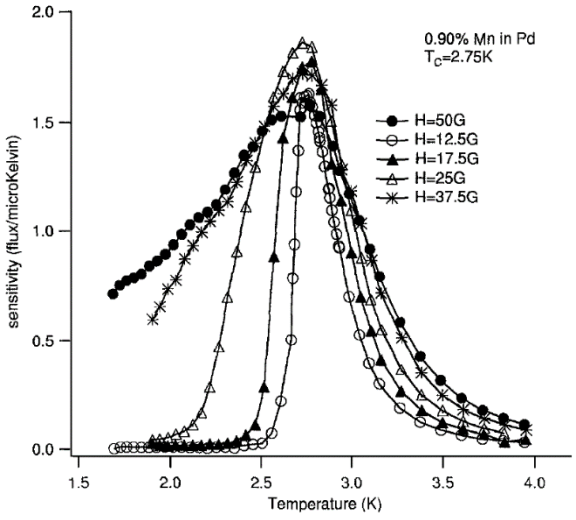

Figure 3.13: Magnetic flux sensitivity vs temperature, in units of flux quanta per μK, of a PdMn paramagnet (0.90 atomic percent Mn in Pd) near its Curie temperature, T_C = 2.75 K, for different trapped fields between 10 to 50 G [64].

A paramagnet commonly used as a thermometric element is PdMn dilute alloy [63], [64], [96], which has a very sharp transition near the Curie temperature. By controlling the Mn concentration in the Pd matrix, the transition temperature can be tuned between 1 and a few Kelvin [64], [103], which makes them an ideal choice for high resolution thermometry for a wide temperature range. In our optical calorimeter, both HRTs will be operated at a temperature near 4 K, which is the minimum temperature achieved by the 4-K base plate. Hence, the paramagnet material needs to have a Curie temperature of slightly below 4 K to have the highest temperature dependence of magnetization. Figure 3.14 shows the measured Curie temperature as a function of atomic percent Mn in Pd obtained by other studies [64], [103].

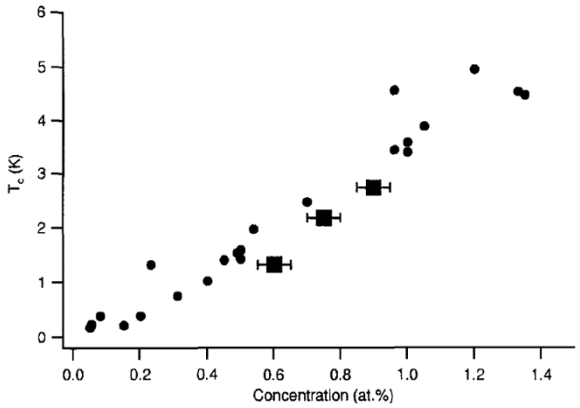

Figure 3.14: Measured Curie temperature as a function of atomic percent Mn in Pd. Data are from reference [63] (■ marker) and reference [102] (● marker).

According to Fig. 3.14, a Pd:Mn alloy with near 1.0 atomic percent Mn would have a Curie temperature of ~3.7 K and would be a good choice for our 4-K measurement chamber.

PdMn Geometry - The optimal dimension of the paramagnet is a compromise of maximizing the magnetization signal coupled to the SQUID and having a small heat capacity for the paramagnet. The change in magnetic flux $\Delta\phi$ coupled to the SQUID can be written in terms of the change in susceptibility $\Delta\chi$, within the paramagnet pill [59]:

$$\Delta\phi = NAHx\Delta\chi, \tag{3.2}$$

where N is the number of turns in the pickup coil, A is the area of the pick-up coil or the cross-sectional area of the paramagnet pill, H is the trapped field within the flux tube, and x is a coupling constant. The number of turns of the pickup coil is determined so that it approximately matches the impedance of the input coil, which is part of the SQUID package. According to Eq. (3.2), $\Delta\phi$ increases linearly with A. So, by increasing the cross-sectional area of the paramagnetic sensor one can increase $\Delta\phi$ coupled to the SQUID. However, by increasing the volume of the paramagnet its heat capacity C_{PM} is increasing too. The temperature change ΔT within the paramagnet is inversely proportional to its heat capacity, $\Delta T \propto 1/\ C_{PM}$. So, increasing C_{PM} will result in less $\Delta\phi$ induced within the paramagnet. To maximize the magnetization coupled to the SQUID, one needs to find optimal dimensions for the paramagnetic material. Our estimations showed that a PdMn pill with a diameter of 3 mm and a length of 5 mm will give us the maximum magnetization signal.

PdMn pill Synthesis – To produce a PdMn dilute alloy as the temperature sensor several steps have been followed. First, pure palladium and manganese powder were thoroughly mixed in a correct ratio to have 1.0 atomic percent of Mn in the Pd matrix. Second, the mixture is melted within an induction furnace to obtain a uniform alloy. The

melting was performed under high purity (99.99%) argon gas, where the oxygen and nitrogen impurities were reduced to below 10 parts per billion using a heated argon purifier. The vacuum induction furnace is developed at UNM and is explained in detail somewhere else [104]. The PdMn alloy was pressed into a cube shape and then it was machined into cylinders of 5-mm length and 3-mm diameter. The machining was done with electrical-discharge machining (non-magnetic tools) to prevent magnetic contamination. The cylinders were then cleaned in aqua regia and ultrasonically rinsed in distilled water and alcohol. Finally, the alloys were annealed under vacuum at 1000°C for 24 hours to remove structural defects and to be homogenized. The prolonged homogenization improves the sensitivity of the PdMn pill by narrowing the transition near the Curie temperature [105].

3.3.3 HRT Assembly

The design of the two HRTs used in our cryostat follows the principles discussed above for commercial HRTs with a few changes. A conventional HRT is typically divided into two parts – (i) the paramagnetic sensor mounted on to the stage to be measured and (ii) the larger shielded SQUID assembly mounted to another stage with the two stages having slightly different temperatures. The two parts are linked by a pair of twisted superconducting wires (forming the superconducting flux transformer, cf. Fig. 3.10) surrounded by a superconducting shielding. The Nb capillary is typically used as the superconducting shielding. In our instrument, this split design would not be ideal. The thermal conductivity of superconductors below their superconducting transition temperatures T_c is proportional to T/T_c [106]. Hence, near the 4-K operating temperature

of our instrument, Nb has T/T_c~0.43, so it still has significant thermal conductivity. In a split design, the thermal contact created by the Nb capillary between the measurement ring and the 4-K base plate would strongly degrade the thermal isolation of the measurement unit and will disturb the measurement. To address this problem the SQUID package is separated from its electronics circuit board and is integrated with the paramagnetic sensor in an "unsplit" HRT design, shown in Fig. 3.15. While the paramagnetic thermometer with integrated SQUID can be mounted on the measurement ring or the reference ring, the wiring connection from the SQUID package to its niobium shielded electronics circuit board, mounted on the 4 K base plate, can be easily done using unshielded twisted pairs of superconducting wires. With such a setup, the undesired thermal path to the measurement unit would be along the superconducting wires not the Nb capillary. In the next section, thermal communication to the measurement unit through undesired thermal paths will be discussed in detail.

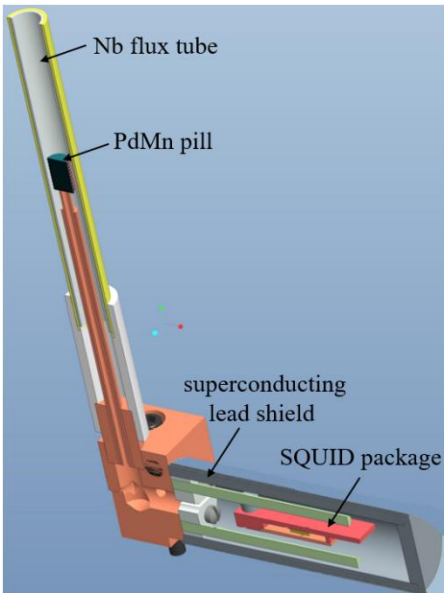

Figure 3.15: Section view of the paramagnetic thermometer with integrated SQUID.

Figure 3.16 shows the HRT at various stages of its assembly. In step 1, a miniature copper tube (0.063-in outer diameter, 0.035-in inner diameter) is slid into another slightly larger copper tube (0.094-in outer diameter, 0.066-in inner diameter) and is fixed in place with lead- and tin-based soft-solder (60%Sn-40%Pb). The outer surface of the larger copper tube is coated with the same solder. Since the 60%Sn-40%Pb solder has a superconducting transition temperature of T_c = 7.8 K [72], the SnPb coated Cu tubes act as superconducting tubes. In addition, $T/T_c \sim 0.5$ near the 4-K operating temperature, so we would still have considerable thermal conduction between the two coated Cu tubes which is desirable for heat sinking purposes. The PdMn pill is then indium-soldered to one end of the small Cu tube which has a small side cut in it. The cut is the side entrance for the pickup coil leads.

In step 2, the SnPb coated Cu tubes are inserted into a Cu centering post and secured in place by indium soldering. The Cu centering post sits on a counterbore hole in the middle of a Cu foot and is secured similarly. The centering Cu post assures that the coated Cu tubes, and so the PdMn pill, are standing straight. The Cu foot provides support for the whole HRT assembly and can be screwed down to any stage. The pure indium solder is a good choice for very high-thermal conductivity joints. The thermal conductance of a Cu/In/Cu solder joint for one square centimeter of contact area is about 30 W/K at 4 K temperature [50]. The thermal resistance between the PdMn pill and the Cu foot is estimated to be about 26 K/W.

In step 3, a superconducting wire (71-μm-diameter Nb-Ti with CuNi clad) is tightly wrapped around the PdMn pill 18 turns. This coil forms the pickup coil and as mentioned

before is wound to roughly match the input coil impedance of the SQUID (~200 nH).

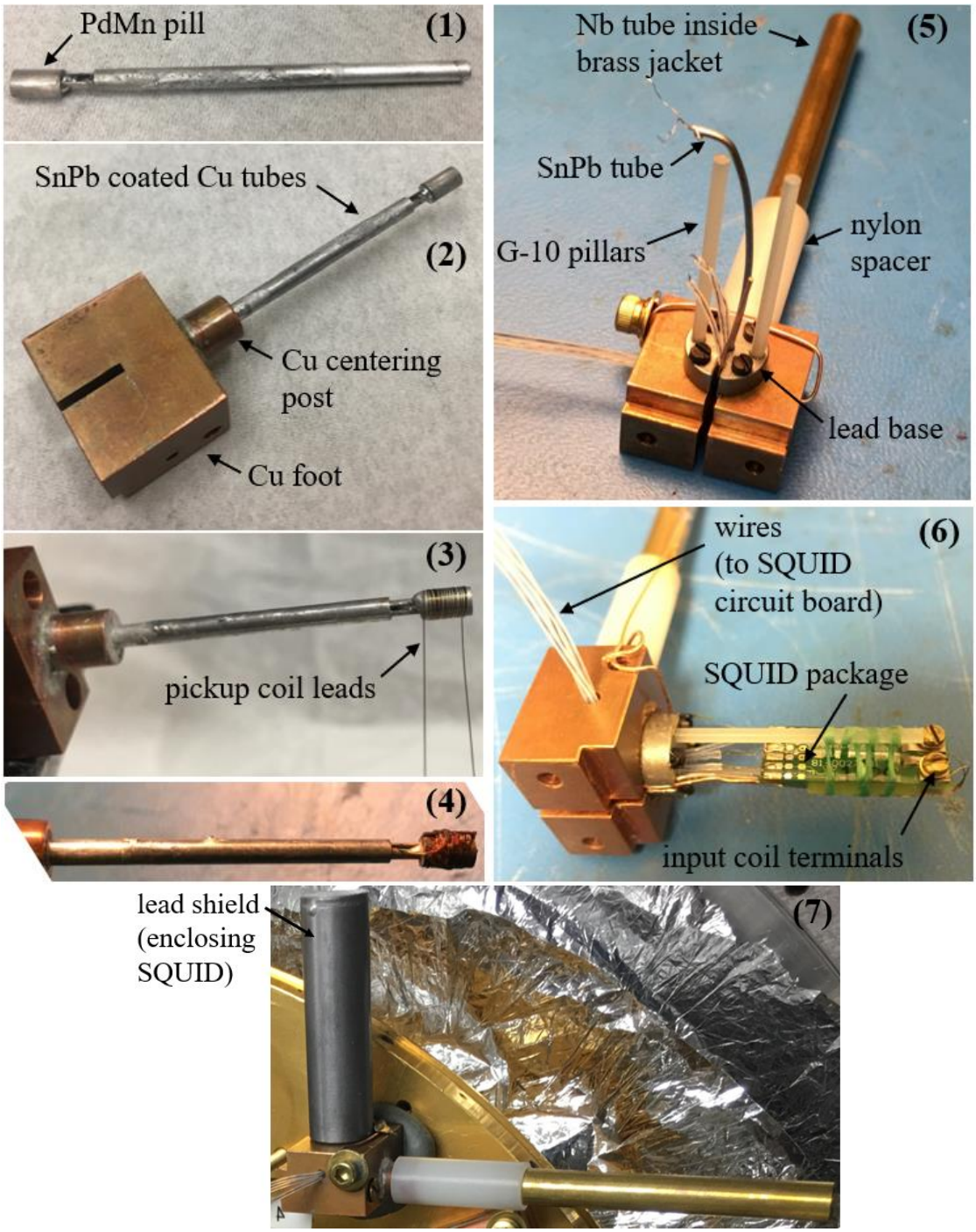

Figure 3.16: Step by step assembly of the HRT used for calorimetric absorption spectroscopy at 4 K.

In step 4, GE varnish is used to secure the pickup coil in place. A miniature SnPb tube (60%Sn-40%Pb, 0.03 in outer diameter) is then fed into the small Cu tube from the opposite end of the PdMn pill. The superconducting leads are twisted tightly together and are threaded through the tiny side cut (of the small Cu tube) into the SnPb tube. The SnPb tube is filled with thermal grease (Apiezon N™ grease) to reduce microphonics in the HRT signal. Grease is a practical choice for securing parts together temporarily. Once the parts are cold, the grease freezes and when they are warm, the parts can be taken apart easily. The SnPb tube is, in fact, a commercially available rosin flux-core solder where the rosin is emptied by blowing compressed nitrogen gas into the flux-core solder immersed into the boiling water. The SnPb tube and the SnPb coated Cu tubes act as superconducting conduits and protect the pickup leads from changing magnetic flux from the environment. For further stray field protection, a cylindrical mu-metal shield is used to enclose the 300-K shell at room temperature. The flux tube providing the superconducting shielding for PdMn pill is a Nb tube with 99.9 % purity.

In step 5, a 10-cm long Nb tube is slid into a brass jacket (10-cm long) which is then pushed tightly into a nylon spacer. The nylon spacer sits firmly on the Cu centering foot. The nylon spacer is used to guide the niobium flux tube in place and to make sure the PdMn pill is sitting right in the middle of the Nb tube so that the pill experience a uniform field when the magnetic field is trapped. A copper wire (screwed down to the Cu foot and indium soldered to the brass jacket) provides the thermal contact between the brass jacket and the Cu foot. Apiezon N™ grease is used to improve the thermal contact between the Nb tube and the brass jacket. The twisted pair of the pickup coil (which is inside the PnSb

tube) is guided to another side of the Cu foot (through a slit on the Cu foot) where it passes through a slit in a lead base, screwed down to the Cu foot. Two G-10 pillars are inserted into two holes on two sides of the lead base and provide support for the SQUID package.

In step 6, the SQUID package is secured to G-10 pillars using a floss thread and the pickup coil leads are connected to screw terminals of the input coil. Three twisted pairs of superconducting wires are used for wiring connection from the SQUID electronics circuit board, mounted on the 4-K base plate, to the SQUID package on the measurement ring or the reference ring. For damage protection, these twisted pairs are sheathed in nylon tubing. As mentioned before, all the wires going to the SQUID package on the measurement ring are thermally anchored on the reference ring. Since the reference ring is a quieter stage compare to the 4-K base plate, the thermal anchoring will help the thermal isolation of the measurement ring.

In the last step of the HRT assembly, the SQUID package is enclosed with a lead cap which is fixed firmly to the lead base using Apiezon N™ thermal grease. Lead is superconducting at 4 K temperature and so the lead cap would be like a superconducting shield for the SQUID against the stray fields. This design provides a robust and good thermal anchoring between the PdMn element and the Cu foot, which can be mounted to any stage. Also, all the sensitive components of the HRT are protected against the stray field with superconducting shielding.

Figure 3.17 shows the HRT mounted on the measurement ring. A cylindrical magnetizing coil, acting like a solenoid, is placed outside the flux tube and provides the uniform magnetic field *H*, to be trapped inside the Nb flux tube. The magnetic field

magnitude can be increased up to 100 Gauss by changing the applied current to the coil. The upper limit for *H* is set by the amount of current that the wiring can handle. The cylindrical coil is supported and thermally anchored by an aluminum post screwed down to the reference ring. The magnetizing coil is well aligned so that the flux tube is centered inside the cylinder.

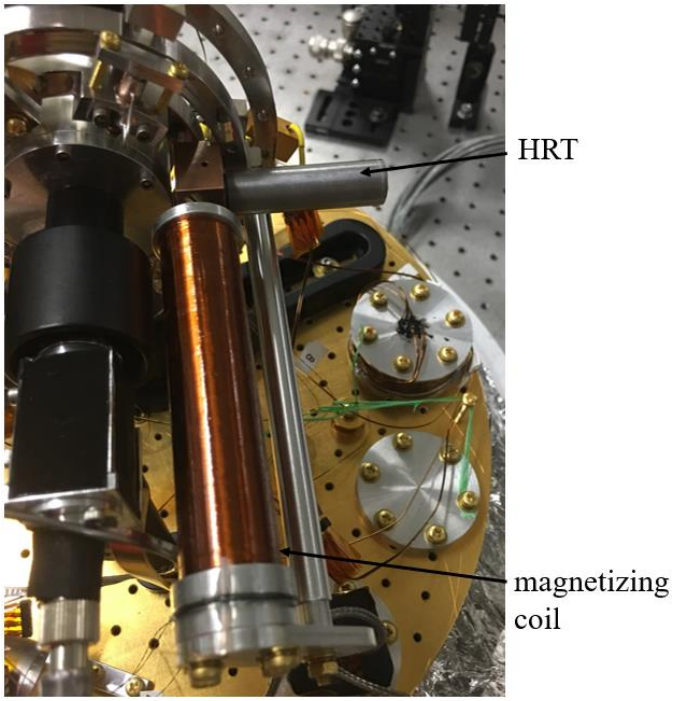

Figure 3.17: The HRT mounted on the measurement ring. The magnetizing coil provides the uniform external magnetic field *H*.

3.4 Unwanted Thermal Communication to the Measurement Unit

The sensitivity of a calorimetric absorption measurement is affected by undesired

thermal communication to the measurement unit. In our absorption setup at 4 K, there are three possible thermal links: thermal radiation from the 4-K radiation shield (4-K base plate), thermal conduction from the 4-K base plate through the optical and electrical cables, and scattered light from the sample. To assess the effect of the latter on the absorption signal (measured temperature increase), we estimated the ratio of the scattered light (from the sample) absorbed by the copper fingers to the total incident optical power. For the other two pathways, thermal resistance is estimated for each of them and compared to the measured thermal resistance between the measurement ring (as part of the measurement unit) and the reference ring through the nylon screws. The heat transfer through nylon screws is the "desired" heat path from the 4-K base plate to the measurement ring. The nylon screws give us some control over the amount of thermal isolation for our measurement unit. In this section, the effect of these pathways on the absorption measurement will be examined in detail.

Inside the 4-K measurement chamber, the thermal radiation coupling from the 4-K radiation shield to the measurement ring can potentially be significant for three reasons:

1. There is a few milli-Kelvin difference in temperature between the measurement ring and the 4-K base plate (and the 4-K radiation shield).
2. The surface area of the 4-K radiation shield enclosing the measurement ring is large.
3. The inner surface of the 4-K radiation shield is black anodized, to absorb the stray light inside the 4-K shield. Consequently it has a surface emissivity of close to one (a perfect black body).

3.4.1 Thermal Radiation from the 4-K Radiation Shield

The net radiative heat exchange between two surfaces can be stated as [50]:

$$P_{rs} = \sigma F \mathrm{A}\left({T_2}^4 - {T_1}^4\right) \tag{3.3}$$

where T_1 and T_2 refer to the temperatures of two surfaces and σ is the Stefan–Boltzmann constant [5.67×10^{-8} W/(m^{2}K^4)]. A is an area factor depending on the geometry. F is a factor between 0 and 1 depending on the emissivity of the two surfaces. For simplicity, we assume the 4-K radiation shield and the measurement ring are like two concentric spheres where the 4-K radiation shield encloses the other one and has a surface emissivity of one. Since the 4-K base plate is gold plated and has an emissivity of much less than one, our estimation can serve as a worst-case scenario. For such a case, the values of A and F would be the area of the inner surface, A_1, and emissivity of the inner surface, ε_1, respectively [107]. So, the equation for the net heat exchange between the measurement ring and the 4-K radiation shield can be written as:

$$P_{rs} = \sigma \varepsilon_1 \mathrm{A}_1\left({T_2}^4 - {T_1}^4\right) \tag{3.4}$$

or:

$$P_{rs} = \sigma \varepsilon_1 \mathrm{A}_1 (T_2 - T_1)(T_2 + T_1)\left({T_2}^2 + {T_1}^2\right) \tag{3.5}$$

Since $\Delta T = T_2 - T_1$ and $\Delta T \ll T_2, T_1$ we can simplify the Eq. (3.5) to:

$$P_{rs} = 4\sigma \varepsilon_1 \mathrm{A}_1 {T_1}^3 \Delta T \tag{3.6}$$

Defining $R_{rs} = 1/(4\sigma\varepsilon_1 \mathrm{A}_1 {T_1}^3)$ we can rewrite Eq. (3.6) as:

$$P_{rs} = \frac{\Delta T}{R_{rs}} \tag{3.7}$$

By looking at the similarity of the above equation and Eq. (1.12) one can realize that R_{rs} represents the thermal resistance between the measurement ring and the 4-K radiation shield for the radiative heat transfer. Since the measurement ring is plated with silver followed by a rhodium flash, a surface emissivity of $\varepsilon_1 \approx 0.03$ would be a good estimation [72]. The measurement ring has a surface area of $A_1 \approx 5\times10^{-3}$ m^2. So, $R_{rs} \sim 3\times10^8$ K/W. The estimated value for thermal resistance between the measurement ring and the 4-K radiation shield for radiative heat transfer is about 3 orders of magnitude larger than the measured thermal resistance between the measurement ring and the reference ring (1.95×10^5 K/W) through a nylon screw. Therefore, the thermal communication to the measurement ring through thermal radiation is a negligible pathway compared to the thermal path through the nylon screws.

3.4.2 Thermal Conduction through Wiring

A superconducting, 71-μm-diameter Nb-Ti wire with a 81-μm-diameter Cu-Ni cladding, is used for connections to the HRT and the electrical resistor mounted on the measurement ring. The wire is embedded in an insulating sleeve of 100-μm-diameter. To examine the effect of thermal conduction through the wire connections to the measurement ring, one can estimate the thermal resistance of the superconducting wire using Eq. (3.1). The approximate thermal conductivity values at 4 K for NbTi and CuNi are 0.43 W/(m.K) and 0.51 W/(m.K), respectively [108], [109]. The thermal conductivity of Stycast 1266 epoxy, considered as insulation for the superconducting wire, is 0.76 W/(m.K) at 4 K [110]. Hence, for a 10-cm long superconducting wire a thermal resistance of 2×10^7 K/W can be

estimated. Ten superconducting wires run to the measurement ring, so the total thermal resistance between the measurement ring and reference ring through the wiring is about 2×10^6 K/W. This value is about one order of magnitude larger than the measured thermal resistance between the measurement ring and the reference ring (1.95×10^5 K/W). Therefore, the nylon screws are the main pathways for the heat transfer to the measurement ring.

3.4.3 Scattered Light from the Sample

In our absorption setup, most of the scattered light from the sample is absorbed by the radiation shield enclosing the sample. A small part of the scattered light will be absorbed by the three exposed copper fingers holding the sample. Since these copper fingers are thermally connected to the measurement ring, one needs to estimate their contribution to the absorption signal. To do so, first, we can estimate how much of the scattered light reaches these three copper fingers. For simplicity, the radiation shield (RS) can be assumed to be a sphere, that blocks almost all the scattered light from the sample (placed on its center), so it has a solid angle of 4π sr. The solid angle for one copper finger with distance d_c from the sample can be estimated according to formula, $\Omega_c=(A_c)/d_c^2$, where A_c is the surface area of the copper finger viewed by the sample. Thus, the ratio $\Omega_c/4\pi$ shows how much of the scattered light from the sample reaches one copper finger. For three 1.5-mm-diameter copper fingers which are 8-mm away from the center of the sample, the ratio would be about 0.006. Since the copper fingers are plated by silver followed by a fine layer of rhodium, an emissivity of ~0.03 would be a good estimation [72]. So, the ratio

of scattered light absorbed by the silver-plated copper fingers to the total amount of scattered light from the sample would be about 10^{-4}. The samples that we are interested in are high purity optical samples where the absorption and the scattering losses are very low. For instance, for a high-quality sample with scattering loss of one part per million, the scattered light reaching the measurement unit would be already 10^{-10}. So the scattering loss would be negligible if the sample has an absorptance (ratio of absorbed power to incident power) of 10^{-8} or more.

3.5 Summary

In summary the light beam from excitation sources (a tunable light source or a laser at selected wavelength) at room temperature is efficiently coupled to the measurement chamber at 4 K where the specimen resides in. A free space optical setup allows us to easily monitor and control the incident beam power. A well-controlled thermal network inside the measurement chamber minimizes the unwanted thermal communication to the measurement unit. In addition, the effect of the scattered light from the sample is minimized so that it does not interfere with the absorption measurement. Paramagnetic sensors with Superconducting Quantum Interference Device readouts are employed, as high resolution thermometers, to measure the optical absorption induced temperature increase of the sample.

Chapter 4

Data Acquisition and Analysis

Data acquisition systems are a necessary part of any spectroscopic measurement. They represent the link between a user interface, such as a PC, and the hardware. In this chapter, the hardware configuration and the PC-based monitoring and control approach that we developed will be discussed first. We will then describe how the measurement data acquired by the HRT are processed to determine the absorptance of a sample.

4.1 Data Taking and Control

A data acquisition system, suitable for a sensitive calorimetric absorption measurement, must meet several criteria.

1. The system must be able to read out several different thermometers

simultaneously.

2. It must interface with and control the (i) excitation source (monochromator and electromechanical switch) and (ii) the temperature controllers and associated ohmic heaters.
3. The outputs of two high resolution thermometers need to be sampled without deteriorating their temperature resolution.

4.1.1 Hardware Configuration

To sample the analog outputs of the PCI1000 SQUID electronics, a USB-4431 data acquisition (DAQ) device from National Instruments is utilized. This DAQ device has four analog input channels with 24-bit resolution and a simultaneous sampling rate of 102.4 kS/s. The input range of this DAQ device is the same as the output range of the SQUID electronics, +/-10V. The 24-bit resolution of this device means that we would be able to resolve ~2 μV in the +/-10V range. The most sensitive SQUIDs have a typical voltage resolution of ~2 μV. Hence, the USB-4431 DAQ hardware is all we need for a sensitive sampling of the two high resolution thermometers. The DAQ device is then interfaced with a PC using USB.

As discussed in section 2.4, a temperature controller (LakeShore 350) reads out the temperature data from the diode and Cernox® temperature sensors. This unit is interfaced with the PC using a GPIB to USB cable.

A USB-6212-BNC DAQ unit from National Instruments (with two analog outputs) is used to drive the electric heaters of the temperature stabilization units, TS-1 and TS-2,

with 16-bit precision. For a maximum driving voltage of 5 V for each analog output, a maximum power of 25 mW can be dissipated through each heater (~1 kΩ ohmic resistor). The single analog output of the USB-4431 DAQ unit with 24-bit precision is used to drive the heater of the stabilization unit TS-3. This unit has a voltage range of ±3.5 V. So, a maximum power of ~12 mW can be dissipated through the heater of the TS-3. If more power is desired to be dissipated through each of these resistors, a Keithley 263 calibrator/source (interfaced with the PC using a GPIB cable) can be used to supply more current.

A low-noise DC precision current source (Keithley model 6220) is used for applying the desired current to the 1- kΩ electric resistor mounted on the measurement ring (labeled as r in Fig. 3.6 (c)). This heater is used to calibrate the absorption signal. This current source has a broad output current range from 100 fA to 100 mA which makes it an ideal current source for calibration and is interfaced with the PC using a GPIB cable.

For actuating the mechanical heat switch, a Matsusada RK-80H power supply is used which can be controlled by the PC. A Caswell NSP-2050 power supply is used to provide sufficient current for the cylindrical magnetizing coil of the HRT assembly to generate a magnetic field of up to 100 Gauss.

4.1.2 Software

For the real-time monitoring and control of the measurement, different LabVIEW VIs were developed and implemented:

1. VI-1 is to interface with the 4431 DAQ unit and to automatically record the

voltage readouts from the two HRTs.

2. VI-2 reads the output channels of the temperature controller (LakeShore 350).
3. VI-3 controls the excitation source – output wavelength (monochromator grating angle), bandwidth (monochromator slit), on- and off-period (electromechanical shutter) and the number of excitation cycles.
4. VI-4 opens and closes the mechanical heat switch
5. VI-5 and VI-6 control the Keithley 263 and Keithley 6220 current sources, respectively.
6. Several VIs are used to control the different temperature stabilization units. These VIs make use of LABVIEW PID (Proportional Integral Derivative) modules. The input to each PID control is the real-time temperature readout from one of the TS units (4-K base plate, beam dump, and reference ring, cf. Fig. 3.6(c)). The output is the voltage applied to the heaters (via one of the DAQ units). Time to reach the set point temperature (e.g. a few seconds for the outer ring) and temperature stability (e.g. $|\Delta T| < 1$ μK for the outer ring) are typical optimization goals.

4.2 Data Analysis

To find the absorptance of a sample from a calorimetric absorption measurement, one needs to determine the incident power P_0 and the power P_{abs} absorbed by the sample. The HRT mounted on the measurement ring is to measure the temperature change induced

by absorption. Since the HRT output is a voltage, we can cross-calibrate the HRT with a calibrated thermometer to determine the temperature change. To find the absolute absorbed power we then need to relate the voltage change (or temperature change) to dissipated or absorbed power. In the next sections the calibration procedure will be explained.

4.2.1 Measuring the Beam Power Incident on the Sample

To find the absorptance, we need first to measure the incident power. As mentioned in section 3.2, the temperature stabilization unit TS-2 (consisting of a Cernox® thermometer and an electric resistor) is mounted on the beam dump. Let's assume R_5 to represent the thermal link between the beam dump and the base plate (cf. Fig. 3.6(c)) and C_{BD} to be the heat capacity of the beam dump. By dissipating a known amount of power through the resistor of TS-2 and waiting long enough ($t >> R_5C_{BD}$), the temperature reaches the steady state and one can calibrate the temperature change of the beam dump against the power dissipated by the beam dump by finding the R_5 from Eq. (1.12). Hence, the dissipated power in the beam dump P_{bd} can be measured very accurately by monitoring the temperature change of the beam dump. Since the beam dump acts like a perfect black body and traps the incident light very efficiently, the measured P_{bd} during an absorption measurement is the transmitted power through the sample. In the absence of a test sample, the measured P_{bd} would be the incident power P_0. The latter scenario can be used to compare the measured P_0 at 4 K temperature to that measured at the room temperature.

Figure 4.1 shows the incident beam power measured at room temperature and at 4 K for several wavelengths. The incident power P_0 at room temperature was measured

after the collimating assembly (Fig. 3.6) with an optical power meter. A good agreement between the two measurements is evident. Since the ratio of the light beam coupled (from outside the cryostat) into the 4-K measurement chamber is 88% (+/- 4%), for wavelength range of 330 nm to 1700 nm, we can simply determine the incident power at 4 K by measuring the beam power outside the cryostat (see Fig. 3.4).

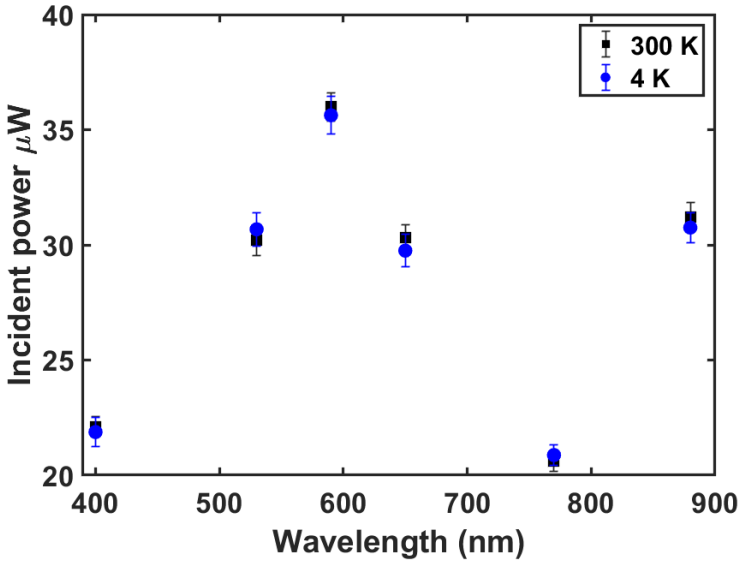

Figure 4.1: Power incident on the beam dump at 4 K determined from the temperature increase and power measured at 300 K using an optical power meter. The power at room temperature was measured after the collimating assembly inside the measurement chamber. The blue and black points are average of 3 and 10 measurements, respectively. The error bars show the standard deviation of these measurements.

4.2.2 Calibration of the High Resolution Thermometer

We can easily determine the calibration factor V/K to relate the voltage signal of the HRT of the measurement unit to a temperature change. To this end, a cross-calibration

was performed by mounting a calibrated Cernox® thermometer next to the HRT on the measurement ring. The results are shown in Fig. 4.2. For this calibration, the temperature is increased up to 2 mK using an ohmic resistor. A calibration factor of about 1.4 V/μK was obtained for a trapped magnetic field of 100 Gauss.

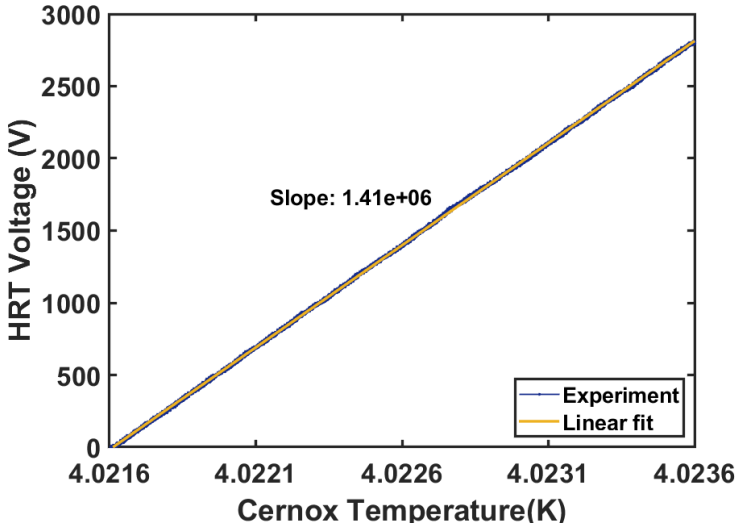

Figure 4.2: Cross-calibration of the HRT (of the measurement unit) with a calibrated Cernox® thermometer mounted next to the HRT. The slope of the linear fit line provides the calibration factor. The fluctuations of the Cernox temperature (and the HRT voltage) are within the width of the fitted line.

The HRT - TS-3 (HRT of the temperature stabilization unit mounted on the reference ring) was calibrated similarly and a calibration factor of 110 V/mK was obtained for a trapped magnetic field of 10 Gauss.

The ratio V/K is measured at each cooldown to obtain the exact calibration factor. It has to be noted that the calibration factor V/K did not change more than +/- 3% for different cooldowns for the same HRT.

4.2.3 Measuring the Temperature (Voltage) Change of a Sample

To measure the absorption induced temperature (voltage) change of a sample, the tunable light source or laser is periodically turned on and off with frequency f_m using the shutter integrated into the monochromator (electromechanical shutter, labeled MS in Fig. 3.4) while the temperature change ΔT (or voltage change ΔV) of the sample is measured with the HRT.

Let's assume C_{SA}, C_T, C_S and are the heat capacities of the sample, temperature sensor and measurement unit. R_{SA} and R_T represent the thermal resistances between the measurement ring, and the C_{SA} and C_T, respectively.

The modulation frequency f_m is chosen so that:

(i) $R_{SA}C_{SA} << \Delta t$ and $R_TC_T << \Delta t$. Hence, temperature differences are negligible within the measurement unit and we only have to consider the total heat capacity of the measurement unit C_S. The time constants $R_{SA}C_{SA}$ and R_TC_T are estimated to be ~50 ms and ~80 ms, respectively.

(ii) The excitation period is short compared to the thermal time constant of R_1C_S. R_1 is the thermal resistance between the measurement unit and the damping ring, see section 3.2. The time constant R_1C_S is estimated to be ~70 minutes. Hence, when the beam is on, a temperature slope of

$$\frac{\Delta T(t)}{\Delta t} = \frac{P_{abs}}{C_S} \tag{4.1}$$

is added to the always present background drift. P_{abs} is the absorbed power.

(iii) There is a reasonable compromise of signal-to-noise ratio and the overall measurement

time.

Figure 4.3 shows the temperature change of a fused silica sample when it is illuminated with 20-µW of optical power modulated at f_m=50 mHz at a wavelength of 639 nm. The communication between the PC software and the readout hardware for the two HRTs limits our sampling rate for the temperature readout to 200 ms.

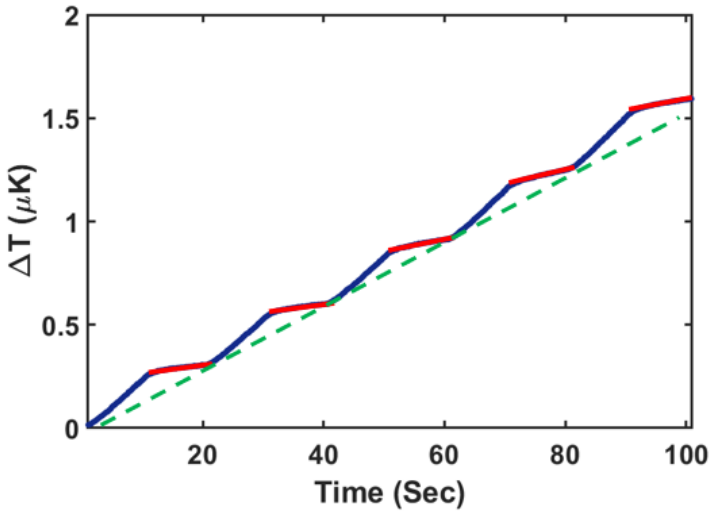

Figure 4.3: Temperature change of a 3-mm thick, 25-mm diameter fused silica sample in the measurement unit at 4 K when illuminated with 20-µW optical power at 693 nm with a beam-on/beam-off with period of 20 s. The temperature was read every 200 ms. The temperature fluctuations are within the line thickness. The green dashed line shows the background temperature drift. The red lines show the dark cycles (excitation source off).

The small temperature increase during the dark cycles (red lines in Fig. 4.3) is a result of still ongoing heat transfer from the excited sample volume and thermalization of the measurement unit. Although the measured temperature change of the sample can be used to estimate the absorbed power after doing a proper calibration, a frequency-domain analysis gives us a more reliable path. This is particularly true for small P_{abs} where ΔT

cannot be clearly distinguished from noise in a plot like the one shown in Fig. 4.3. This analysis is very similar to a lock-in technique where the contribution from signals that are not at the reference frequency is attenuated depending on the detection bandwidth. The lock-in technique takes advantage of the fact that noise is spread over a broader range of frequencies than the signal. Hence by reducing the bandwidth of the measurement, the measurement becomes less sensitive to the noise.

4.2.4 Amplitude Spectrum of the Temperature (Voltage) Data

Fourier-transformed amplitude spectra of a temperature change $\Delta T(t)$ (or voltage change $\Delta V(t)$) help to study certain features of the temperature signal, e.g., a distinct peak at the modulation frequency f_m or peaks corresponding to harmonics of f_m, and spectral features of background noise. Spectral analysis has often been used to characterize the performance of high resolution thermometers. Also, a frequency-domain analysis provides a way of visualizing the response of the system to changes in the measurement thermal network and to better understand the qualitative behavior of the system.

Suppose that our time-dependent temperature $T(t)$ is sampled at N equidistant points in a time interval of length $\mathcal{T}$, that is $\mathcal{T}=N\Delta$, where Δ is the sampling interval and N should (preferably) be an even integer. The well-known one-sided power spectrum (also called power spectral density or PSD) at frequency f_k, for a single measurement, $\hat{S}_T(f_k)$, can be written as [111]:

$$\hat{S}_T(f_k) = 2\frac{\Delta^2}{\mathcal{T}}|\Upsilon(f_k,\mathcal{T})|^2 \qquad k = 0,1,\dots,\frac{N}{2} \quad (4.2)$$

where f_k is the kth Fourier frequency,

$$f_k = \frac{k}{\mathcal{T}}, \qquad k = 0,1,\ldots,\frac{N}{2} \quad (4.3)$$

and $\Upsilon(f_k, \mathcal{T})$ is the fast Fourier transform (FFT) of the temperature $T(t)$ at frequency f_k. The amplitude of the power spectral density is the square root of the $\hat{S}_T(f_k)$. To reduce the effect of noise, the amplitude spectrum $\hat{\mathrm{A}}_T(f_k)$ is typically averaged over several, let's say n, measurements.

$$\hat{\mathrm{A}}_T(f_k) = \frac{\sqrt{2}\Delta}{n\sqrt{\mathcal{T}}}\sum_{i=1}^{n}|\Upsilon_i(f_k,\mathcal{T})| \qquad k = 0,1,\ldots,\frac{N}{2} \quad (4.4)$$

In our data analysis, Matlab software is used to find the amplitude spectrum of the temperature measurement. For a measured temperature change $\Delta T(t)$, such as the one shown in Fig. 4.3, the background drift is removed by detrending the temperature data to simplify the data analysis. For example, after subtracting a linear contribution, $\propto at$, from the measurement shown in Fig. 4.3, we approximately obtain a triangle function for the right choice of the parameter a, Fig. 4.4(a). The amplitude spectrum is then calculated using Eq. (4.4). Figure 4.4(b) shows the calculated amplitude spectrum of the temperature change $\Delta T(t)$ for an integration time of 100 s and averaged over 20 measurements.

The distinct peak labeled A in Fig. 4.4(b) stems from the triangular wave with a modulation frequency of f_m=50 mHz and is a measure of P_{abs} (after subtracting the noise background). Peaks labeled B arise from higher harmonics whose presence is expected from the triangular shape of $\Delta T(t)$. The spectral component at 1.5 Hz is produced by the PTC.

The signal-to-noise ratio in our sensitive detection measurement scheme is inversely proportional to the square root of the measurement integration time. In principle, increasing the integration time could further improve the temperature sensitivity. However, we feel that we are already at the limit of what we consider practical integration times for a spectroscopic measurement, about 100 s per wavelength sampling point.

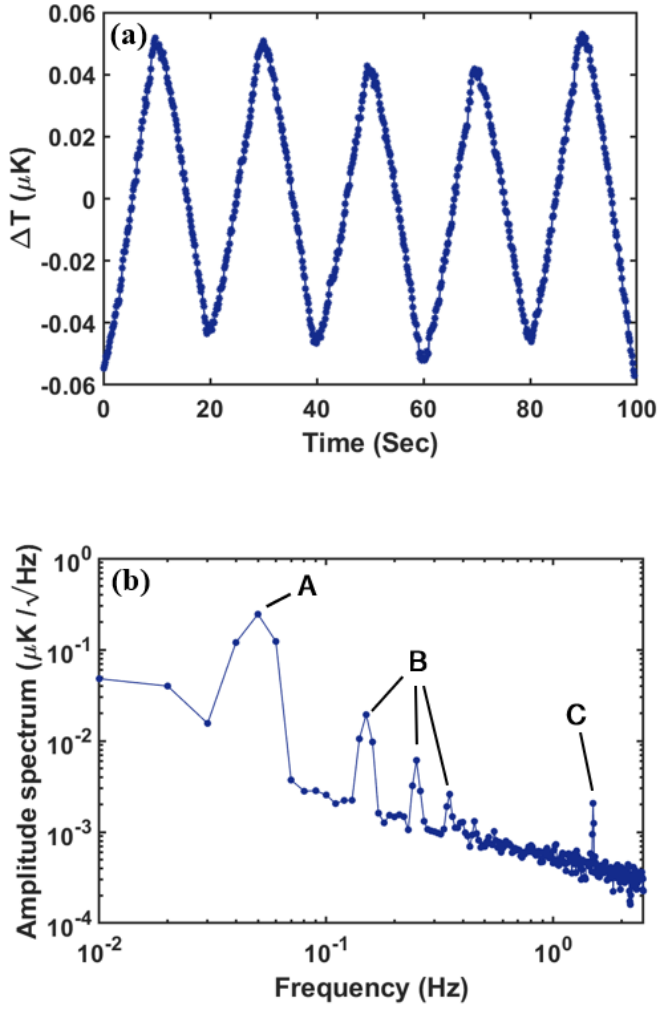

Figure 4.4: (a) Detrended temperature change $\Delta T(t)$ of a fused silica disk (1" diameter, 3 mm thick) illuminated periodically (f_m=50 mHz) with 20-μW optical power at a wavelength of 639 nm. (b) $\hat{A}_T(f_k)$ of $\Delta T(t)$ showing the 50 mHz modulation component (A), its higher harmonics (B) and a 1.5-Hz component produced by the PTC.

According to the sampling theorem, the amplitude spectrum is meaningful only for frequencies up to the Nyquist critical frequency f_c=1/(2Δ)=2.5 Hz to avoid aliasing. The full width at half maximum (FWHM) of peaks A, B and C are the same and equal to $2/\mathcal{T}$.

To find the temperature change corresponding to one illumination period, the following steps are taken. First, the noise background is subtracted from the amplitude spectrum for each frequency sampling point under the peak A. The resulting values are added to yield the temperature amplitude in K/√Hz at the corresponding modulation frequency f_m. Second, the sum is divided by the square root of the integration time to find the amplitude of the temperature change for one period in units of K. Third, the result is multiplied by 2 to find the peak to peak difference for one period. The latter is the absorption-induced temperature change for one period.

4.2.5 Absorbed Power Calibration

To find the power P_{abs} absorbed by the sample, calibration is performed with periodic (frequency f_m) heating using the electric resistor r (with a 1 kΩ resistance) mounted on the measurement ring (see Fig. 3.6(c)). Different currents are applied through the resistor r and the amplitude spectrum for each dissipated power is calculated (for the same integration time as the absorption measurement) by following the same approach as the one explained in the previous section. By measuring the peak heights, at frequency f_m, we can plot the dissipated power versus voltage change in V (or temperature change in K). A linear fit to the plot will yield the calibration.

Figure 4.5 shows an example calibration plot for the dissipated power versus

temperature change for the 1-inch, 3-mm thick fused silica sample. For this test, a calibration factor of 0.25 nK/pW is obtained. By multiplying this measured calibration factor to the calibration ratio V/K, obtained in section 4.2.2, one can simply find the calibration factor for the dissipated power versus the voltage change as well. It has to be noted that the absorbed power determined from the voltage change or the one determined from the temperature change would be exactly the same.

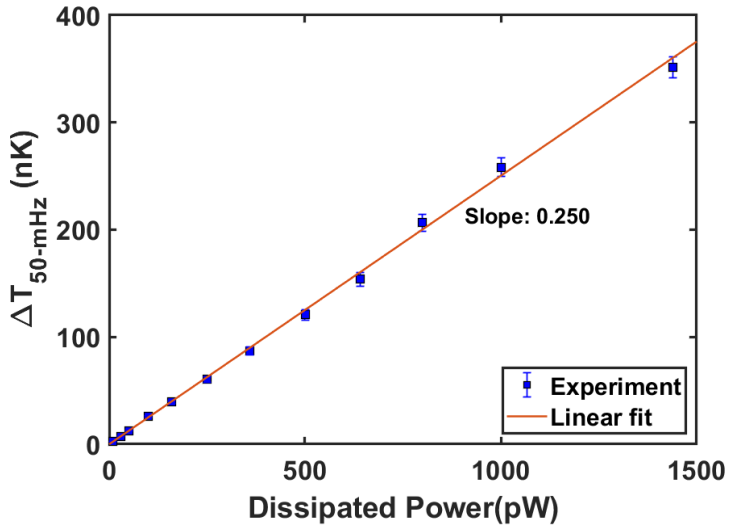

Figure 4.5: Measured temperature change of the measurement unit versus the power dissipated by an electric heater (ohmic resistor). The current was turned on and off with a frequency of 50 mHz. The integration time was 100 s. The slope of the linear fit line provides the calibration factor. The blue points are averages of 10 measurements. The error bars show the standard deviation of these measurements. For the first few points the error bars are within the width of the blue marks.

Using Eq. (4.1), a heat capacity of $C_S \approx 40$ mJ/K can be estimated for the measurement unit (which includes the sample). The heat capacity of our sample (1-inch, 3-mm thick fused silica disk) at 4 K is ~1.5 mJ/K and much smaller than C_S. Therefore the calibration factor does not change for similar samples as long as the heat capacity

remains << C_S.

Chapter 5

Noise Characteristics and Sensitivity

In this chapter, we analyze various noise sources that limit the performance of our calorimeter for optical absorption measurements. The effect of PID controlled temperature control units on the temperature stability inside the measurement chamber will be described. The sensitivity limits of the developed pico-Watt calorimeter will be discussed at the end of this chapter.

5.1 Noise Analysis

To reach high sensitivity of our calorimetric absorption measurement, we need to improve the noise characteristics of our apparatus. To this end, first, we need to identify

the noise sources and characterize their contribution to the noise that is relevant for the measurement of the induced temperature change of the sample. In a cryostat, the noise from vibrations and the room temperature electronics is well-known. The noise from vibrations can be divided into three main categories: seismic (ground) vibrations, mechanically coupled vibrations of the PTC to the experimental setup, and acoustic vibrations. By acoustic vibrations, we mean vibrations caused by air pressure variations. Many of the sources that generate seismic and mechanically coupled vibrations, generate acoustic vibrations as well. A vacuum pump located on the floor, a compressor or even the rotary valve are a few examples which could affect our experimental setup specifically. Hence, the effect of seismic vibrations and mechanical vibrations will be examined here and the characteristic noise will be compared to the fundamental thermal noise of our thermal network.

To find the characteristic noise spectrum, the amplitude spectrum of the temperature readouts of the HRT is determined, see section 4.2.4, while the optical excitation is off.

5.1.1 Seismic Vibrations

Vibrations of the laboratory floor are called seismic vibrations here. Common seismic vibration sources in a laboratory are foot traffic, vehicular traffic (on a nearby street), the air conditioning system and a vacuum pump located on the floor near the experimental setup. Dissipation of mechanical vibrations that reach the cryostat and measurement chamber lead to local temperature changes.

Our cryostat resides on an optical table. To reduce the transmission of seismic vibrations to the experimental setup, the table is floated using pneumatic isolators (legs). They act as mechanical low-pass filters.

After floating the optical table and waiting for a few hours so that the temperature stabilizes, the temperature of the measurement ring is recorded with the HRT for several hours. The noise amplitude spectrum is obtained for a recording time of 1000 s, a sampling rate of 200 ms and averaged over 40 spectra. Figure 5.1 compares the noise amplitude spectrum of the measurement unit for the two scenarios - when the optical table is floated and when it is not floated. In both measurements all PID controlled temperature stabilization units were activated.

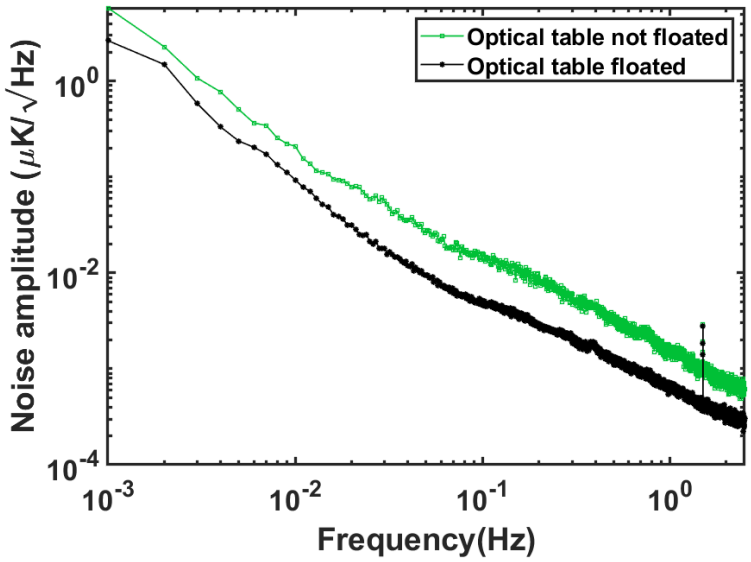

Figure 5.1: Comparison of the noise amplitude at 4 K measured at the measurement ring for two cases: the optical table is floated and the optical table is not floated. Frequencies < 1 Hz are of interest for our absorption measurements with typical modulations frequencies in the 0.01 Hz range.

The improvement of the background measurement noise over a broad frequency

range, shows the effect of seismic vibrations and the benefit of floating the optical table. The temperature stabilization achieved for different stages within the 4-K measurement chamber will be discussed in the next section.

5.1.2 Mechanical Vibrations

In a cryostat where a PTC provides the cooling, mechanical vibrations directly coupling into the cryostat are another main source of vibration induced temperature noise. Even though no moving components are connected to the low-temperature unit, the rotary valve, the pressure oscillations of the working gas, and the gas high/low pressure compressor lines (flexible tubes) will generate and transmit vibrations. Since there is always a mechanical link between the compressor, rotary valve, and flexible tubes of the PTC and the cold stage of the cryostat, these vibrations can propagate to the coldest parts of the cryostat, dissipate and generate an excess heat load. Vibrations originating in the pulse tube cooler have been investigated by several groups and methods have been utilized to measure, analyze and reduce their effect on low temperature measurements [70], [112]–[115].

In one of the early papers, the mechanical vibrations caused by the pulse tube coolers were investigated [112]. Figure 5.2 shows the vertical and horizontal displacement spectra of their PTC cold stage. An optical sensor was used to monitor the cold stage displacement of the PTC. The authors concluded that two kinds of vibrations exist. The first one is associated with the overall motion of the cold-head of the PTC, which is caused by the high/low pressure compressor tubes and vibrations from the compressor and rotary

valve. The second one is the vibration of the cold stage of the PTC which is caused by pressure oscillations of the working gas.

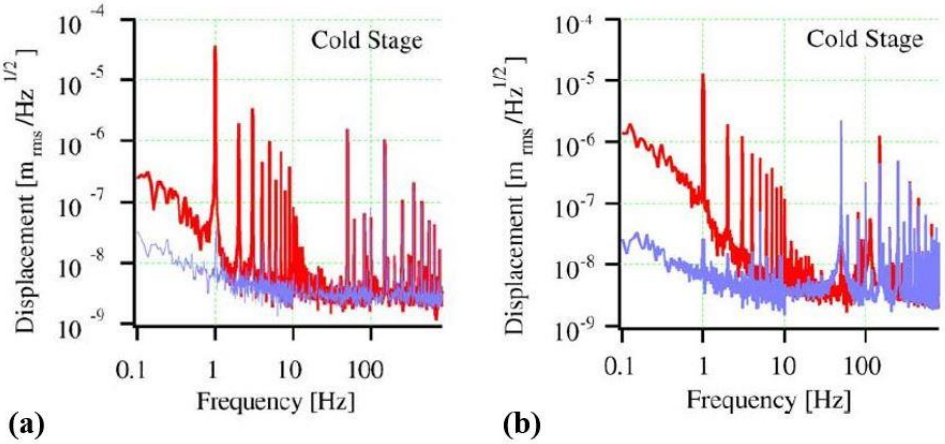

Figure 5.2: Vibration spectra for a Sumitomo pulse tube cooler. (a) Vertical vibration spectrum, (b) horizontal vibration spectrum. The vibration spectra of the PTC are shown with red lines and the blue lines show the noise spectra of optical sensors. The sharp peaks at 1 Hz and higher harmonics are associated with a rotary valve operating at 1 Hz and periodically connecting the Sumitomo PTC to the high-pressure and low-pressure side of the compressor. Adapted from Ref. [112].

To address the vibration induced by pressure oscillations of the working gas, we have deployed flexible copper braids to mechanically decouple the cold stages of our PTC from the 4-K and 60-K parts, see section 2.2.2. To reduce the propagation of vibration from the compressor, the rotary valve, and the flexible tubes to our cryostat, high/low pressure flexlines are suspended from the ceiling structure by elastic bands instead of non-elastic ropes, see Fig. 5.3. In addition, the molecular sieve filter is suspended from the ceiling by the elastic bands.

Figure 5.4 shows the (temperature) noise amplitude spectra for the two discussed scenarios, obtained in the same way as explained in the previous section. The optical table

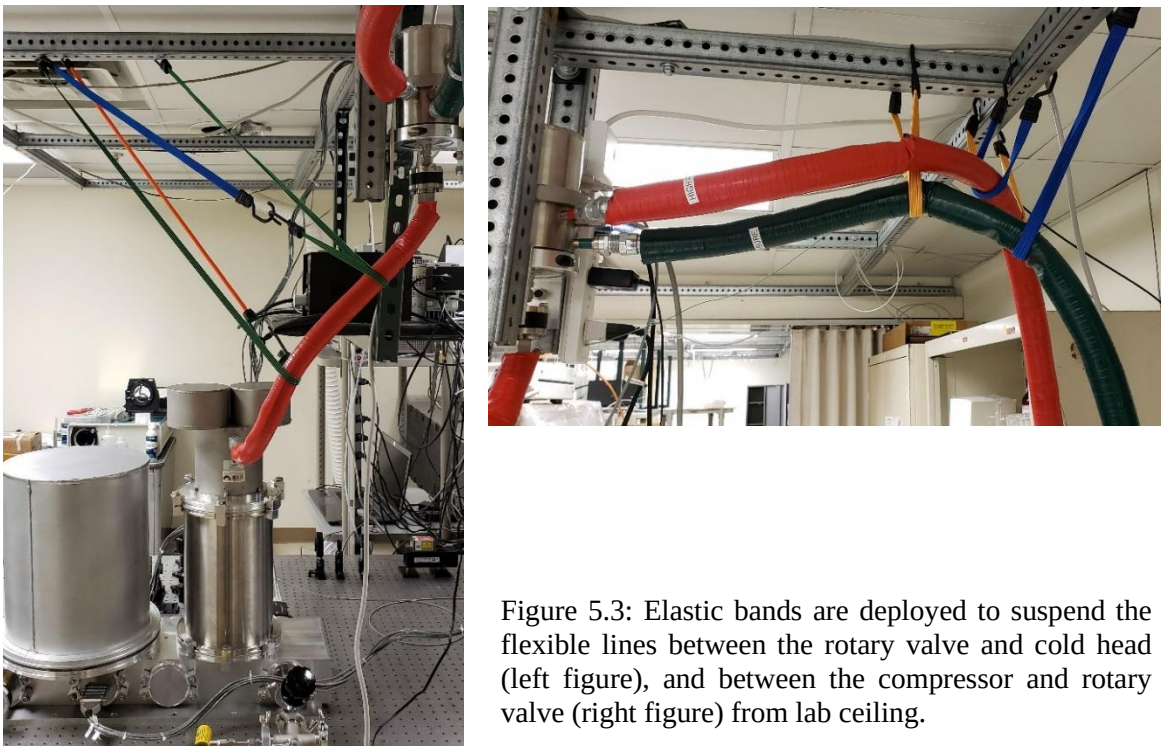

Figure 5.3: Elastic bands are deployed to suspend the flexible lines between the rotary valve and cold head (left figure), and between the compressor and rotary valve (right figure) from lab ceiling.

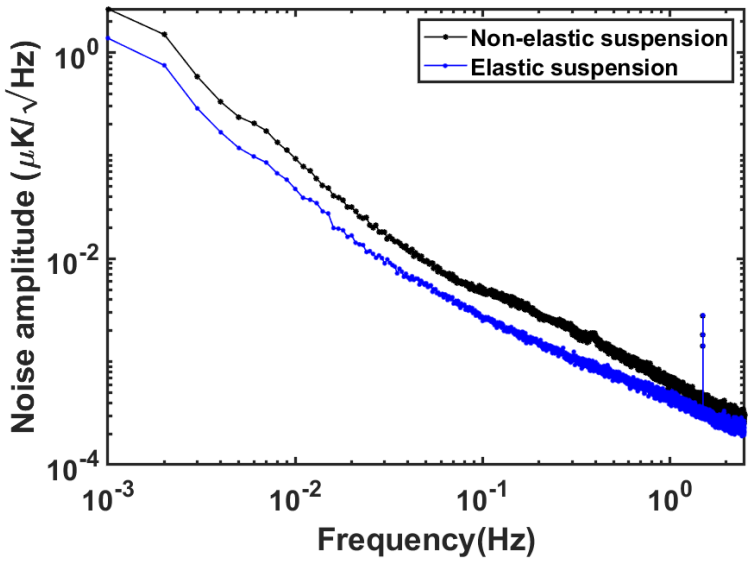

Figure 5.4: Measured (temperature) noise amplitude when the high/low pressure flexlines and the molecular sieve filter are suspended from the ceiling structure by elastic and non-elastic ropes.

is floated in both cases. The soft mechanical supports damp the amplitude of vibrations transferred to the cryostat.

The vibration-induced noise affecting the temperature data recorded by the HRT of the measurement unit is observed very explicitly by the previous tests. To further study the vibration-induced impact on our measurement, the noise spectra with and without the PTC running are compared. Turning off the PTC, means turning off the compressor and the rotary valve at the same time. There is a temperature increase right after turning off the compressor. The base plate temperature increases by ~0.7 K and ~1.6 K after 20 seconds and 50 seconds, respectively. To ensure that the temperature at the measurement unit remained within the dynamic range of the HRT (± 2 mK), the temperature is recorded for only 20 seconds after turning off the PTC. The measurement is repeated ten times and the results averaged, see Fig. 5.5. In both measurements, the optical table is floated and the

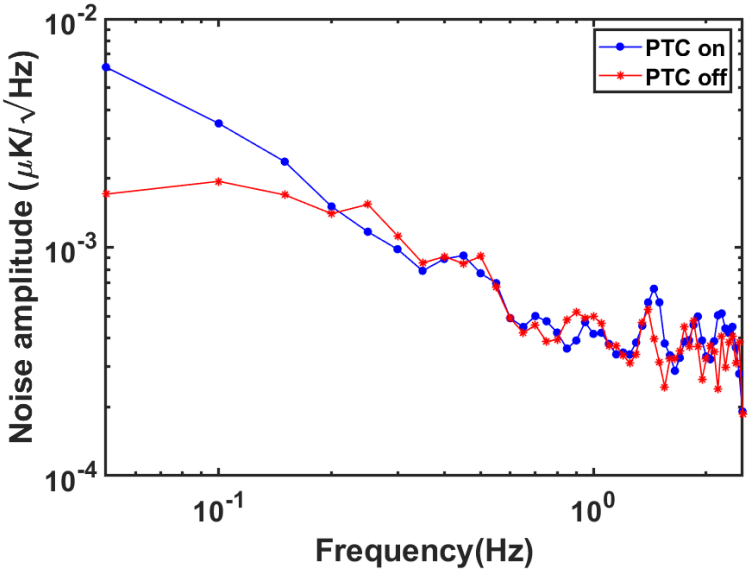

Figure 5.5: Measured (temperature) noise amplitude spectrum when the PTC is on and off. The integration time for each measurement is 20 seconds. Each spectrum is an average over 10 measurements.

PID controlled temperature stabilization units are not activated. Also, elastic bands are used for suspension.

The PTC has a strong affect at frequencies below 0.2 Hz. Obviously, our mitigation measures discussed above dampen the PCT-induced noise effectively for higher frequencies. However, a typical modulation frequency used in our absorption measurements is 50 mHz. At this frequency, the PTC contribution to the background noise is still substantial. Since the integration time for each measurement was short, we did not have enough resolution to resolve the 1.5-Hz component produced by the PTC.

5.1.3 Room Temperature Electronics

Noise from room temperature electronics, which could contribute to the 4-K measurement noise, consists of two parts: - (i) the noise from the SQUID electronics and (ii) the noise from the DAQ units. The noise contribution of the PCI1000 SQUID electronics box at room temperature, while the SQUID itself is not operating, is crucial for the noise characteristics of the measurement system. Furthermore, the 4431 DAQ unit is used to readout the outputs of the SQUID electronics and the 6212 DAQ unit is used as a voltage source for electric heaters (for temperature stabilization purposes). Hence, their noise contributions must be understood as well.

To evaluate the noise (i), the output of the SQUID electronics box (in V) is read out by the 4431 DAQ device and the data are recorded for about two days. To evaluate the noise (ii), the analog output of the 6212 DAQ unit is connected directly to the 4431 DAQ device and the signal is recorded similarly. The results are shown in Fig.5.6 together with

the overall measurement noise at 4 K seen by the HRT of the measurement unit.

All data were obtained while the optical table was floated, the PID controlled temperature stabilization units activated, and elastic bands suspended the flexlines and the molecular sieve filter. It is evident that the noise from room temperature electronics is negligible compared to the characteristic noise spectrum measured by the HRT of the measurement unit at 4 K.

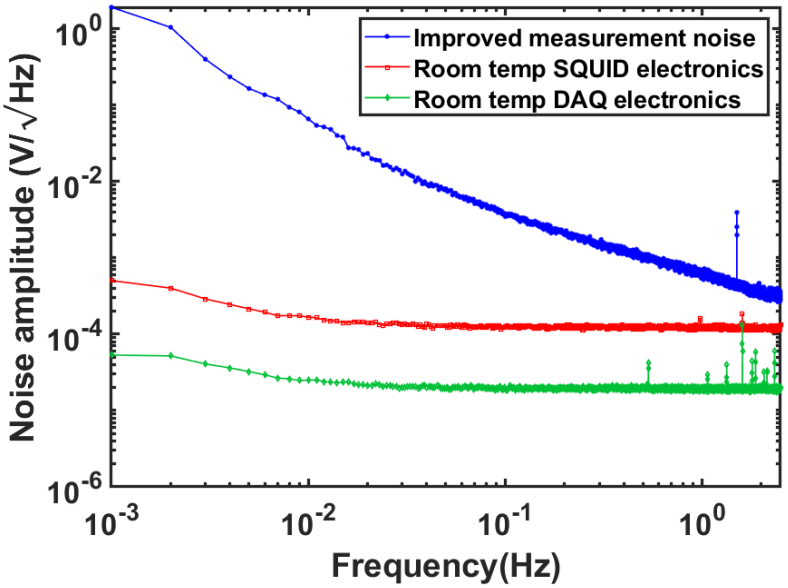

Figure 5.6: Measured noise amplitude spectra from room temperature electronics for noise sources (i) and (ii). Each of these spectra is an average of 200 spectra, each with an integration time of 1000 s. For comparison, the overall measurement noise is also shown (average of 40 spectra with an integration time of 1000 s).

5.1.4 Impact of Movement and Temperature Change of the Air Outside the Cryostat

To estimate the effect of air movement and temperatures changes induced by the

air conditioner, a quick test is improvised. A carboard box is placed around the cryostat to change air movement in the immediate vicinity of the instrument. The noise amplitude spectrum is obtained again for an integration time of 1000 s and is averaged over 40 spectra. Figure 5.7 compares the two noise amplitude spectra obtained with and without the box around the cryostat. In both tests, the optical table is floated, the PID controlled temperature stabilization units are activated, and the elastic bands are deployed to suspend the flexlines and molecular sieve filter.

It can be seen that the noise amplitude spectra are almost identical in the frequency range of interest. This result indicates that air movement and periodic air temperature changes from the HVAC system does not critically affect our background noise.

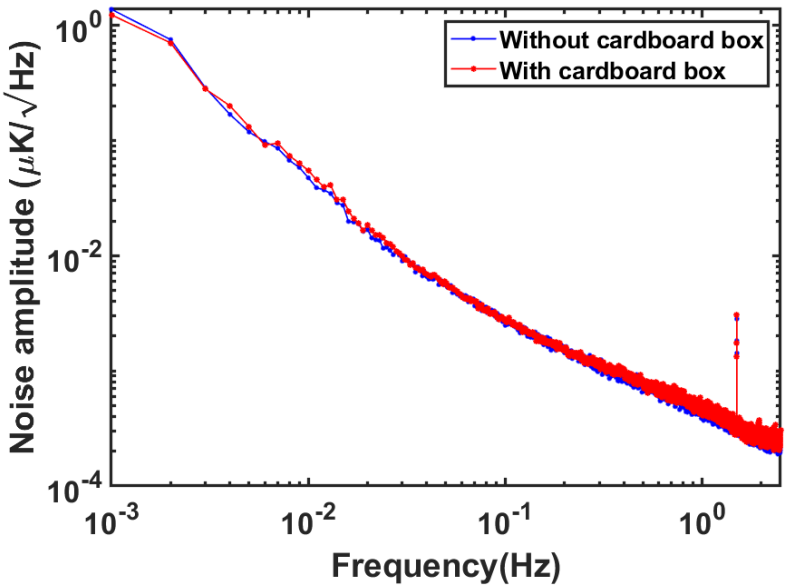

Figure 5.7: Noise amplitude spectra obtained with and without a cardboard box around the cryostat.

5.1.5 Noise due Thermal Fluctuations

Thermal fluctuation noise is a fundamental phenomenon that arises from the random motion of atoms due to their thermal energy. For an electric resistor with resistance $\acute{R}$ at a non-zero temperature T this produces a (Johnson-Nyquist) noise voltage of [116], [117],

$$V_n = \sqrt{4k_B T \acute{R}} \tag{5.1}$$

where k_B is the Boltzmann's constant and V_n is the root mean square noise voltage per unit frequency interval. An equivalent electric circuit is an ideal noiseless resistor in series with an AC voltage source with a magnitude equal to V_n. According to the fluctuation-dissipation theorem a similar model applies to a thermal resistance R. Instead of a noise voltage, we can introduce thermal noise given by [118], [119],

$$T_n = \sqrt{4k_B T^2 R}, \tag{5.2}$$

Where T_n is the root mean square temperature fluctuation per measurement bandwidth. To estimate the contribution of this fundamental noise to our measurement noise, we use the thermal capacities and thermal resistances of our thermal network (Fig. 3.6) in analogy to the treatment of electrical circuits. The network is shown in Fig.5.8.

The sample and the temperature sensor are represented by thermal capacities C_{SA} and C_T, respectively. The thermal resistors R_{SA} and R_T represent the thermal link between measurement ring, with thermal capacity C_{MR}, and the C_{SA} and C_T, respectively. Thermal resistor R_B stands for the thermal link between the 4-K base plate, with thermal capacity

C_{BP}, and the thermal bath, with thermal capacity C_B. The 2nd stage of the PTC and the 4-K parts (except the base plate) in thermal contact with the PTC, are considered as part of the thermal bath. Thermal resistors R_1, R_2, R_3, and R_5 are defined in the same way as they defined in section 3.2. In addition, the damping ring, reference ring, and the beam dump are represented by the thermal capacities C_{DR}, C_{RR}, and C_{BD}, respectively.

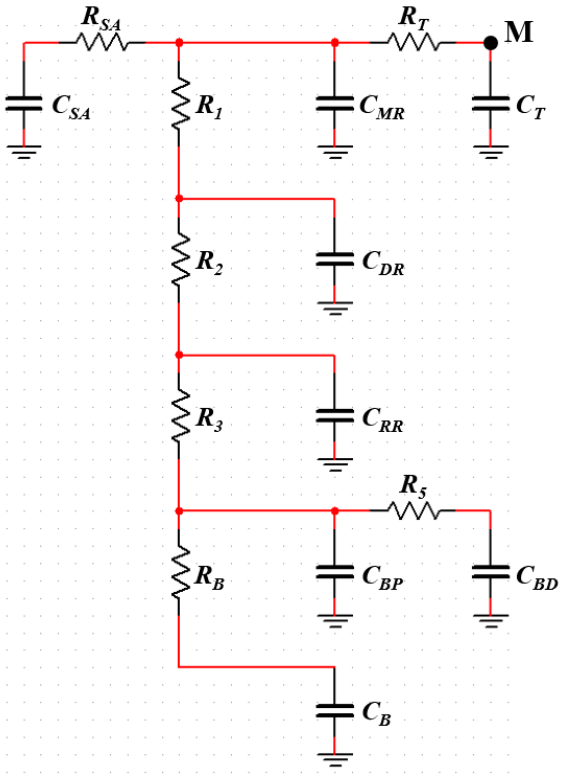

Figure 5.8: Thermal network of our measurement system represented in terms of thermal capacities and thermal resistances in analogy to electrical circuits. Thermal capacity of different components of the thermal network is denoted by C: C_{SA}: sample, C_T: temperature sensor, C_{MR}: measurement ring, C_{DR}: damping ring, C_{RR}: reference ring, C_{BP}: base plate, C_{BD}: beam dump, C_B: thermal bath. Thermal resistance between different thermal capacities is denoted by R: R_{SA}: sample and measurement ring, R_T: temperature sensor and measurement ring, R_1: measurement ring and damping ring, R_2: damping ring and reference ring, R_3: reference ring and base plate, R_5: base plate and beam dump, R_B: base plate and thermal bath.

To model the thermal noise in our network, the NI Multisim^{TM} software is used. In analogy to electrical circuits, each thermal resistor can be represented by a noise free thermal resistor in series with an AC source with a magnitude equal to T_n (in K/√Hz), given by Eq. (5.2). Since the temperature where the absorption measurement is conducted is about 4 K, T = 4 K for all thermal resistors. The measured (or estimated) values of the thermal resistances and the thermal capacities, used in the simulation, are summarized in table 5.1 and table 5.2.

Table 5.1: Measured/estimated values of thermal resistances of the thermal network shown in Fig. 5.8.

Thermal resistance	R_{SA}	R_T	R_1	R_2	R_3	R_B	R_5
Measured/estimated value (K/W)	50	80	10^5	10^5	1400	9	50

Table 5.2: Measured/estimated values of thermal capacitances of the thermal network shown in Fig. 5.8.

Thermal capacitance	C_{SA}	C_T	C_{MR}	C_{DR}	C_{RR}	C_{BP}	C_{BD}
Measured/estimated value (J/K)	0.001	0.001	0.038	0.020	0.1	2.3	0.08

The thermal noise at the location of the temperature sensor (point **M**), owing to the thermal fluctuation of a specific thermal resistor, is probed by sweeping the frequency of the AC source of that thermal resistor across the desired range of frequencies (e.g. 1 mHz to 2.5 Hz). For taking phase into account, the thermal noise due to each thermal resistor is evaluated separately. By monitoring the frequency response of the thermal circuit at point **M,** the thermal noise contribution from the specific thermal resistor is determined. The total thermal noise is then determined by calculating the root sum square of the thermal

noises produced by all thermal resistors.

Figure 5.9 compares the theoretical noise spectrum due to thermal fluctuations to the actual characteristic noise spectrum measured by the HRT of the measurement unit. One can realize that the contribution of the thermal noise to the measured characteristic noise for frequencies below 0.1 Hz is negligible. Hence the thermal noise is not the limiting factor in our absorption measurement with modulation frequencies in the sub 0.1-Hz range. Figure 5.9 also suggests that for frequencies > 1 Hz the fundamental thermal noise may become a major component of the overall noise budget.

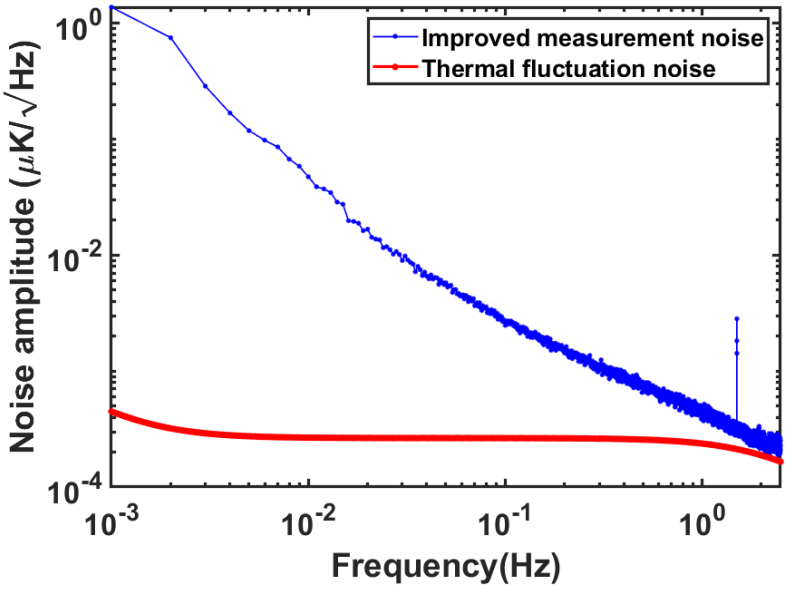

Figure 5.9: Estimated theoretical thermal noise amplitude spectrum due to thermal fluctuation. For comparison the measured overall noise spectrum is also shown.

5.2 Temperature Stabilization of Thermal Network

As mentioned in sections 3.2 and 4.2.2, the PID controlled temperature stabilization

units (TS) are used to separately stabilize the temperatures of the 4-K base plate, the beam dump, and the reference ring. While the TS-2 suppresses the periodic temperature change introduced by the modulated optical pump beam, the TS-1 and TS-3 reduce the cyclical temperature swings (~100 mK) at the PTC 2nd stage and other temperature perturbations before they reach the measurement unit.

Figure 5.10 (left) compares the temperature noise amplitude at the base plate without active stabilization (black curve) to the spectrum with TS-1 activated (red curve). Figure 5.10 (right) compares the temperature noise amplitude at the reference ring without any active stabilization (brown curve) to the spectrum with the TS-1 activated (orange curve) and to the spectrum with TS-1 and TS-3 activated (blue curve). Control TS-1 reduces the base plate temperature noise at frequencies below ~10 mHz. A spectral component at 1.5 Hz caused by the PTC is clearly visible in the spectrum at the reference ring. The total temperature rms value from 1 mHz to 2.5 Hz at the reference ring with the two control units on, is about 700 nK compared to about 500 μK for the base plate without stabilization. To compare to literature data, the total rms value was simply determined from relation [111],

$$rms = \sqrt{\sum_{k=0}^{N/2} \left|\hat{A}_T(f_k)\right|^2 \frac{1}{\mathcal{T}}} \tag{5.3}$$

where $\hat{A}_T(f_k)$ is the amplitude spectrum of the temperature data $T(t)$ at frequency f_k, see Eq. (4.3) and Eq. (4.4). $\mathcal{T}$ and N are the integration time and the number of sample points, respectively.

The 700-nK temperature rms of the 4-K reference mass compares favorably to the quietest cryostats with PTC (standard deviation of measurement chamber of 21 µK at 5 K during 12 hours) [120]. It should be mentioned that similar stability was obtained when 15 mW of optical power was dissipated through the beam dump, see section 6.2.

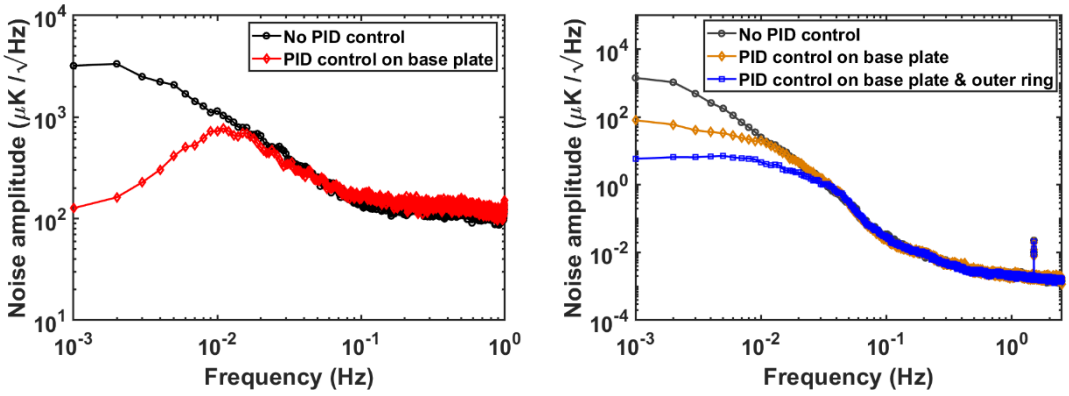

Figure 5.10: Left: Temperature noise spectrum of the 4-K base plate without any temperature stabilization (black curve) and with PID control TS-1 activated (red curve). Right: Temperature noise spectrum of the reference ring without any temperature stabilization (brown curve) with the TS-1 activated (orange curve) and with TS-1 and TS-3 activated (blue curve). Data were taken with the optical excitation off and an integration time of 1000 seconds. The sampling rate for the temperature measurement of base plate and reference ring was 500 ms and 200 ms, respectively. The noise spectrum is averaged over 50 measurements.

5.3 Sensitivity of the Calorimetric Absorption Measurement

To demonstrate the practical capabilities of the optical calorimeter we measured the minimum detectable absorbed power P_{min} and the minimum detectable temperature change ΔT_{min}.

Figure 5.11 shows the amplitude spectrum of the temperature change (see section 4.2.4), measured by the HRT of the measurement unit, when 10 pW of power was dissipated with periodic (frequency f_m=50 mHz) heating using the electric resistor mounted on the measurement ring. The amplitude spectrum is obtained for an integration time of 100 seconds and averaged over 30 spectra. A peak value of about 12 nK/√Hz at 50 mHz is obtained for the spectral amplitude at 50 mHz, which corresponds to a temperature change of $\Delta T_{min} \approx 2.5$ nK during one excitation period. For a noise amplitude of about 6 nK/√Hz at 50 mHz, see Fig. 5.11, this suggests a signal-to-noise ratio (SNR) of one.

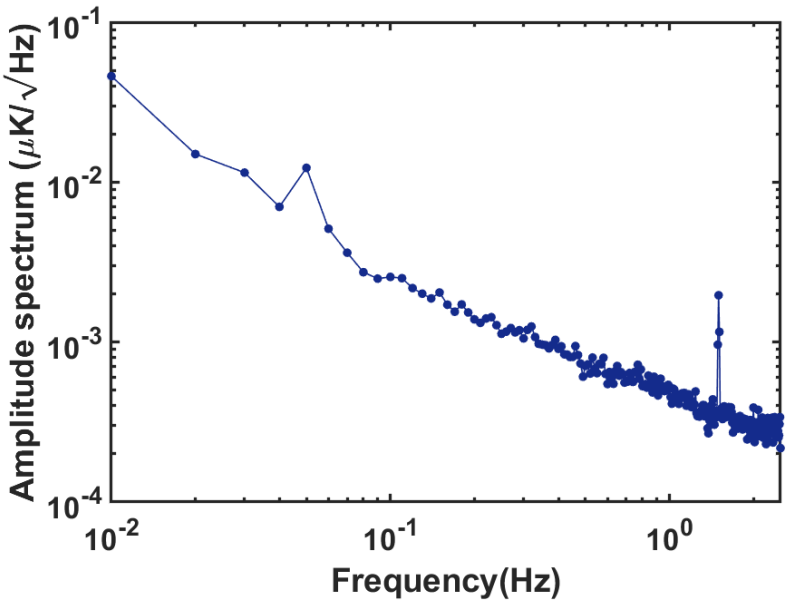

Figure 5.11: Amplitude spectrum of the temperature change measured by the HRT, when 10 pW of power was dissipated with periodic heating (frequency f_m=50 mHz). The 50-mHz modulation component corresponds to a temperature change of about 2.5 nK per heating period. The 1.5-Hz component is caused by the PTC.

According to Eq. (1.1), the minimum detectable absorbed power of 10 pW can be translated into an absorption sensitivity of $A_{min} \approx 300$ parts per billion (ppb) using the

available tunable light source, which delivers about 30 μW per 5 nm bandwidth from 330 nm to 1700 nm (see section 3.1.1).

5.4 Summary

The vibration-induced temperature noise was reduced by suspending the high/low pressure flexlines and the molecular sieve filter with flexible cords and floating the optical table. The contribution of the vibrations of acoustic origin, and of the room temperature electronics to the measured characteristic noise is negligible.

The fundamental noise due to thermal fluctuations is negligible at our modulation frequency of 50 mHz but may become important at frequencies > 1 Hz. Active temperature stabilization of key components of the cryogen-free cryostat produced residual temperature rms values of as low as 700 nK integrated from 1 mHz to 2.5 Hz in the reference ring. We were able to detect temperature changes as small as 2.5 nK at 50 mHz, for an integration time of 100 seconds, which corresponds to an absorbed power of 10 pW. This results in an absorption sensitivity of 300 ppb with only 30 μW of excitation power (tunable light source). At maximum illumination power of 100 mW (limited by the cooling power) we reach an absorption sensitivity of 0.1 ppb.

Chapter 6

Calorimetric Absorption Measurement Examples

To demonstrate the practical capabilities of the optical calorimeter at 4 K, the absorption spectrum of high-quality substrates and films with only a few μW of incident power is measured. The ultimate sensitivity of the instrument estimated in the previous chapter is tested at a selected wavelength by coupling a few mW of laser power into the cryostat.

6.1 Absorption Measurements with Spectral Resolution

To perform an absorption measurement with spectral resolution the tunable light source described in section 3.1.1 in detail was used. It delivered an average illumination power of 6 μW/nm from 330 nm to 1700 nm. The absorption-induced temperature change of the sample is sensed by the calibrated HRT (mounted on the measurement ring) and yields the power absorbed by the sample, see section 4.2. PID controlled temperature stabilization units are activated to produce a quiet thermal environment under load, see section 5.2.

The test samples were obtained from collaborators. Our absorption spectra were instrumental in the development of new mirror designs [121], [122] and in clarifying properties of coating materials [123] when exposed to high-power laser irradiation. The samples were:

1. A low-loss, IR-grade fused silica sample (substrate) provided by Heraeus.
2. Hafnium oxide thin films with varying oxygen content deposited on polished fused silica substrates. The samples are from the Laboratory for Laser Energetics, University of Rochester.
3. An Al_2O_3–HfO_2 nanolaminate-based mirror coating (for 355 nm radiation), deposited on a fused silica substrate. The sample was from the Laboratory of Thin Film Optics, Shanghai Institute of Optics and Fine Mechanics.
4. A 1064-nm high reflective mirror based on a multi-layer stack of HfO_2 and SiO_2 films deposited with different techniques (one with discrete interfaces between

the high-n and low-n coatings and the other one with co-evaporated interfaces). The samples were prepared by the Laboratory of Thin Film Optics, Shanghai Institute of Optics and Fine Mechanics.

6.1.1 Absorption of a Fused Silica Substrate

The first sample is a low-loss, IR-grade fused silica sample. The sample has a diameter of 1 in and a thickness of 3 mm. An HRT calibration factor of 0.25 nK/pW is obtained. The absorbed power P_{abs} of the fused silica samples is probed at ~4 K at normal incidence in 20-nm steps from 330 nm to 1700 nm with an average illumination power and bandwidth of 30 μW and 5 nm, respectively. The optical excitation is modulated (f_m=50 mHz). The integration time and the sampling rate are 100 s and 200 ms, respectively.

The absorptance of a substrate (coating) is defined as the ratio of the absorbed power by the substrate (coating) to the incident power [43]. For a known incident power of P_0 and an absorbed power of P_{abs} by the fused silica sample, the absorptance of the substrate, A_s, is:

$$A_s = {P_{abs}}/{P_0} \tag{6.1}$$

For a substrate thicker than the coherence length of the incident light, an incoherent superposition of excitation light bouncing back and forth in the substrate can be assumed and the above relation can be obtained easily, see appendix E. One can see that the substrate absorptance can be found by measuring the absorbed power. For a low-loss substrate

$A_s << 1$.

The absorption spectrum of the fused silica sample measured with the pico-Watt calorimeter is shown in Fig. 6.1 [124]. The sample is made from IR-grade fused silica. Thus the OH absorption peaks at 1390 nm and 940 nm are suppressed. The increase in absorption for shorter wavelengths is likely due to band tail states and excitation of impurity states in the band gap [125]. The error bars represent the uncertainty of the measurement which is about +/- 8% of the absorptance value at each wavelength. The uncertainty arises mainly from the variation of the incident power, cf. Fig. 4.1, and the calibration factor, cf. Fig. 4.5.

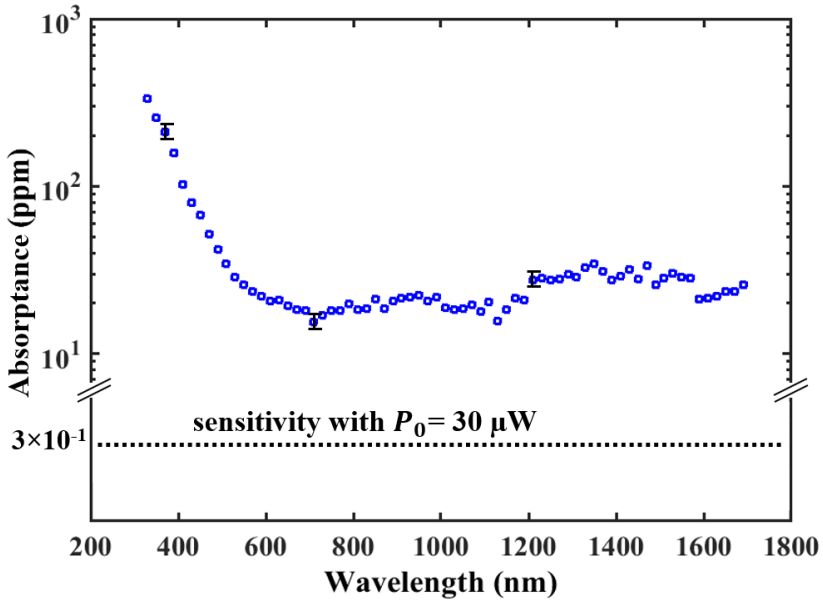

Figure 6.1: Absorption spectrum of a 3-mm thick fused silica sample (Heraeus Suprasil 300, 1 inch diameter) from 330 nm to 1700 nm. The wavelength sample point separation is 20 nm. The excitation source had a power of about 30 µW and a 5-nm bandwidth. For comparison, the dashed lines at ~0.3 ppm represent the absorption sensitivity for a signal-to-noise ratio of one, measured with 30 µW at a modulation frequency of f_m=50 mHz and 100 s integration time [124].

6.1.2 Absorption Spectrum of HfO_2 Thin Films

The absorption of two hafnium oxide thin films, one with standards oxygen content (EB1) and one with reduced oxygen content (EB2), is investigated to find characteristic optical signatures of oxygen vacancies in the film. Since the films are deposited on polished fused silica substrates (Corning 7980), absorption of a bare fused silica substrate is measured as reference. The hafnium oxide thin films with 175-nm physical thickness are deposited using conventional electron beam (e-beam) evaporation, where the oxygen content in the film is controlled by the deposition rate and oxygen back-fill pressure [123].

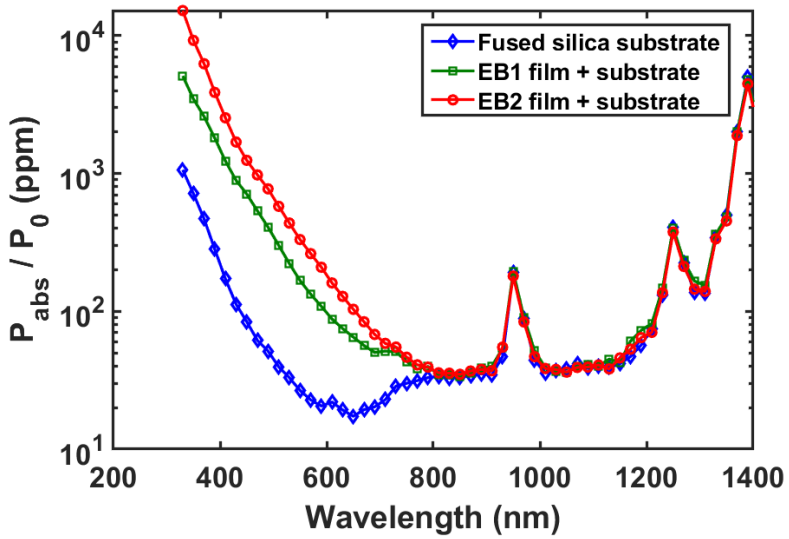

Figure 6.2: Ratio of absorbed power to incident power for a fused silica substrate (Corning 7980), the EB1 film plus substrate, and the EB2 film plus substrate from 330 nm to 1400 nm. The samples have a thickness of 3 mm and a diameter of 1 inch. The wavelength sample point separation is 20 nm. The excitation source had a power of about 30 µW and a 5-nm bandwidth. The measurements are performed at f_m=50 mHz and with a 100-s integration time [123].

The samples have a diameter of 1 inch and a thickness of 3 mm. A calibration factor

of 0.25 nK/pW is obtained. The difference in heat capacity of the three samples is negligible compared to the heat capacity of the measurement unit. Consequently the same calibration factor is obtained for all three samples. Figure 6.2 shows the ratio of absorbed power to incident power (P_{abs}/P_0) for the fused silica substrate, the EB1 film plus substrate, and the EB2 film plus substrate.

When the sample is a single film deposited on top of a substrate, the measured absorbed power P_{abs} is the total power absorbed by film plus substrate. To find the absorption of the film only, one needs to subtract the substrate contribution from P_{abs}.

For such a sample (in an air or vacuum) with known wavelength dependent refractive indices for the film and substrate, the power reflection coefficients at the air-film interface R_{af}, the substrate-air interface, R_s, and the film-substrate interface, R_{fs}, can be calculated, see appendix F. The substrate absorptance A_s can be measured directly using an uncoated reference sample, see section 6.1.1.

Considering the thin film as a resonant cavity, the total transmission $\mathcal{T}_f$ and reflection $\Re_f$ of thin film can be written as [126]:

$$\mathcal{T}_f = \frac{G\left(1-R_{af}\right)\left(1-R_{fs}\right)}{\left(1-G\sqrt{R_{af}R_{fs}}\right)^2 + 4G\sqrt{R_{af}R_{fs}}\,sin^2(kd_f)} \tag{6.2}$$

$$\Re_f = \frac{(\sqrt{R_{af}}-\sqrt{R_{fs}})^2 + 4G\sqrt{R_{af}R_{fs}}\,sin^2(kd_f)}{(1-G\sqrt{R_{af}R_{fs}})^2 + 4G\sqrt{R_{af}R_{fs}}\,sin^2(kd_f)} \tag{6.3}$$

where $G = e^{-A_f}$ and A_f is absorptance of the thin film. $k=2\pi n_f(\lambda)/\lambda$ is the wavenumber and d_f is thickness of the film. $n_f(\lambda)$ is the wavelength-dependent refractive index of the film.

Assuming again an incoherent superposition of excitation light bouncing back and

forth in substrate, the absorbed power P_{abs} by film plus substrate can be written, according to appendix F, as:

$$\frac{P_{abs}}{P_0} = 1 + \mathcal{T}_f \left[\frac{(1+R_s)}{1-R_s R_{fs}} A_s - 1 \right] - \Re_f. \tag{6.4}$$

where P_0 is the illumination power. According to Eq. (6.2) and Eq. (6.3), $\mathcal{T}_f$ and $\Re_f$ are dependent on the film absorptance A_f. Thus Eq. (6.4) can be solved numerically and absorptance A_f of the EB1 and the EB2 films can be obtained.

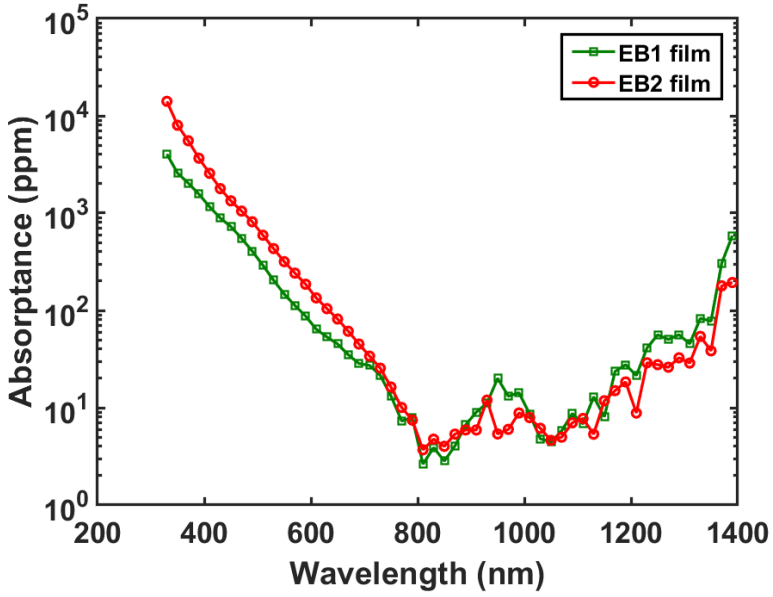

Figure 6.3: Absorption spectra of sample EB1 (with standards oxygen content) and sample EB2 (with reduced oxygen content) from 330 nm to 1400 nm obtained from Eq. (6.4) and the data from Fig. 6.2.

Figure 6.3 shows the absorption spectra of the EB1 film and the EB2 film. Comparing the absorptances of the EB1 and the EB2 films to the P_{abs}/P_0 measured for the EB1 film plus substrate and the EB2 film plus substrate, one can realize that the absorption

contribution from the substrate is not trivial. For instance, the absorptances of both films are about an order of magnitude smaller than the P_{abs}/P_0 measured for EB1 film plus substrate and EB2 film plus substrate in the spectral range from 800 nm to 1400 nm. The peaks at 940 nm and 1250 nm (Fig. 6.2) are due to OH absorption of the substrate. By determining the absorptances of the EB1 and the EB2 films using Eq. (6.4), the substrate contribution is removed. Hence, the OH absorption peaks are not distinctly visible anymore in Fig. 6.3. The measurements revealed enhanced absorption (roughly two times) for the sample with reduced oxygen content (EB2) as compared to the standard sample (EB1) in the spectral range from 330 nm to 750 nm. This enhanced absorption can be attributed to occupied oxygen vacancy defect states located deep in the band gap [127]. Absorption in the near-infrared was found to originate by other than oxygen vacancy structural defects, since no measurable difference between samples EB1 and EB2 can be found in this portion of the spectrum.

6.1.3 Absorption of Two UV Laser Mirrors

There are many applications where a coating stack is deposited on a substrate. For example high-quality coating structures are needed for damage-resistant mirrors in high-power laser applications [128]–[131]. A lot of effort is currently applied to improve deposition technologies and material properties. We received samples from the Laboratory of Thin Film Optics, Shanghai Institute of Optics and Fine Mechanics. The overall goal of the collaborative research was to compare the application of nano-laminate films to traditional dielectric films for UV laser mirrors. Our task was to measure the absorption

spectra of two representative samples - (A) a nanolaminate-based multilayer design (NLD coating) consisting of Al_2O_3-HfO_2 nanolaminate layers and (B) a traditional design of alternating high-n and low-n coatings (TCD coating). The NLD coating structure is as follows: substrate/4L(0.335A0.165H0.335A0.165HL)^{20}A8.15L/air, where A, H and L represent Al_2O_3, HfO_2 and SiO_2, respectively. The numbers represent the optical thickness in units of the quarter-wavelength optical thickness of the respective material. For instance, 0.335A0.165H0.335A0.165H represents a nanolaminate layer with four sublayers. The TCD system has a structure of substrate/4L(HL)^5(AL)^{15}A8.15L/air. The alternating high-*n* and low-*n* layers of HfO_2 and SiO_2 are deposited on the substrate to obtain high reflectivity. Pairs of high-*n* layers of Al_2O_3 (with a relatively larger optical bandgap than HfO_2) and low-*n* layers (SiO_2) are deposited on top to achieve a high laser-induced damage threshold (LIDT). The UV high-reflectors were designed for a wavelength of 355 nm. More details on the design and the preparation of coatings can be found in Ref. [121].

The samples have a diameter of 30 mm and a total thickness of 3 mm. The calibration factor measured for these samples is the same as the one obtained for previous samples. The samples are probed from 330 nm to 1100 nm. The wavelength sample point separation is 5 nm from 330 nm to 400 nm, 20 nm from 410 nm to 790 nm, and 30 nm afterwards. Figure 6.4(a) shows the ratio of absorbed power to incident power (P_{abs}/P_0) for a fused silica reference substrate, the NLD film stack plus substrate, and the TCD film stack plus substrate. Figure 6.4(b) shows the transmittance spectra of the samples measured at room temperature under normal incident angle measured with a UV-visible spectrophotometer (SHIMADZU UV-1601PC).

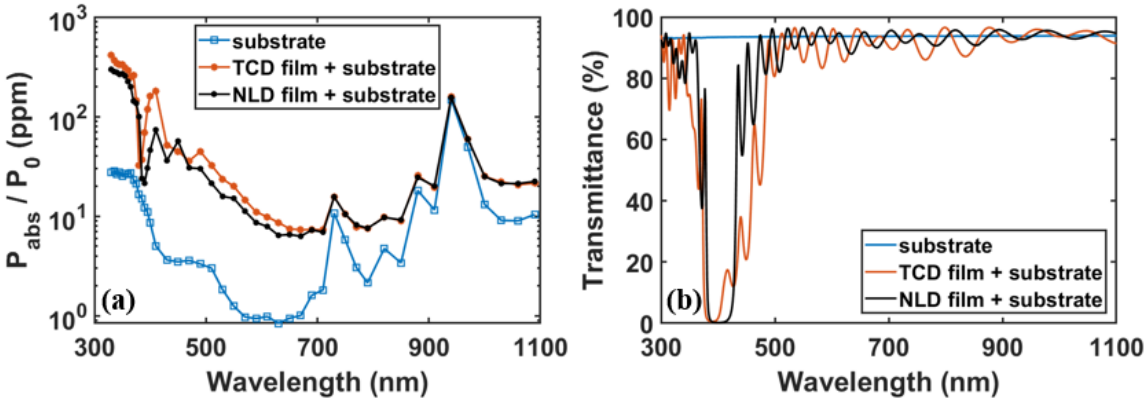

Figure 6.4: Absorption and transmission measurements of two UV mirrors and a reference substrate. (a) Ratio of absorbed power to incident power at ~4 K measured with the optical calorimeter, (b) transmission measured with a spectrophotometer (SHIMADZU UV-1601PC). Data are shown for three different samples – the TCD coating stack plus substrate, the NLD coating stack plus substrate, and a bare reference substrate. The samples have a thickness of 3 mm and a diameter of 30 mm. For the absorption measurement, the excitation source had a power of about 30 μW, a 5-nm bandwidth, and measurements were performed at f_m=50 mHz with 100-s integration time and 200-ms sampling rate. The samples are probed from 330 nm to 1100 nm [121].

To determine the absorption of just the multi-layer film, one needs to subtract the substrate contribution from the total absorption of the sample. This is not as straightforward as finding the absorption of one single-layer film.

Consider a multi-layer film deposited on top of a substrate. The total transmitted power is known and the substrate absorptance A_s is measured independently from a reference substrate sample, see section 6.1.1. The wavelength-dependent refractive index of the substrate is known, so the power reflection coefficient at substrate-air interface, R_s, can be determined, see appendix F. The power reflection coefficient at the film-substrate interface, R_f, can be calculated from the total transmitted power of the coated sample P_T,

$$R_f = \frac{1 - R_s - \left(\frac{P_T}{P_0}\right)}{1 - R_s - R_s\left(\frac{P_T}{P_0}\right)}. \tag{6.5}$$

The derivation of this relation can be found in appendix G. An incoherent superposition of excitation light bouncing back and forth in stack and substrate is assumed again. Hence, the film absorptance in terms of measurable and known quantities can be written as:

$$A_f = \frac{\frac{P_{abs}}{P_0} - A_s\left(1 + \frac{R_s - R_f}{1 - R_s R_f}\right)}{\left(1 + R_s \frac{1 - R_f}{1 - R_s R_f}\right)}. \tag{6.6}$$

The derivation of this relation can be found in appendix G. The absorptance of just the coating stack from the measured P_{abs}/P_0 can be determined from Eq. (6.6).

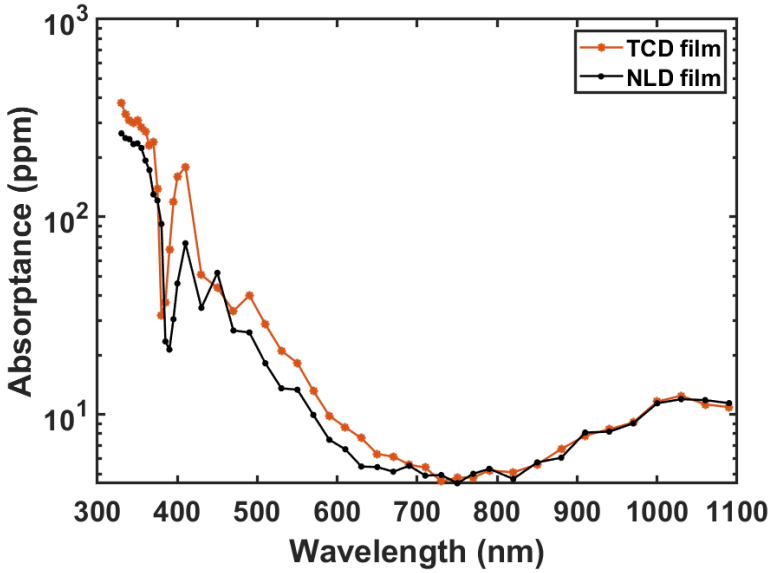

Figure 6.5: Absorption spectra of TCD and NLD coating stacks. The absorption spectra of the films are obtained after subtracting the substrate absorption and considering incoherent superposition of excitation light bouncing back and forth in stack and substrate [121].

Figure 6.5 shows the so obtained absorptances of the TCD and NLD coatings. The

peaks at 730 nm, 880 nm and 940 nm in Fig. 6.4 (a) are due to OH absorption of the substrate and they are not visible in Fig. 6.5 where the substrate absorption is subtracted from the absorption of the mirrors. By comparing Fig 6.4 (a) and Fig. 6.5, we can realize that the substrate is not contributing significantly to the P_{abs}/P_0 of the TCD and NLD mirrors, except for the OH absorption peaks. The absorption losses in the NLD coating stack are about 20% smaller than in the TCD coating stack for comparable overall thickness at the wavelength of interest (355 nm). This absorption loss is mainly attributed to the presence of nodular defects which cause E-field intensification especially in the top layers of the coating stack close to air. Compared to the TCD coating, the NLD coating has a lower E-field intensification, a faster E-field decay with depth, and smaller absorption. The laser-induced damage threshold (LIDT) measured by our collaborators with 7.6 ns pulses at 355 nm was ~1.3 times higher for the NLD coating. Also, the measured bandwidth (over which the reflectance is >99.5%) of the NLD coating was 38 nm, more than twice that of the TCD coating (17 nm) [121]. The nanolaminate layers serve as an effective layer with a high refractive index and a large optical bandgap and can produce superior mirror properties for high-power lasers.

6.1.4 Absorption of Two HR Mirrors for 1064 nm

There is a lot of uncertainty about the role of interfaces for the laser induced damage threshold (LIDT) of multi-layer stacks. Instead of the traditional discrete interfaces between the high-n and low-n coatings, the use of gradual refractive index transitions is discussed and corresponding mirrors are being produced. Many questions remain about the

prospects of this approach [122].

We measured absorption spectra of two, 1064-nm HR mirrors with different (interface) architecture. In the first design, called conventional (CON) design, HfO_2 and SiO_2 were deposited, one material at a time with discrete interfaces. The second mirror was produced with co-evaporated interfaces and is called CEI. Two materials were evaporated simultaneously with different and changing relative deposition rates. This produced a gradual transition from high n to low n layers and vice versa. The coating stacks were designed to have high reflectivity for 1064 nm at normal incidence. Both mirrors have the same overall structure of "substrate|4L$(HL)^{12}$H4L|air", where "H" and "L" denote HfO_2 and SiO_2, respectively. The number before "H" and "L" represent the optical thickness in units of the quarter-wavelength optical thickness of the respective material. More details on design and preparation of coatings can be found in ref. [122]. The absorption measurements were performed to understand the possible role of absorption at interfaces for the LIDT.

The samples have a diameter of 30 mm and a total thickness of 3 mm. Since the coatings are deposited on K9 substrates, absorption of a blank K9 substrate with same dimension is measured as the reference. An approach similar to the one used in section 6.1.3 and appendix G is followed and absorptance of each coating stack is estimated. Figure 6.6 shows the estimated absorptances of the CEI mirror, CON mirror, and K9 substrate.

The higher absorption for CEI coating is attributed to oxygen vacancies created, since the co-evaporation was performed at an oxygen-deficient environment [122]. Interestingly, the LIDT measured by our collaborators with 8 ns pulses at 1064 nm was

higher for the CEI mirror. Yet, the LIDT of the CEI mirror was larger than that of the CON sample. These experimental results suggest that adhesive forces between layers plays a more important role in nanosecond laser damage resistance than interface absorption [122].

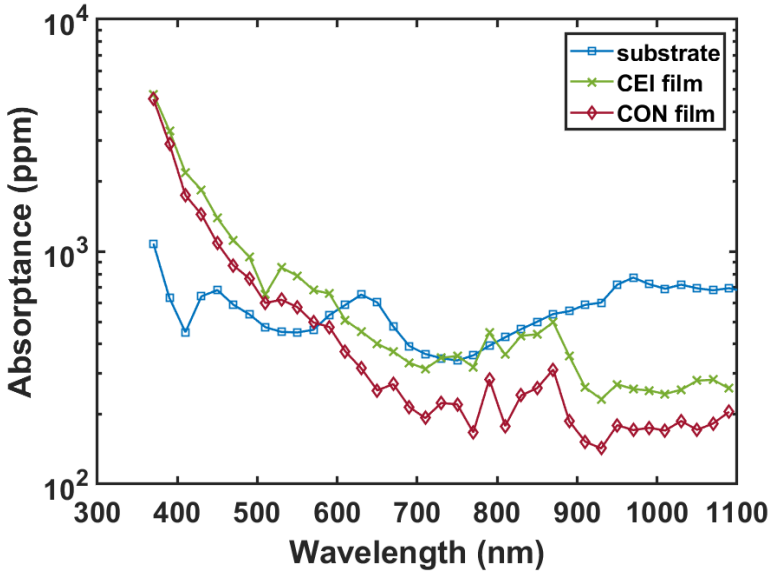

Figure 6.6: Absorption spectra of the CEI mirror, CON mirror and reference substrate from 330 nm to 1100 nm. The wavelength sample point separation is 20 nm. The excitation source had a power of about 30 µW and a 5-nm bandwidth. The optical excitation is modulated (f_m=50 mHz) and the integration time and the sampling rate are 100 s and 200 ms, respectively [122].

6.2 Absorption Measurement with Ultimate Sensitivity

To explore the absorption sensitivity limits of our calorimeter, 15-mW optical power at a wavelength of 639 nm from a diode laser is fiber-coupled into the cryostat. In an absorption measurement with 15 mW of incident power, the transmitted power reaching the beam dump is about 500 times larger than in the experiments where a tunable light

source with an average illumination power of 30 μW is used. The periodic temperature changes in the beam dump due to modulation of the excitation will also be 500 times larger.

To ensure a quiet thermal environment one needs to minimize these temperature excursions in the beam dump (BD) before they can propagate into the thermal system of the measurement unit. To this end, the beam dump was heated out of phase with the optical excitation using an ohmic resistor. The electric power was adjusted such that during the measurement the power dissipated by the BD was approximately constant. Similar to the measurements with low-incident optical power, the temperature stabilization units (including PID-controlled electric heaters and thermometers) on the base plate and the reference ring were active. Since the base plate acts as the thermal reservoir in our thermal network (including measurement unit, reference ring and beam dump), its set temperature defines the temperature at which the measurement is conducted. A power of 15 mW continuously dissipated in the base plate will increase its temperature by ~140 mK. Hence, the temperature of the base plate was set to ~4.2 K.

The test sample was the low-loss fused silica plate that was characterized in section 6.1.1. It has a diameter of 1 in and a thickness of 3 mm. Figure 6.7(a) shows the temperature of the beam dump when it is heated (via an electric resistor) out of phase with the optical excitation. Only a temporary excursion of a few mK occurs when the laser turns on and off. Figure 6.7(b) shows the temperature fluctuations of the reference ring before, after and during the absorption measurement. No evident temperature excursion in the reference ring due to the 15-mW optical input is observable. This demonstrates the effectiveness of the stabilization approach taken.

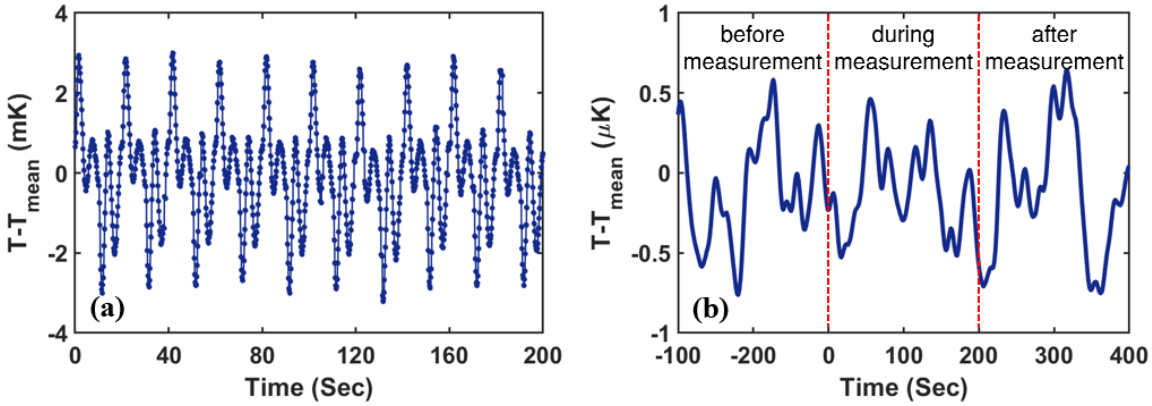

Figure 6.7: (a) Temperature of the beam dump during the absorption measurement with 15 mW incident power. The temperature excursion in the beam dump is minimized by heating it out of phase with the optical excitation modulated at 50 mHz. (b) Temperature fluctuations of the reference ring before, after and during the measurement.

Figure 6.8(a) shows the detrended temperature change of the fused silica substrate illuminated periodically with 15 mW optical power. The measured temperature increase during one excitation cycle, $\Delta T \approx 73$ µK, corresponds to $P_{abs} \approx 292$ nW, which translates to an absorption of $A_s = (P_{abs}/P_0) \approx 20$ ppm. This measured absorption at 639 nm is the same as the one measured by the tunable light source at the low-incident power of 30 µW. Figure 6.8(b) shows the amplitude spectrum of the measured $\Delta T(t)$. The observed signal-to-noise ratio of about 60000 at 50 mHz confirms the previously mentioned sensitivity of the temperature measurement of 2.5 nK. This translates to a minimum detectable absorbed power of 10 pW. At 15 mW incident power the corresponding absorption sensitivity becomes

$$A_{min} \approx \frac{10\ \text{pW}}{15\ \text{mW}} \approx 0.6\ \text{ppb} \tag{6.7}$$

for our 50 mHz modulation frequency with an integration time of 100 s.

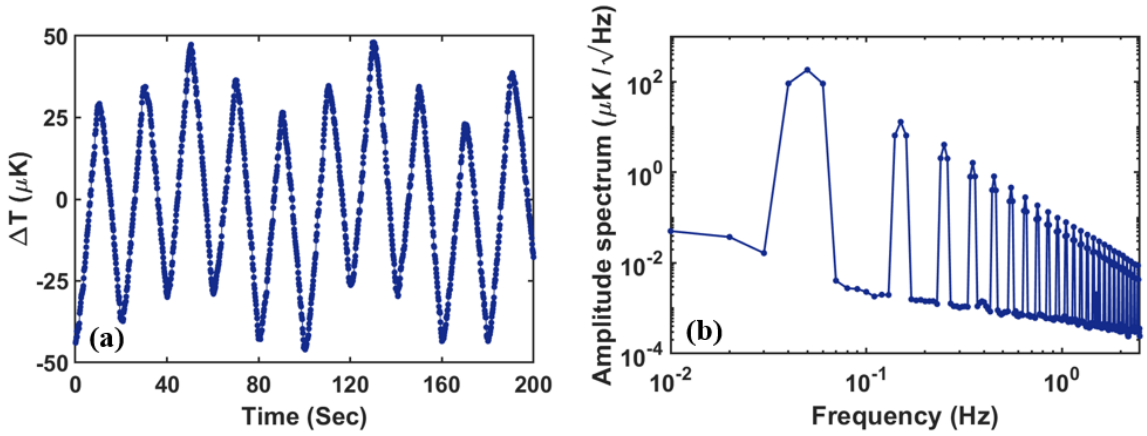

Figure 6.8: (a) Temperature change of the fused silica sample (1 in diameter, 3 mm thick) illuminated periodically (f_m=50 mHz) with 15 mW optical power at a wavelength of 639 nm. (b) Amplitude spectrum of $\Delta T(t)$ showing the 50 mHz modulation component and its higher harmonics. The additional peak at 1.5 Hz is produced by the PTC. The integration time and sampling rate are 100 s and 200 ms, respectively. A signal to noise ratio of ~60000 is obtained at 50 mHz modulation period.

Chapter 7

Summary and Outlook

Sensitive measurements of optical absorption are essential for nondestructive characterization of highly transparent, nonradiative optical materials and the detection of trace impurities in materials where utmost purity and quality are needed. The work presented in this thesis describes the development and demonstration of an optical calorimeter for spectrally resolved absorption measurements from the near IR to the near UV with sensitivity limits on the order of 0.3 ppm at 4 K [124].

A cryogen-free cryostat with a commercial pulse-tube cooler (PTC) was designed and built. The instrument is compact enough to be mounted on an optical table. Starting from room temperature the measurement chamber reaches 4 K after about 14 hours. The

versatile cryostat provides a large number of input and output ports for optical and electronic cables. Optical power is delivered through a multi-mode fiber from either a laser source or a filtered white light source providing 30 μW in a 5-nm wide band tunable from 330 nm to 1700 nm. Optically induced temperature changes were measured with high-resolution thermometers (HRTs) based on paramagnetic salt sensors with SQUID readouts.

PID-controlled temperature stabilization units are deployed in critical places inside the 4-K measurement chamber to produce a quiet thermal environment under load (optical excitation). In particular, periodic temperature changes introduced by the modulated optical pump beam and by the PTC are suppressed. Floating the optical table, flexible thermal connections within the cryostat, and damping of vibrations transmitted from the PTC were measures taken to mitigate noise due to mechanical vibrations. Residual temperature rms values as low as 700 nK integrated from 1 mHz to 2.5 Hz were measured, which compares favorably to the quietest cryostats using PTCs reported to date. Of particular importance is that these noise parameters could be maintained when optical powers as high as 15 mW were dissipated periodically.

Dissipated (absorbed) powers as low as 10 pW could be detected at modulation frequencies of 50 mHz and an integration time of 100 s, which required the detection of temperature changes as small as 2.5 nK. This translates into a measurement sensitivity of 0.3 ppm over the entire tuning range of the filtered white light source. For excitation with a 15-mW laser the absorption sensitivity was 0.6 ppb. At the maximum possible illumination power of 100 mW, limited by the cooling power, the absorption sensitivity would be 0.1 ppb.

The calorimeter was successfully applied to the measurement of three different samples from different research projects [124]. The first test samples were hafnium oxide thin films with varying oxygen content deposited on polished fused silica substrates. The absorption measurement revealed enhanced absorption for the sample with reduced oxygen content as compared to the standard oxygen content sample in the spectral range from 330 nm to 750 nm. The second sample was an Al_2O_3–HfO_2 nanolaminate-based mirror coating (for 355 nm radiation), deposited on a fused silica substrate. This sample showed about 20% less absorption losses compared to the traditional dielectric films in UV laser mirrors for comparable overall thickness at the wavelength of interest (355 nm). The third sample set were 1064-nm high reflective mirrors based on a multi-layer stack of HfO_2 and SiO_2 films deposited with different techniques (one with discrete interfaces and the other one with co-evaporated interfaces). The multi-layer stack with co-evaporated interfaces showed higher absorption, compared to the one with discrete interfaces.

Future work to improve the already excellent performance characteristics of the calorimeter and to add more versatility to the instrument should focus on the following three aspects:

1. Although the achieved P_{min} is low compared to published data, it remains well above the fundamental limits for this system. Based on our test results and on reported observations from other groups, we believe this is due to mechanical vibrations from the 4-K PTC refrigerator. Highly-effective vibration-decoupling schemes for low temperature measurements have recently been demonstrated [132], [133]. We estimate that implementing similar measures will decrease our P_{min} by a factor of 3.

2. The absorption sensitivity of the optical calorimeter can be further improved by decreasing the heat capacity of the measurement unit consisting of sample, measurement ring and the HRT thermometer. We estimate that the use of miniature HRTs [134], [135] and a re-designed sample holder will reduce the heat capacity of the measurement unit and increase the sensitivity by a factor of about 10.

3. The new instrument's breakthrough sensitivity will allow one to implement focused excitation and XYZ scanning for spatial resolution. XYZ scanning stages for operation at 4 K are commercially available. With this approach, absorption spectroscopy of single atoms and molecules should be possible for example.

Appendices

A Fundamental Energy Resolution of a Calorimeter

This derivation is adopted from [49].

Let us first determine the FWHM of a Gaussian distribution:

$$f(x) = \frac{1}{\acute{\sigma}\sqrt{2\pi}} e^{\frac{-(x-x_0)^2}{2\acute{\sigma}^2}} \qquad (A.1)$$

where $\acute{\sigma}$ is the standard deviation of the function. To find FWHM one need to find values of the x where the Gaussian function becomes half of its maximum value, $f(x_{\pm})=1/2\ f(x_0)$, thus:

$$\frac{1}{\acute{\sigma}\sqrt{2\pi}} e^{\frac{-(x_{\pm}-x_0)^2}{2\acute{\sigma}^2}} = \frac{1}{2\acute{\sigma}\sqrt{2\pi}} e^{\frac{-(x_0-x_0)^2}{2\acute{\sigma}^2}} \qquad (A.2)$$

Solving this equation yields:

$$x_{\pm} = \pm\acute{\sigma}\sqrt{2\ ln2} + x_0 \qquad (A.3)$$

The FWHM can be expressed as:

$$FWHM = x_+ - x_- = 2\sqrt{2\ ln2}\ \acute{\sigma} \approx 2.36\ \acute{\sigma} \qquad (A.4)$$

To find the fundamental energy resolution one needs to find the standard deviation of energy, explained in section 1.2.3. Consider a calorimeter, where an absorber with heat capacity C_s and energy E is in thermal contact with a bath at temperature T. The variance of energy of the absorber is defined as:

$$\sigma_E{}^2 = \langle E^2 \rangle - \langle E \rangle^2 \qquad (A.5)$$

Here $\langle E \rangle$ is the expectation value of the energy. If $P(E_i)$ shows the probability that the system is in energy state E_i, then $\langle E \rangle$ can be written as:

$$\langle E \rangle = \frac{\sum_i E_i P(E_i)}{\sum_i P(E_i)} \qquad (A.6)$$

According to the Boltzmann distribution for the energy of a thermodynamic system at temperature T, $P(E_i)$ can be expressed as:

$$P(E_i) = \sum_i e^{-\beta E_i} \qquad (A.7)$$

where $\beta = 1/k_B T$ and k_B is the Boltzmann constant. Using this probability Eq. (A.5) can be written as:

$$\sigma_E{}^2 = \frac{\sum_i E_i{}^2 e^{-\beta E_i}}{\sum_i e^{-\beta E_i}} - \left(\frac{\sum_i E_i e^{-\beta E_i}}{\sum_i e^{-\beta E_i}} \right)^2 \qquad (A.8)$$

The numerator of the first and second terms can be simplified by taking the partial derivative of the exponential term, with respect to β:

$$\sum_i E_i e^{-\beta E_i} = -\frac{\partial}{\partial \beta} \left(\sum_i e^{-\beta E_i} \right) \qquad (A.9)$$

$$\sum_i E_i{}^2 e^{-\beta E_i} = -\frac{\partial}{\partial \beta} \left(\sum_i E_i e^{-\beta E_i} \right) \qquad (A.10)$$

By substituting Eq. (A.9) and Eq. (A.10) in Eq. (A.8), and multiplying both numerator and

denominator of the first term by $\sum_i e^{-\beta E_i}$ we get:

$$\sigma_E{}^2 = \frac{-\frac{\partial}{\partial\beta}\left(\sum_i E_i e^{-\beta E_i}\right)\left(\sum_i e^{-\beta E_i}\right)}{\left(\sum_i e^{-\beta E_i}\right)^2} - \frac{-\left(\frac{\partial}{\partial\beta}\left(\sum_i e^{-\beta E_i}\right)\right)\left(\sum_i E_i e^{-\beta E_i}\right)}{\left(\sum_i e^{-\beta E_i}\right)^2} \qquad (A.11)$$

The above relation can be simplified to:

$$\sigma_E{}^2 = \frac{\partial}{\partial\beta}\left(\frac{\sum_i E_i e^{-\beta E_i}}{\sum_i e^{-\beta E_i}}\right) = \frac{\partial}{\partial\beta}\langle E\rangle \qquad (A.12)$$

Here the definition $\frac{\partial}{\partial\beta}\left(\frac{X}{Y}\right) = \frac{\frac{\partial X}{\partial\beta}Y - \frac{\partial Y}{\partial\beta}X}{Y^2}$ is used to reach from Eq. (A.11) to Eq. (A.12). The expectation value of energy (or mean energy) in statistical mechanics is equal to the negative of the internal energy of the system, *U*, so:

$$\sigma_E{}^2 = \frac{\partial}{\partial\beta}(-U) = -\frac{\partial T}{\partial\beta}\frac{\partial U}{\partial T} \qquad (A.13)$$

From the heat capacity definition, $C_s = \partial U/\partial T$, one can express the standard deviation of the energy as:

$$\sigma_E = \sqrt{k_B T^2 C_s} \qquad (A.14)$$

Using Eq. (A.4), the fundamental energy resolution of a calorimeter can be written as:

$$\Delta E_{FWHM} = 2.36\sqrt{k_B T^2 C_s} \qquad (A.15)$$

B Basic Operation of a Pulse Tube Cooler (PTC)

To simplify the operation of a cryostat, it is very convenient to be able to operate them without a liquid-helium bath. Several technologies have been developed to mechanically cool the cryostat to temperatures below 5 K. These include Stirling

refrigerators, Gifford-McMahon (GM) coolers, and pulse tube coolers (PTCs) to name a few examples [136]. PTCs do not have moving parts that are mechanically or electrically connected to the cryostat. This results in relatively low noise and vibrations compared to other mechanical refrigerators such as GM cryocoolers [112]. PCTs can run for several years without any inspection or regular maintenance.

A pulse tube cooler (PTC) uses helium gas as a working fluid in an expansion-compression cycle. Figure 1 shows a diagram of the simplest version of such a cryocooler.

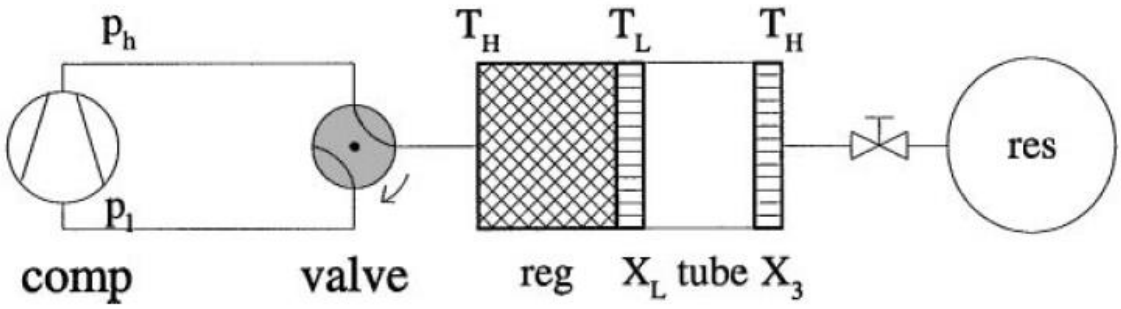

Figure 1: Schematic diagram of a one stage type PTC. A rotary valve alternatively connects the high and low pressure side of the compressor to the tube and a pressure variation is generated inside the tube. The figure is taken from [137].

In this type of cryocooler, the pressure in the pulse tube is periodically varied using a valve system (e.g. rotary valve) alternatively connecting the pulse tube to the high pressure (P_h) and low pressure (P_l) side of a compressor. The compression of the helium gas inside the pulse tube leads to heating while the expansion leads to cooling. A regenerator matrix material, which has a high heat capacity, acts as a heat exchanger. The regenerator precools the room-temperature high pressure gas when it flows to the right and gives off the stored heat to the low pressure cold gas when it flows in the opposite direction.

The basic refrigeration cycle starts when the room temperature helium gas flows through a regenerator, past the cold stage X_L, and into the pulse tube as the pressure increases. The heated compressed gas in the pulse tube then flows towards the heat exchanger X_3 and it is cooled to room temperature T_H before flowing through an orifice and entering the room temperature reservoir. The gas flow stops when the pressure in the pulse tube equals the reservoir pressure. As the rotary valve connects the pulse tube to the low pressure side of the compressor, the helium gas cools in the pulse tube. The reverse flow of the gas from the reservoir forces the low pressure gas towards the cold stage of pulse tube. The cooled gas absorbs heat from the cold stage X_L and provides the useful cooling power. The cooling occurs since the gas depart X_L to the right with a temperature T_L and returns back with a temperature lower than T_L. Eventually the pressure inside the tube increases to reservoir pressure and the refrigeration cycle ends. The entire cycle is then repeated to reach the lowest temperature possible by the PTC. By using two stages in PTC, temperatures down to 2 K can be achieved, where the first stage reaches to temperatures in the range of 40-80 K and the second stage reaches to ~2 K. Detailed descriptions the PTC operation can be found in [136], [138].

C Radiative Heat Flux

This derivation is taken from the COMSOL Multiphysics User's Guide [74].

Assume a point $\bar{p}$ located on a surface with emissivity ε, reflectivity R, absorptivity α, and temperature T. It is assumed that the point object is fully opaque so no radiation is

transmitted through the object, which is true for all the materials used in our simulation. Consider Fig. 2. The left figure shows the irradiation *G* which is the total arriving radiative flux at point $\bar{p}$. The right figure shows the radiosity *J* which is the total outgoing radiative flux from point $\bar{p}$ and can be written as the sum of the reflected irradiation and the emitted radiation:

$$J = RG + \varepsilon\sigma T^4 \qquad (C.1)$$

According to Fig. 2, one can realize that the difference between the irradiation and radiosity would be the net inward radiative heat flux:

$$q_r = G - J \qquad (C.2)$$

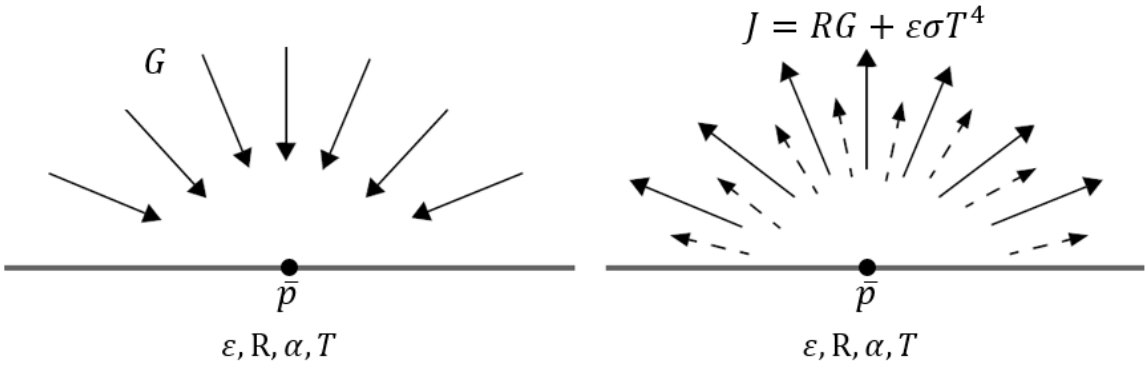

Figure 2: Arriving irradiation (left), leaving radiosity (right). Image taken from [74].

Substituting Eq. (C.1) in Eq. (C.2) yields:

$$q_r = (1 - R)G - \varepsilon\sigma T^4 \qquad (C.3)$$

Assuming $\alpha=\varepsilon=1-R$ (ideal gray body), Eq. (C.3) can be written as:

$$q_r = \varepsilon(G - \sigma T^4) \qquad (C.4)$$

This equation holds for both surface-to-surface and surface-to-ambient radiation. For

surface-to-ambient radiation, *G* can be expressed as:

$$G = \sigma\, T_{amb}^4\,, \qquad (C.5)$$

where T_{amb} is the ambient temperature. To obtain the above relation, it is assumed that the surrounding of the surface has a constant ambient temperature and behaves like a black body $\varepsilon=1$. So for surface-to-ambient radiation, the inward radiative heat flux can be written simply as:

$$q_{r\_amb} = \varepsilon\sigma(T_{amb}^4 - T^4) \qquad (C.6)$$

The total inward radiative heat flux is the sum of two components – surface-to-surface and surface-to-ambient radiative heat fluxes:

$$q_r = \varepsilon\sigma(T_{amb}^4 - T^4) + \varepsilon(G - \sigma T^4) \qquad (C.7)$$

D White Light Source (EQ-99)

The white light source (EQ-99) consists of a controller unit with power supply, lamp house, laser fiber optic cable, and I/O (input/output) connectors. EQ-99 power supply controller is the housing for IR diode laser, laser power supply, and control electronics. I/O connector is the operator interface to the EQ-99.

In the EQ-99 white light source, the plasma is formed at the focusing spot of the laser beam in the center of a fused-silica bulb filled with high-pressure Xenon gas. EQ-99 lamp house is where the xenon plasma is formed. The high-intensity plasma is sustained by absorbing energy from a focused laser beam from the CW diode laser. The laser light is delivered from the power supply controller to the lamp house via a fiber optic cable with

armored protection. Intense plasma with temperatures in the 10,000 – 20,000 K range enable deep ultraviolet production.

E Absorptance of a Substrate

Figure 3 shows a substrate illuminated by a beam light with an incident power P_0. The total absorbed power P_{abs} is measured and known. For a substrate which is thicker than the coherence length of the incident light, we can assume an incoherent superposition of excitation light bouncing back and forth in substrate. We want to determine the substrate absorptance which is the ratio of absorbed power by the substrate to the incident power P_0.

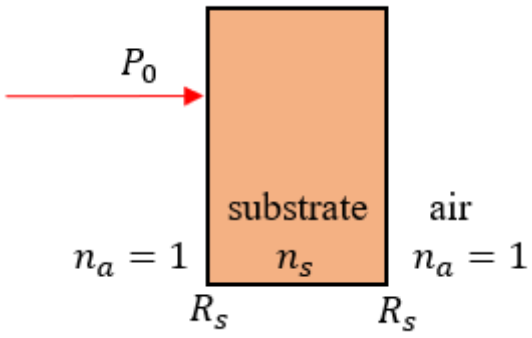

Figure 3: Illumination of a low-loss bulk material with surface reflectance R_s. P_0 is the incident power.

The light power P_{abs} absorbed by the substrate can be written as:

$$P_{abs} = P_0(1 - R_s)A_s\left[1 + R_s + {R_s}^2 + {R_s}^3 + \cdots\right] \qquad (E.1)$$

where A_s is the substrate absorptance, and R_s is the reflectance of the air-substrate interface. The term in brackets is a geometric series. Because $R_s < 1$, the geometric series becomes

$$\sum_{i=0}^{\infty} {R_s}^i = \frac{1}{1 - R_s} \qquad (E.2)$$

Thus the absorptance of the substrate is given by

$$A_s = \frac{P_{abs}}{P_0} \qquad (E.3)$$

independent of the reflectance R_s. For a low-loss substrate with $\alpha d << 1$, where α is the absorption coefficient (in units of m^{-1}) and d is the sample thickness (in units of m), the absorption coefficient can be obtained from:

$$\alpha = \frac{A_s}{d} \qquad (E.4)$$

F Absorptance of a Film with Known Refractive Index

Figure 4 shows a film with known refractive index n_f deposited on a substrate with known refractive index n_s. With the two wavelength dependent refractive indices given, the power reflection coefficient at the film-substrate interface, R_{fs}, can be calculated:

$$R_{fs}(\lambda) = \left| \frac{n_s(\lambda) - n_f(\lambda)}{n_s(\lambda) + n_f(\lambda)} \right|^2 \qquad (F.1)$$

The power reflection coefficients for the air-film interface R_{af}, and substrate-air interface R_s, can be calculated similarly. The sample is illuminated with incident power P_0. Both film and substrate contribute to the total absorbed power P_{abs}:

$$P_{abs} = \Delta P_f + \Delta P_s \qquad (F.2)$$

where ΔP_f and ΔP_s are the absorbed power by film and substrate, respectively. To determine the absorption of the film, we need to subtract contributions of the absorption of

substrate from the total absorbed power.

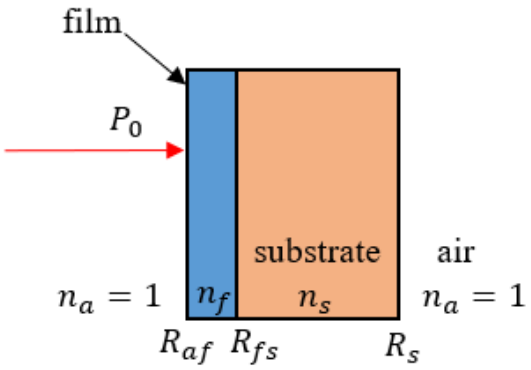

Figure 4: A film with known refractive index n_f deposited on top of a substrate with refractive index n_s. P_0 is the incident power.

Considering the thin film as a resonant cavity, the total transmission $\mathcal{T}_f$ and reflection $\Re_f$ of thin film can be written as [126]:

$$\mathcal{T}_f = \frac{G\left(1 - R_{af}\right)\left(1 - R_{fs}\right)}{\left(1 - G\sqrt{R_{af}R_{fs}}\right)^2 + 4G\sqrt{R_{af}R_{fs}}\,sin^2(kd_f)} \qquad (F.3)$$

$$\Re_f = \frac{(\sqrt{R_{af}} - \sqrt{R_{fs}})^2 + 4G\sqrt{R_{af}R_{fs}}\,sin^2(kd_f)}{(1 - G\sqrt{R_{af}R_{fs}})^2 + 4G\sqrt{R_{af}R_{fs}}\,sin^2(kd_f)} \qquad (F.4)$$

where $G = e^{-A_f}$ and A_f is absorption of the thin film. k=2$\pi n_f(\lambda)/\lambda$ is the wavenumber and d_f is thickness of the film. From above equations one can realize that by expressing ΔP_f and ΔP_s in terms of $\mathcal{T}_f$ and $\Re_f$, the film absorption A_f can be found. We can assume an incoherent superposition of excitation light bouncing back and forth in substrate. Hence, the absorbed power by the substrate can be written as,

$$\Delta P_s = A_s P_0 \mathcal{T}_f\left[1 + R_s + R_s R_{fs} + {R_s}^2 R_{fs} + {R_s}^2 {R_{fs}}^2 + \cdots\right] \qquad (F.5)$$

where A_s is the substrate absorptance and can be measured independently from a reference substrate sample, see appendix E. Equation (F.5) can be rearranged:

$$\Delta P_s = A_s P_0 \mathcal{T}_f (1 + R_s)\left[1 + R_s R_{fs} + {R_s}^2 {R_{fs}}^2 + \cdots\right] \qquad (F.6)$$

The expression in the bracket is a geometric series. Since $R_s R_{fs} < 1$, the geometric series becomes equal to $\frac{1}{1-R_s R_{fs}}$. This simplifies Eq. (F.6):

$$\Delta P_s = A_s P_0 \mathcal{T}_f \frac{(1 + R_s)}{1 - R_s R_{fs}} \qquad (F.7)$$

The power absorbed by the film can be written as:

$$\Delta P_f = P_0 - P_0\left(\mathcal{T}_f + \mathfrak{R}_f\right) \qquad (F.8)$$

By substituting Eq. (F.7) and Eq. (F.8) in Eq. (F.2) we obtain

$$\frac{P_{abs}}{P_0} = 1 + \mathcal{T}_f \left[\frac{(1 + R_s)}{1 - R_s R_{fs}} A_s - 1\right] - \mathfrak{R}_f. \qquad (F.9)$$

According to Eq. (F.3) and Eq. (F.4), $\mathcal{T}_f$ and $\mathfrak{R}_f$ are dependent on the film absorptance A_f. Thus Eq. (F.9) can be solved numerically and A_f can be obtained for the known P_0 and P_{abs}.

G Absorptance of a Multi-layer Film Structure

Consider a multi-layer film deposited on top of a substrate, such as the one depicted in Fig 5. The total transmitted and reflected power are known and the substrate absorption A_s was measured independently from a reference substrate sample, see appendix E. The wavelength-dependent refractive index of the substrate is known, so the power reflection coefficient at substrate-air interface, R_s, can be determined using Eq. (F.1). We are

interested in the absorptance of the layer stack as a whole. Where exactly within the stack absorption occurs cannot be resolved in our measurement. Still, we have to subtract the contribution of the substrate to the overall absorption to be able to characterize the film stack. To this end we devised the following simplified model, based on the schematic diagram shown in Fig.5.

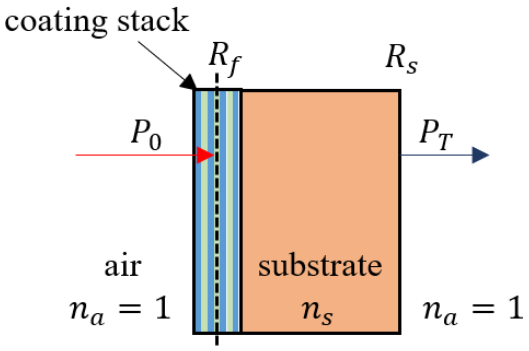

Figure 5: Schematic diagram of a coating stack on top of a substrate. A reflecting interface having a reflectance R_f is assumed in the center of the multi-layer film. P_0 and R_s are the incident power and the reflectance of substrate/air interface, respectively.

We assume again an incoherent superposition of excitation light bouncing back and forth in stack and substrate. To simplify the absorption estimation, we assume one interface in the middle of the multi-layer film with reflectance R_f. For a given incident power P_0, the total absorbed power P_{abs} for the substrate plus multi-layer film, can be written as:

$$\frac{P_{abs}}{P_0} = \frac{A_f}{2} + R_f\frac{A_f}{2} + (1-R_f)[\frac{A_f}{2} + A_s + R_sA_s + R_s\frac{A_f}{2} + R_s(1-R_f)\frac{A_f}{2} + R_sR_f\frac{A_f}{2} + R_sR_fA_s$$

$$+{R_s}^2R_fA_s + {R_s}^2R_f\frac{A_f}{2} + {R_s}^2R_f(1-R_f)\frac{A_f}{2} + {R_s}^2{R_f}^2\frac{A_f}{2} + {R_s}^2{R_f}^2A_s + {R_s}^3{R_f}^2A_s$$

$$+{R_s}^3{R_f}^2\frac{A_f}{2} + {R_s}^3{R_f}^2(1-R_f)\frac{A_f}{2} + \cdots] \qquad (G.1)$$

where A_f, R_f, are the multi-layer film absorptance and film reflectance, respectively. Rearranging and simplifying the above relation will yields:

$$\frac{P_{abs}}{P_0} = A_f\left[1 + R_s(1 - R_f)\{1 + R_sR_f + {R_s}^2{R_f}^2 + \cdots\}\right]$$

$$+A_s\left[1 + (R_s - R_f)\{1 + R_sR_f + {R_s}^2{R_f}^2 + \cdots\}\right] \qquad (G.2)$$

The expressions in the curly brackets are a geometric series. Since $R_s\, R_f < 1$, $\{\ldots\} = \frac{1}{1-R_sR_f}$.

This simplifies Eq. (G.2):

$$\frac{P_{abs}}{P_0} = A_f\left(1 + R_s\frac{1 - R_f}{1 - R_sR_f}\right) + A_s\left(1 + \frac{R_s - R_f}{1 - R_sR_f}\right). \qquad (G.3)$$

The film absorptance in terms of measurable quantities becomes then

$$A_f = \frac{\frac{P_{abs}}{P_0} - A_s\left(1 + \frac{R_s - R_f}{1 - R_sR_f}\right)}{\left(1 + R_s\frac{1 - R_f}{1 - R_sR_f}\right)}. \qquad (G.4)$$

To find R_f one needs to measure the transmission of the coated substrate. Similar to the approach above, the measured transmitted power P_T through the coated sample neglecting the absorption can be written as:

$$\frac{P_T}{P_0} = (1 - R_f)(1 - R_s)\left[1 + R_sR_f + {R_s}^2{R_f}^2 + \cdots + {R_s}^{n-1}{R_f}^{n-1}\right] \qquad (G.5)$$

which yields

$$\frac{P_T}{P_0} = \frac{(1 - R_f)(1 - R_s)}{1 - R_sR_f}, \qquad (G.6)$$

and

$$R_f = \frac{1 - R_s - \left(\frac{P_T}{P_0}\right)}{1 - R_s - R_s\left(\frac{P_T}{P_0}\right)}. \qquad (G.7)$$

By measuring the transmitted power of the coated sample using a spectrophotometer, one can determine $R_f(\lambda)$. The absorptance of the coating stack A_f can now be obtained from Eq. (G.4).

References

[1] J. Campbell, “Damage resistant optical glasses for high power lasers: A continuing glass science and technology challenge,” *Glas. Sci. Technol. Am Main-*, vol. 75, pp. 91–108, 2002.

[2] Y. Mao *et al.*, “The thermal aberration analysis of a lithography projection lens,” in *Optical Microlithography XXX*, 2017, vol. 10147, p. 101471P.

[3] C. Wagner and N. Harned, “EUV lithography: Lithography gets extreme,” *Nat. Photonics*, vol. 4, no. 1, pp. 24–26, 2010.

[4] W. H. Lowdermilk, D. Milam, and F. Rainer, “Optical coatings for laser fusion applications,” *Thin Solid Films*, vol. 73, no. 1, pp. 155–166, 1980.

[5] G. Harry, T. P. Bodiya, and R. Desalvo, *Optical coatings and thermal noise in precision measurement*, vol. 9781107003. 2012.

[6] J. Yu *et al.*, “Laser-Induced Damage Initiation and Growth of Optical Materials,” *Adv. Condens. Matter Phys.*, vol. 2014, 2014.

[7] J. Degallaix *et al.*, “Large and extremely low loss: the unique challenges of

gravitational wave mirrors," *J. Opt. Soc. Am. A*, vol. 36, no. 11, p. C85, 2019.

[8] G. Acchioni, L. Skuja, and D. L. Griscom, Eds., *Defects in SiO2 and Related Dielectrics: Science and Technology*. Springer Science & Business Media, 2012.

[9] A. F. Brooks *et al.*, "Direct measurement of absorption-induced wavefront distortion in high optical power systems," *Appl. Opt.*, vol. 48, no. 2, pp. 355–364, 2009.

[10] S. J. Sheldon, L. V. Knight, and J. M. Thorne, "Laser-induced thermal lens effect: a new theoretical model," *Appl. Opt.*, vol. 21, no. 9, p. 1663, 1982.

[11] B. C. Stuart, M. D. Feit, S. Herman, A. M. Rubenchik, B. W. Shore, and M. D. Perry, "Optical ablation by high-power short-pulse lasers," *J. Opt. Soc. Am. B*, vol. 13, no. 2, p. 459, 1996.

[12] S. Demos, M. Staggs, K. Minoshima, and J. Fujimoto, "Characterization of laser induced damage sites in optical components," *Opt. Express*, vol. 10, no. 25, p. 1444, 2002.

[13] J. D. Musgraves, K. Richardson, and H. Jain, "Laser-induced structural modification, its mechanisms, and applications in glassy optical materials," *Opt. Mater. Express*, vol. 1, no. 5, p. 921, 2011.

[14] K. Arai, H. Imai, H. Hosono, Y. Abe, and H. Imagawa, "Two-photon processes in defect formation by excimer lasers in synthetic silica glass," *Appl. Phys. Lett.*, vol. 53, no. 20, pp. 1891–1893, 1988.

[15] M. Stubenvoll, B. Schäfer, K. Mann, A. Walter, and L. Zittel, "Photothermal absorption measurements for improved thermal stability of high-power laser optics," in *Laser-Induced Damage in Optical Materials: 2013*, 2013, vol. 8885, p. 88851R.

References

[16] M. Baudelet, *Laser spectroscopy for sensing: Fundamentals, techniques and applications*. Woodhead Publishing Series in Electronic and Optical Materials. Elsevier Science, 2014.

[17] J. O. Arroyo and P. Kukura, "Non-fluorescent schemes for single-molecule detection, imaging and spectroscopy," *Nat. Photonics*, vol. 10, no. 1, pp. 11–17, 2016.

[18] W. E. Moerner, Y. Shechtman, and Q. Wang, "Single-molecule spectroscopy and imaging over the decades," *Faraday Discuss.*, vol. 184, pp. 9–36, 2015.

[19] W. E. Moerner and M. Orrit, "Illuminating single molecules in condensed matter," *Science (80-.).*, vol. 283, no. 5408, pp. 1670–1676, 1999.

[20] M. Orrit and J. Bernard, "Single pentacene molecules detected by fluorescence excitation in a p-terphenyl crystal," *Phys. Rev. Lett.*, vol. 65, no. 21, pp. 2716–2719, 1990.

[21] C. Valley, S. Liu, D. Lidke, and K. Lidke, "Sequential Superresolution Imaging of Multiple Targets Using a Single Fluorophore," *PLoS One*, vol. 10, no. 4, p. e0123941, 2015.

[22] R. M. Dickson, A. B. Cubittt, R. Y. Tsient, and W. E. Moerner, "On/off blinking and switching behaviour of single molecules of green fluorescent protein," *Nature*, vol. 388, no. 6640, pp. 355–358, 1997.

[23] W. E. Moerner, "Single-molecule spectroscopy, imaging, and photocontrol: foundations for super-resolution microscopy (nobel lecture)," *Angew. Chemie Int. Ed.*, vol. 54, no. 28, pp. 8067–8093, 2015.

[24] D. Axelrod, D. E. Koppel, J. Schlessinger, E. Elson, and W. W. Webb, "Mobility measurement by analysis of fluorescence photobleaching recovery kinetics," *Biophys. J.*, vol. 16, no. 9, pp. 1055–1069, 1976.

[25] P. Kukura, M. Celebrano, A. Renn, and V. Sandoghdar, "Single-molecule sensitivity in optical absorption at room temperature," *J. Phys. Chem. Lett.*, vol. 1, no. 23, pp. 3323–3327, 2010.

[26] M. Celebrano, P. Kukura, A. Renn, and V. Sandoghdar, "Single-molecule imaging by optical absorption," *Nat. Photonics*, vol. 5, no. 2, pp. 95–98, 2011.

[27] S. E. Bialkowski, *Photothermal spectroscopy methods for chemical analysis*. John Wiley & Sons, 1996.

[28] C. Mühlig, S. Bublitz, and W. Paa, "Enhanced laser-induced deflection measurements for low absorbing highly reflecting mirrors," *Appl. Opt.*, vol. 53, no. 4, p. A16, 2014.

[29] A. Marcano O., C. Loper, and N. Melikechi, "High-sensitivity absorption measurement in water and glass samples using a mode-mismatched pump-probe thermal lens method," *Appl. Phys. Lett.*, vol. 78, no. 22, pp. 3415–3417, 2001.

[30] C. Jacinto and T. Catunda, "High-sensitivity absorption coefficients measurements using thermal lens spectrometry," *J. Phys. IV JP*, vol. 125, pp. 229–232, 2005.

[31] A. Alexandrovski, M. Fejer, A. Markosian, and R. Route, "Photothermal common-path interferometry (PCI): new developments," in *Solid State Lasers XVIII: Technology and Devices*, 2009, vol. 7193, p. 71930D.

[32] A. Gaiduk, M. Yorulmaz, P. V. Ruijgrok, and M. Orrit, "Room-temperature

detection of a single molecule's absorption by photothermal contrast," *Science (80-.).*, vol. 330, no. 6002, pp. 353–356, 2010.

[33] T. X. Ding, L. Hou, H. Van Der Meer, A. P. Alivisatos, and M. Orrit, "Hundreds-fold Sensitivity Enhancement of Photothermal Microscopy in Near-Critical Xenon," *J. Phys. Chem. Lett.*, vol. 7, no. 13, pp. 2524–2529, 2016.

[34] D. B. Leviton and B. J. Frey, "Temperature-dependent absolute refractive index measurements of synthetic fused silica," *Optomech. Technol. Astron.*, vol. 6273, p. 62732K, 2006.

[35] O. Stenzel and M. Ohlidal, *Optical Characterization of Thin Solid Films*, vol. 64, no. 64. Springer, 2018.

[36] M. H. Chien, M. Brameshuber, B. K. Rossboth, G. J. Schütz, and S. Schmid, "Single-molecule optical absorption imaging by nanomechanical photothermal sensing," in *Proceedings of the National Academy of Sciences of the United States of America*, 2018, vol. 115, no. 44, pp. 11150–11155.

[37] K. D. Heylman *et al.*, "Optical microresonators as single-particle absorption spectrometers," *Nat. Photonics*, vol. 10, no. 12, pp. 788–795, 2016.

[38] M. R. Foreman, "Single-particle spectroscopy: Whispers of absorption," *Nat. Photon.*, vol. 10, no. 12, pp. 755–757, 2016.

[39] J. Black, "Lectures on the elements of chemistry," 1803.

[40] S. International Organization for Standardization, Geneva, "ISO 11551: Optics and optical instruments - Lasers and laser-related equipment - Test method for absorptance of optical laser components," vol. 2003. 2003.

[41] B. Li, H. Blaschke, and D. Ristau, "Combined laser calorimetry and photothermal technique for absorption measurement of optical coatings," *Appl. Opt.*, vol. 45, no. 23, pp. 5827–5831, 2006.

[42] L. D. Bowers and P. W. Carr, "Noise measurement and the temperature resolution of negative temperature coefficient thermistors," *Thermochim. Acta*, vol. 10, no. 2, pp. 129–142, 1974.

[43] U. Willamowski, D. Ristau, and E. Welsch, "Measuring the absolute absorptance of optical laser components," *Appl. Opt.*, vol. 37, no. 36, p. 8362, 1998.

[44] R. W. Gammon, J. N. Shaumeyer, M. E. Briggs, H. Boukari, D. A. Gent, and R. A. Wilkinson, "Highlights of the zeno results from the usmp-2 mission," 1995.

[45] L. D. Hansen and R. M. Hart, "The art of calorimetry," *Thermochim. Acta*, vol. 417, no. 2, pp. 257–273, 2004.

[46] A. Eucken, "The determination of specific heat at low temperatures," *Phys. Zeitschrift*, vol. 10, 1909.

[47] W. Nernst, "Specific heat at low temperatures," *Sitzb. Kgl. Preuss. Akad. Wiss*, vol. 12, 1996.

[48] D. Bimberg and A. Bubenzer, "Calorimetric absorption spectroscopy of nonradiative recombination processes in GaP," *Appl. Phys. Lett.*, vol. 38, no. 10, pp. 803–805, 1981.

[49] R. Hummatov, "Gamma-Ray Metallic Magnetic Calorimeters with NbTa Passive Persistent Switches and Electroformed Au Absorbers," 2017.

[50] J. W. Ekin, *Experimental techniques for low-temperature measurements: cryostat*

design, material properties and superconductor critical-current testing. Oxford U. Press, 2006.

[51] P. Geraghty, M. Wixom, and A. H. Francis, "Photocalorimetric spectroscopy and ac calorimetry of thin surface films," *J. Appl. Phys.*, vol. 55, no. 7, pp. 2780–2785, 1984.

[52] H. Gruhl, H. P. Dorn, and K. Winzer, "Calorimetric absorption spectroscopy of J-aggregate dye monolayers below 0.1 Kelvin," *Appl. Phys. B Photophysics Laser Chem.*, vol. 38, no. 3, pp. 199–203, 1985.

[53] A. Juhl, A. Hoffmann, D. Bimberg, and H. J. Schulz, "Bound-exciton-related fine structure in charge transfer spectra of InP:Fe detected by calorimetric absorption spectroscopy," *Appl. Phys. Lett.*, vol. 50, no. 18, pp. 1292–1294, 1987.

[54] A. Juhl and D. Bimberg, "Calorimetric absorption and transmission spectroscopy for determination of quantum efficiencies and characterization of ultrathin layers and nonradiative centers," *J. Appl. Phys.*, vol. 64, no. 1, pp. 303–309, 1988.

[55] I. Akai, T. Karasawa, and Y. Kaifu, "The Photocalorimetric Spectra in Layered BII3 Single Crystals," *J. Phys. Soc. Japan*, vol. 58, no. 2, pp. 718–725, 1989.

[56] L. Podlowski, A. Hoffmann, and I. Broser, "Calorimetric absorption spectroscopy at mK temperatures - an extremely sensitive method to determine nonradiative processes in solids," *J. Cryst. Growth*, vol. 117, no. 1–4, pp. 698–703, 1992.

[57] A. M. Vasson, A. Vasson, J. Leymarie, P. Disseix, P. Boring, and B. Gil, "First investigation on an ultra-thin InAs/InP single quantum well by thermally detected optical absorption spectroscopy," *Semicond. Sci. Technol.*, vol. 8, no. 2, pp. 303–

306, 1993.

[58] Y. Kondo, I. Goto, and N. Sakaida, "Photoinduced anomalous heat generation in AgCl and AgBr single crystals at liquid-helium temperature," *Phys. Rev. B - Condens. Matter Mater. Phys.*, vol. 55, no. 15, pp. 9534–9543, 1997.

[59] J. A. Lipa, B. C. Leslie, and T. C. Wallstrom, "A very high resolution thermometer for use below 7 K," *Phys. B+C*, vol. 107, no. 1–3, pp. 331–332, 1981.

[60] M. J. Adriaans, T. C. P. Chui, M. Ndesandjo, D. R. Swanson, and J. A. Lipa, "High resolution thermometry near the Lambda point," *Phys. B Phys. Condens. Matter*, vol. 169, no. 1–4, pp. 455–456, 1991.

[61] H. Fu *et al.*, "A High-Resolution Thermometer for the Range 1.6 to 5 K," *J. Low Temp. Phys.*, vol. 111, no. 1–2, pp. 49–71, 1998.

[62] R. W. Simon, M. J. Burns, M. S. Colclough, G. Zaharchuk, and R. Cantor, *Mr. SQUID® User's Guide*. v. 6.6, STAR Cryoelectronics, 2012.

[63] D. A. Sergatskov *et al.*, "New Paramagnetic Susceptibility Thermometers for Fundamental Physics Measurements," 2003, pp. 1009–1014.

[64] B. J. Klemme, M. J. Adriaans, P. K. Day, D. A. Sergatskov, T. L. Aselage, and R. V. Duncan, "PdMn and PdFe: New Materials for Temperature Measurement Near 2 K," *J. Low Temp. Phys.*, vol. 116, no. 1–2, pp. 133–146, 1999.

[65] J. Clarke and A. I. Braginski, *The SQUID Handbook*, vol. 1. Weinheim: Wiley-VCH, 2006.

[66] Ray Radebaugh, "Development of the Pulse Tube Refrigerator as an Efficient and Reliable Cryocooler," in *Institute of Refrigeration*, 2000.

[67] C. Wang, G. Thummes, and C. Heiden, "A two-stage pulse tube cooler operating below 4 K," *Cryogenics (Guildf).*, vol. 37, no. 3, pp. 159–164, 1997.

[68] *TransMIT Center for Adaptive Cryotechnology and Sensors*. http://www.cryo.transmit.de.

[69] A. D'Addabbo *et al.*, "An active noise cancellation technique for the CUORE Pulse Tube cryocoolers," *Cryogenics (Guildf).*, vol. 93, pp. 56–65, 2018.

[70] S. Caparrelli *et al.*, "Vibration-free cryostat for low-noise applications of a pulse tube cryocooler," *Rev. Sci. Instrum.*, vol. 77, no. 9, 2006.

[71] E. D. Marquardt, J. P. Le, and R. Radebaugh, "Cryogenic Material Properties Database," in *Cryocoolers 11*, 2006, pp. 681–687.

[72] F. Pobell, *Matter and methods at low temperatures*. Berlin: Springer, 2007.

[73] T. L. Bergman, F. P. Incropera, D. P. DeWitt, and A. S. Lavine, *Fundamentals of Heat and Mass Transfer, Seventh Edition*. New York: John Wiley & Sons, 2011.

[74] *The COMSOL Multiphysics user's guide*. COMSOL Multiphysics® v. 4.2. COMSOL AB, Stockholm, Sweden (2011), pp. 649-651.

[75] R. P. Reed and A. F. Clark, "Materials at Low Temperatures," *Am. Soc. Met.*, p. 590, 1983.

[76] R. L. Powell and F. R. Fichett, "Cryogenic properties of copper," *Int. Copp. Res. Assoc.*, 1979.

[77] *Lake Shore Cryotronics, Inc.* https://www.lakeshore.com/.

[78] S. S. Courts, "A new cryogenic diode thermometer," 2003, pp. 1620–1627.

[79] *Oerlikon Leybold Vacuum*. www.oerlikon.com/leyboldvacuum.

[80] J. G. Weisend II, *Cryostat design: case studies, principles and engineering*. Springer, 2016.

[81] S. Horne *et al.*, "A novel high-brightness broadband light-source technology from the VUV to the IR," in *Next-Generation Spectroscopic Technologies III*, 2010, vol. 7680, p. 76800L.

[82] A. J. Miller, S. W. Nam, J. M. Martinis, and A. V. Sergienko, "Demonstration of a low-noise near-infrared photon counter with multiphoton discrimination," *Appl. Phys. Lett.*, vol. 83, no. 4, pp. 791–793, 2003.

[83] D. Rosenberg, A. E. Lita, A. J. Miller, and S. W. Nam, "Noise-free high-efficiency photon-number-resolving detectors," *Phys. Rev. A - At. Mol. Opt. Phys.*, vol. 71, no. 6, 2005.

[84] A. E. Lita, A. J. Miller, and S. W. Nam, "Counting near-infrared single-photons with 95% efficiency," *Opt. Express*, vol. 16, no. 5, p. 3032, 2008.

[85] D. Fukuda *et al.*, "Titanium-based transition-edge photon number resolving detector with 98% detection efficiency with index-matched small-gap fiber coupling," *Opt. Express*, vol. 19, no. 2, p. 870, 2011.

[86] F. T. Jaeckel, L. N. Le, K. W. Martin, and S. T. P. Boyd, "Development of a precision scanning optical pulser for lowerature particle detectors," in *IEEE Transactions on Applied Superconductivity*, 2013, vol. 23, no. 3.

[87] G. K. White and P. J. Meeson, *Experimental techniques in low temperature physics*. Oxford: Clarendon Press, 1959.

[88] W. M. Rohsenow, J. P. Hartnett, and Y. I. Cho, *Handbook of heat transfer*. New

York: McGraw-Hill, 1998.

[89] M. J. Dipirro and P. J. Shirron, "Heat switches for ADRs," *Cryogenics (Guildf).*, vol. 62, pp. 172–176, 2014.

[90] J. H. Colwell, "The performance of a mechanical heat switch at low temperatures," *Rev. Sci. Instrum.*, vol. 40, no. 9, pp. 1182–1186, 1969.

[91] R. P. Bywaters and R. A. Griffin, "A gas-gap thermal switch for cryogenic applications," *Cryogenics (Guildf).*, vol. 13, no. 6, pp. 344–349, 1973.

[92] V. P. Peshkov and A. Y. Parshin, "Superconducting Thermal Switches," *TPSoviet Phys. J. Exp. Theor. Phys.*, vol. 21, no. 2, pp. 258–265, 1965.

[93] T. C. P. Chui, "SQUID-based high-resolution thermometer," *Cryogenics (Guildf).*, vol. 41, no. 5–6, pp. 407–414, 2001.

[94] P. B. Welander and I. Hahn, "Miniature high-resolution thermometer for low-temperature applications," *Rev. Sci. Instrum.*, vol. 72, no. 9, pp. 3600–3604, 2001.

[95] S. T. P. Boyd, V. Kotsubo, R. Cantor, A. Theodorou, and J. A. Hall, "Miniature thin-film SQUID susceptometer for magnetic microcalorimetry and thermometry," *IEEE Trans. Appl. Supercond.*, vol. 19, no. 3, pp. 697–701, 2009.

[96] S. Narayana and Y. Sato, "Compact miniature high-resolution thermometer," *IEEE Trans. Appl. Supercond.*, vol. 20, no. 6, pp. 2402–2405, 2010.

[97] J. A. Lipa, D. R. Swanson, J. A. Nissen, T. C. P. Chui, and U. E. Israelsson, "Heat capacity and thermal relaxation of bulk helium very near the lambda point," *Phys. Rev. Lett.*, vol. 76, no. 6, pp. 944–947, 1996.

[98] A. Fleischmann *et al.*, "Metallic magnetic calorimeters," in *AIP Conference*

Proceedings, 2009, vol. 1185, pp. 571–578.

[99] P. Welander, M. Barmatz, and I. Hahn, "A new small nano-Kelvin resolution thermometer for low-temperature experiments," *IEEE Trans. Instrum. Meas.*, vol. 49, no. 2, pp. 253–255, 2000.

[100] D. K. Finnemore, T. F. Stromberg, and C. A. Swenson, "Superconducting properties of high-purity niobium," *Phys. Rev.*, vol. 149, no. 1, pp. 231–243, 1966.

[101] STAR Cryoelectronics, "SQUID selection guide." [Online]. Available: https://starcryo.com/lts-sensors/%0D.

[102] H. Ibach and H. Lüth, *Solid-state physics: An introduction to principles of materials science*. 2010.

[103] G. J. Nieuwenhuys, "Magnetic behaviour of cobalt, iron and manganese dissolved in palladium," *Adv. Phys.*, vol. 24, no. 4, pp. 515–591, 1975.

[104] L. N. Le, "Development of Direct Coupled Metallic Magnetic Microcalorimeters for High Energy Resolution Gamma-Ray Spectroscopy," University of New Mexico, 2018.

[105] B. M. Boerstoel, J. J. Zwart, and J. Hansen, "The specific heat of dilute palladium-manganese alloys; Critical behaviour and magnetic-field dependence," *Physica*, vol. 57, no. 3, pp. 397–420, 1972.

[106] J. Bardeen, G. Rickayzen, and L. Tewordt, "Theory of the thermal conductivity of superconductors," *Phys. Rev.*, vol. 113, no. 4, pp. 982–994, 1959.

[107] J. Ekin, "Radiative heat transfer," in *Experimental techniques for low-temperature measurements: cryostat design, material properties and superconductor critical-*

current testing, Oxford university press, 2006, pp. 55–57.

[108] A. L. Woodcraft, G. Ventura, V. Martelli, and W. S. Holland, "Thermal conductance at millikelvin temperatures of woven ribbon cable with phosphor-bronze clad superconducting wires," *Cryogenics (Guildf).*, vol. 50, no. 8, pp. 465–468, 2010.

[109] H. A. Fairbank and D. M. Lee, "Thermal conductivity of 70-30 cupro-nickel alloy from 0.3°to 4.0°K," *Rev. Sci. Instrum.*, vol. 31, no. 6, pp. 660–661, 1960.

[110] G. Armstrong, A. S. Greenberg, and J. R. Sites, "Very low temperature thermal conductivity and optical properties of Stycast 1266 epoxy," *Rev. Sci. Instrum.*, vol. 49, no. 3, pp. 345–347, 1978.

[111] W. H. Press, S. A. Teukolsky, W. T. Vetterling, and B. P. Flannery, *Numerical Recipes in Fortran 77: The Art of Scientific Computing*. Cambridge university press, 1999.

[112] T. Tomaru *et al.*, "Vibration analysis of cryocoolers," *Cryogenics (Guildf).*, vol. 44, no. 5, pp. 309–317, 2004.

[113] T. Tomaru *et al.*, "Vibration-Free Pulse Tube Cryocooler System for Gravitational Wave Detectors, Part I: Vibration-Reduction Method and Measurement," *Cryocoolers 13*, pp. 695–702, 2005.

[114] Y. Ikushima *et al.*, "Ultra-low-vibration pulse-tube cryocooler system - cooling capacity and vibration," *Cryogenics (Guildf).*, vol. 48, no. 9–10, pp. 406–412, 2008.

[115] A. Chijioke and J. Lawall, "Vibration spectrum of a pulse-tube cryostat from 1 Hz to 20 kHz," *Cryogenics (Guildf).*, vol. 50, no. 4, pp. 266–270, 2010.

[116] J. B. Johnson, "Thermal agitation of electricity in conductors," *Phys. Rev.*, vol. 32,

no. 1, pp. 97–109, 1928.

[117] H. Nyquist, "Thermal agitation of electric charge in conductors," *Phys. Rev.*, vol. 32, no. 1918, 1928.

[118] T. C. P. Chui, D. R. Swanson, M. J. Adriaans, J. A. Nissen, and J. A. Lipa, "Temperature fluctuations in the canonical ensemble," *Phys. Rev. Lett.*, vol. 69, no. 21, pp. 3005–3008, 1992.

[119] P. Day, I. Hahn, T. C. Chui, A. W. Harter, D. Rowe, and J. A. Lipa, "The fluctuation-imposed limit for temperature measurement," *J. Low Temp. Phys.*, vol. 107, no. 3–4, pp. 359–370, 1997.

[120] B. Gao *et al.*, "Realization of an ultra-high precision temperature control in a cryogen-free cryostat," *Rev. Sci. Instrum.*, vol. 89, no. 10, 2018.

[121] M. Zhu *et al.*, "Nanolaminate-based design for UV laser mirror coatings," *Light Sci. Appl.*, vol. 9, no. 1, 2020.

[122] N. Xu *et al.*, "Laser resistance dependence of interface for high-reflective coatings studied by capacitance-voltage and absorption measurement," *Opt. Lett.*, vol. 43, no. 18, p. 4538, 2018.

[123] S. Papernov *et al.*, " Optical properties of oxygen vacancies in HfO 2 thin films studied by absorption and luminescence spectroscopy ," *Opt. Express*, vol. 26, no. 13, p. 17608, 2018.

[124] B. Roshanzadeh, S. T. P. Boyd, and W. Rudolph, "Pico-Watt calorimeter for optical absorption spectroscopy," *Appl. Phys. Lett.*, To be Submitted.

[125] R. Kitamura, L. Pilon, and M. Jonasz, "Optical constants of silica glass from extreme

ultraviolet to far infrared at near room temperature," *Appl. Opt.*, vol. 46, no. 33, pp. 8118–8133, 2007.

[126] J. T. Verdeyen, *Laser Electronics*. Englewood Cliffs, NJ: Prentice Hall, 1995.

[127] D. M. Ramo, J. L. Gavartin, A. L. Shluger, and G. Bersuker, "Spectroscopic properties of oxygen vacanciesin monoclinic HfO2 calculated with periodic and embedded cluster density functional theory," *Phys. Rev. B*, vol. 75, no. 20, p. 205336, 2007.

[128] Z. W. Fan, J. S. Qiu, Z. J. Kang, Y. Z. Chen, W. Q. Ge, and X. X. Tang, "High beam quality 5 J, 200 Hz Nd:YAG laser system," *Light Sci. Appl.*, vol. 6, no. 3, 2017.

[129] T. M. Baer and N. P. Bigelow, "2020 Visions (lasers)," *Nature*, vol. 463, pp. 26–32, 2010.

[130] S. Malobabic, M. Jupé, and D. Ristau, "Spatial separation effects in a guiding procedure in a modified ion-beam-sputtering process," *Light Sci. Appl.*, vol. 5, 2016.

[131] C. Jauregui, J. Limpert, and A. Tünnermann, "High-power fibre lasers," *Nat. Photonics*, vol. 7, no. 11, pp. 861–867, 2013.

[132] L. Gottardi *et al.*, "A six-degree-of-freedom micro-vibration acoustic isolator for low-temperature radiation detectors based on superconducting transition-edge sensors," *Rev. Sci. Instrum.*, vol. 90, no. 5, 2019.

[133] M. De Wit *et al.*, "Vibration isolation with high thermal conductance for a cryogen-free dilution refrigerator," *Rev. Sci. Instrum.*, vol. 90, no. 1, 2019.

[134] S. T. P. Boyd *et al.*, "Integrated SQUID/Sensor Metallic Magnetic Microcalorimeter for Gamma-Ray Spectroscopy," *J. Low Temp. Phys.*, vol. 193, no. 3–4, pp. 435–

440, 2018.

[135] A. Reifenberger, A. Reiser, S. Kempf, A. Fleischmann, and C. Enss, "Development of a novel calorimetry setup based on metallic paramagnetic temperature sensors," *Rev. Sci. Instrum.*, vol. 91, no. 3, 2020.

[136] A. T. A. M. De Waele, "Basic operation of cryocoolers and related thermal machines," *J. Low Temp. Phys.*, vol. 164, no. 5–6, pp. 179–236, 2011.

[137] A. T. A. M. De Waele, "Pulse-tube refrigerators: principle, recent developments, and prospects," *Phys. B Condens. Matter*, vol. 280, no. 1–4, pp. 479–482, 2000.

[138] R. Radebaugh, "A review of pulse tube refrigeration," in *Advances in Cryogenic Engineering*, Boston, MA: Springer, 1990, pp. 1191–1205.